A Single Nanoparticle Study of Plasmon Modified Fluorescence

Webster, Linden Ruth

Awarding institution:
King's College London

A Single Nanoparticle Study of Plasmon Modified Fluorescence

Linden Ruth Webster

Department of Physics

King's College London

A thesis submitted for the degree of

Doctor of Philosophy

February 2014

"Great are the works of the Lord, studied by all who delight in them. Full of splendour and majesty is his work, and his righteousness endures forever."

Psalm 111:2-3

Acknowledgements

I would firstly like to say a huge thank you to my supervisor Professor David Richards for all his support and encouragement. Without his patience and excellent advice not only would this project never have been completed, but it would have been much less enjoyable!

I am very grateful to Dr Jia Li for all his help with the experiments, the modification of the set-up and many valuable discussions about the results. Many thanks also to Dr Wayne Dickson, Dr Jean-Sebastien Bouillard, Dr Brad Littleton, Dr James Levitt and Dr Klaus Suhling for their assistance with analysis, the discussions and encouragement they've provided – their expertise and humour has been much appreciated.

Thanks also to Bill Luckhurst for his faultless technical advice and mechanical know-how, without whom no decent samples would have been fabricated, and without whom I'd certainly never have learned how to fix my bike!

Many thanks to the EPSRC for funding this PhD – it's been quite the experience!

Finally, a massive thanks to my wonderful family and friends for their patience, love, encouragement, prayers and support. Special thanks must go to Mummy, Treeni, Niall and Granny who've been there since the beginning, to Danielle and Heather who patiently and graciously lived with the thesis write-up, Eilidh who encouraged and sympathised with the thesis from afar, Furqaan who provided much needed distraction from the thesis, encouragement and interesting discussion while at King's, Sarah, Natalie and Denise who cheered the thesis on from the sidelines, and my ever encouraging and faithful church family at St Helen's who never let me forget why I was doing it all in the first place.

I owe far too many people a debt of thanks to list you all here, but I certainly could never have done it without you, and I hope you know that I am and always will be deeply grateful.

Abstract

It is well established that when in close proximity to gold nanoparticles the optical properties of local fluorescent molecules are dramatically altered. When the localised surface plasmon resonance (LSPR), tuned to the fluorophore absorption band is excited a strong optical enhancement is observed near the nanoparticle due to enhancement in the excitation rate. Both the radiative and non-radiative decay rates undergo significant modification, resulting in either quantum efficiency enhancement, or fluorophore quenching, and a corresponding reduction in the fluorescence lifetime. These effects depend on fluorophore and nanoparticle separation, the fluorophore quantum efficiency, and the alignment of fluorophore excitation and emission wavelength with the LSPR.

Fluorescence lifetime imaging microscopy (FLIM) is used to create high-resolution spatial maps of molecular lifetime and intensity values of single gold nanoparticles deposited on a thin fluorescent-doped polymer film, separated by a SiO_2 spacer layer. A strong enhancement in emission intensity is observed in the region of a single nanoparticle. The fluorescence lifetime images are described well using two contributions to fluorescence decay; an unmodified term, allowing for the fact that the diffraction limited focus is significantly larger than the nanoparticle, and some average modified term, accounting for the reduction in fluorescence lifetime.

Large numbers of nanoparticles are interrogated, giving a statistical distribution of intensity enhancement and lifetime reduction, associated with varying nanoparticle size and shape. These nanoparticle populations are measured for a variety of excitation wavelengths, LSPRs, and dyes, allowing analysis of the relationship between LSPR and fluorophore excitation and emission wavelength. Additionally dark-field information is collected for individual nanoparticles, allowing a direct comparison between LSPR and modified lifetime in order to investigate a correlation between peak lifetime reduction, and optimal overlap of the fluorophore emission and the location of the LSPR.

Table of Contents

List of Figures

Chapter 1 - Introduction

1.1 Motivations of the Project: Plasmonic Modified Fluorescence

Fluorescence spectroscopy and time-resolved fluorescence have long been tools of primary importance in the study of biological samples, but in an increasingly modern and multi-disciplinary scientific culture, its functionality is becoming broader and its use more widespread. There is increasing demand for improvement in imaging and analysis methods; a particularly relevant concern given that traditional fluorescence imaging techniques are often unsuited for very low fluorophore concentration samples, or samples where the structures of interest are sub-resolution. The modification of fluorophore performance by the use of metallic nanostructures has the potential to address both of these issues.

Firstly, the emission of the fluorophore can be enhanced. In 1946 Purcell made the discovery that the rate of spontaneous emission depended not only on the characteristics of the emitter, but the electromagnetic environment in which it resided (3). He observed that a resonator in some resonant cavity subject to a varying magnetic field displayed a sharp resonance absorption peak. Similarly, when considering the response of fluorophores to their local environment it is well established that in the presence of a metallic nanostructure the emission intensity can be significantly enhanced, accompanied by a corresponding reduction in fluorescence lifetime (4,5). This phenomenon is known as metal-enhanced fluorescence (MEF), and is attributed to the fact that localized surface plasmon resonance (LSPR) modes can be excited within a nanostructure turning the structure into a nanoantenna, causing a strong localized electromagnetic field enhancement and thus modifying the radiative and non-radiative decay rates. Additionally, the short-range distance dependence of the LSPR can be used to extract sub-resolution distance data (6-8). The mechanisms by which these phenomena occur will be discussed more fully in chapter 2.

There is no shortage of work in the field considering different nanostructures and fluorescence enhancement, ranging from enhancement in the region of nanorods (9), nanoprisms (10,11) and particle aggregates (12,13), for applications ranging from plasmon-enhanced bio-assays (14) to novel optoelectronic devices (15). However, there is still work to be done to ensure that the picture of the role that spectral overlap between fluorescence

excitation, LSPR and fluorescence emission plays in the enhancement observed in local fluorophores is complete, and this thesis aims to address our understanding of these phenomena.

1.2 Fluorescence

Since this project concerns itself entirely with the manipulation and enhancement of fluorescence techniques, it is prudent to begin with a careful discussion of the mechanism of fluorescence, and to outline the characteristics and properties that this project will seek to exploit.

1.2.1 Fluorescence Mechanisms

The phenomenon of fluorescence is one that has long been observed and manipulated. Sir John Fredrich William Herschel documented an early observation of fluorescence in 1845(16), when he observed that an aqueous solution of quinine and tartaric acid, while perfectly transparent and colourless when placed next to a white background "yet exhibits… under certain incidences of the light, an extremely vivid and beautiful celestial blue colour" (17). Herschel, while lacking the scientific knowledge to explain his discovery, had observed a common and highly aesthetically pleasing example of fluorescence, and Sir George Stokes coined the term fluorescence shortly after (18).

The process by which light is emitted from a material is known as luminescence, and it is under this general category that fluorescence falls, alongside phosphorescence. These two processes are illustrated in a basic Jablonski diagram (19), which can be seen in figure 1.1. In this figure the singlet states are denoted S_0, S_1 etc, and comprise of electron pairs with opposite spin. In each state fluorophores can exist in a number of vibrational energy levels, as illustrated by the sub-states above each bold black line. The presence of these sub-states is the reason that the characteristic emission and absorption spectra do not simply consist of lines of emission and absorption representing the energy difference between S_0 and S_1.

Following the excitation of a molecule through the absorption of light, a fluorophore is excited to a higher order vibrational state through incident light. The fluorophore then typically undergoes rapid internal conversion, which is a process whereby the molecules

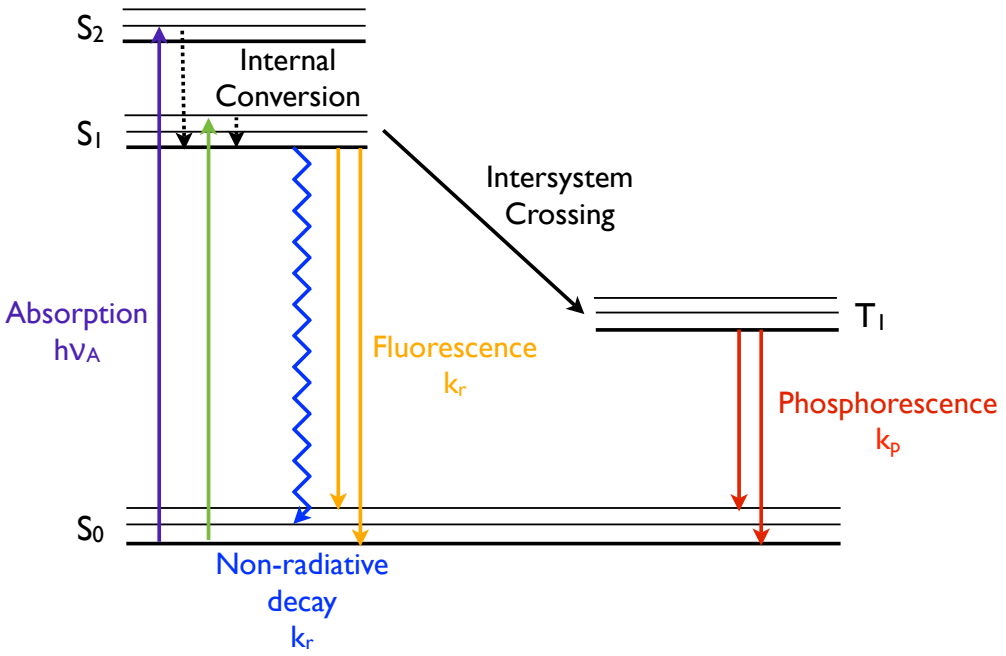

Figure 1.1: A Jablonski diagram showing a typical example of absorption of a photon, and emission either via a non-radiative pathway, fluorescence or phosphorescence. S denotes the singlet state, and T the triplet state.

relax back to the lowest possible excited state (S_1) with a timescale of around 10^{-12} s or less – a significantly faster process than fluorescence emission, with fluorescence lifetimes typically of the order of around 10^{-8} s – and so it can therefore be assumed that internal conversion generally occurs prior to emission. It is the speed of this process that ensures that the vast majority of fluorescence emission occurs from the lowest possible excited vibrational state, S_1.

A transition from excited state S_1 to ground state S_0 can then occur, either via a radiative or a non-radiative pathway. In the case of a radiative pathway, a photon is emitted and it is this process that is called fluorescence. The excited state typically decays into a higher vibrational ground state level, and then quickly reaches thermal equilibrium, again with a timescale of around 10^{-12} s. It is worth pointing out here that the energy of emission for the fluorophore is typically less than that of the energy of excitation – as a result fluorescence emission occurs at longer wavelengths than the wavelengths at which it is excited. This phenomenon was first observed by Sir George Stokes in his paper "On the Refrangibility of Light" in 1852 [3], and is now known as Stoke's Shift. Since, as explained above,

fluorophores transition from highly excited states to the lowest possible excited state S_1, and a photon is only emitted during the transition from S_1 to a higher vibrational ground state, it stands to reason that excitation energy is lost through the thermalisation of these states. There are other reasons that Stoke's shift might be observed, but these are generally environment specific and are not the concern of this thesis.

In addition to the transition from singlet state to singlet state figure 1.1 also depicts a transition from singlet state S_1 to triplet state T_1 – such a transition is known as intersystem crossing. Emission from this triplet state T_1 is known as phosphorescence, and occurs at comparatively longer wavelengths relative to its fluorescence counterpart. Also a direct transition from T_1 to S_0 is forbidden, and as a result phosphorescence lifetimes are typically of the order of milliseconds, or even seconds in extreme cases.

1.2.2 Lifetime and Quantum Yield

Each fluorophore has a characteristic emission and absorption spectrum as can be seen in figure 1.2. However in addition to absorption and emission information, details pertaining to the quantum efficiency, and the lifetime of the fluorophore can be extracted.

When considering a typical singlet fluorescence decay, the total decay rate is defined as

$$\gamma_0 = k_r + k_{nr} \tag{1.1}$$

where k_r is the total radiative decay rate, and k_{nr} is the total non-radiative decay rate. All decay rates give the likelihood of the event they're describing happening within a defined period of time, and therefore are measured in units of probability per unit time (s^{-1}).

The quantum yield of a fluorophore is defined as the number of photons emitted relative to the number of photons absorbed, and so is defined as follows;

$$Q = \frac{k_r}{k_r + k_{nr}} \tag{1.2}$$

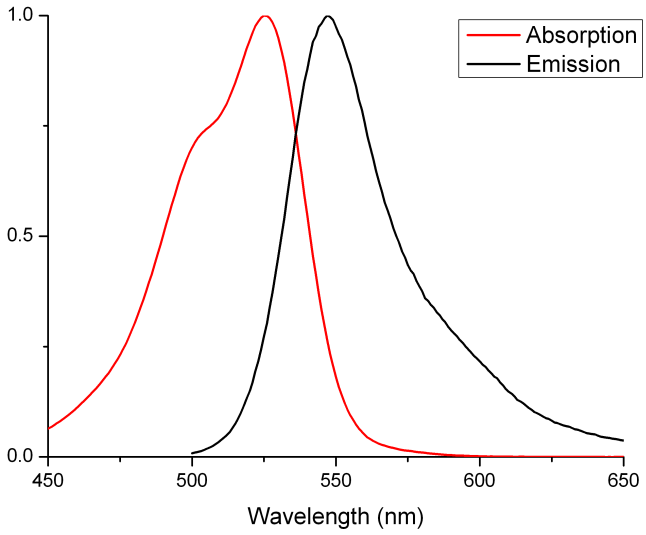

Figure 1.2: A typical normalised fluorescence spectrum showing both absorption and emission for Rhodamine 6G.

Unsurprisingly, the fluorophores with the highest quantum yields have the highest number of photons emitted relative to photons absorbed, and therefore have a much brighter emission relative to excitation – however, due to Stokes losses it is impossible for a fluorophore to have a quantum yield equal to one. It also makes sense that the modification of these radiative and non-radiative decay rates can act to either increase or decrease the quantum yield, a fact that will be discussed in more detail in section 2.3.2.

The lifetime of a fluorophore is then considered to be the average time that a molecule will occupy the excited state before it decays back to the ground state. An average value is necessary because fluorescence emission is a random process and therefore not many molecules will emit at a time of exactly τ. Fluorescence lifetime is therefore calculated by measuring the intensity decay of a large number of fluorophores, and the fluorescence lifetime is taken as the time that it takes for the population intensity to reduce to $1/e$ of its original value. This is the inverse of the total decay rate, which is the sum of the rates at which the excited state can be depopulated, and has the form

$$\tau = \frac{1}{k_r + k_{nr}}. \tag{1.3}$$

Both the radiative (k_r) and non-radiative (k_{nr}) decay rates are strongly dependent on the environment in which the molecule resides. The absorption and emission spectra of the molecule and the refractive index of its environment heavily influence the radiative decay rate, and the non-radiative decay rate depends on factors in the local environment like pH, polarity and the viscosity of the medium in which the molecule resides. This means that the fluorescence intensity is dependent on many variables, and will comprise of contributions from many molecules with many different lifetimes and as such can be generalised in the form

$$I(t) = \sum^{i} A_i \exp\left(-t/\tau_i\right) \tag{1.4}$$

where τ_i is the lifetime of any particular contribution to the emission. As can be surmised from the equation above, fluorescence decay functions can be particularly complex, and fitting of the data is required to extract the parameters A_i and τ_i (14). More discussion of fitting methods used for different fluorescence decays can be found in section 4.5.

1.2.3 Fluorescence Photobleaching

Fluorescence photobleaching is a process distinct from fluorescence decay as described in the previous section. Fluorescence decay is simply the depopulation of an excited fluorescence state back to the ground state after excitation, which for each different fluorophore has some intrinsic timescale, and therefore the decay process does not typically involve any chemical alteration in the fluorophore. Fluorescence photobleaching however is a process whereby the number of molecules in the ground state is depleted by permanent photochemical destruction when molecules are either in the excited singlet or triplet state (20)References. Photobleaching can then be considered to be the loss over time of fluorophore molecules from each excitation/emission cycle, and the rate at which photobleaching occurs is a function of the excitation intensity. Once a molecule has been "bleached" it can no longer be excited/emit and therefore the fluorescence intensity of the population of fluorophores under investigation decreases.

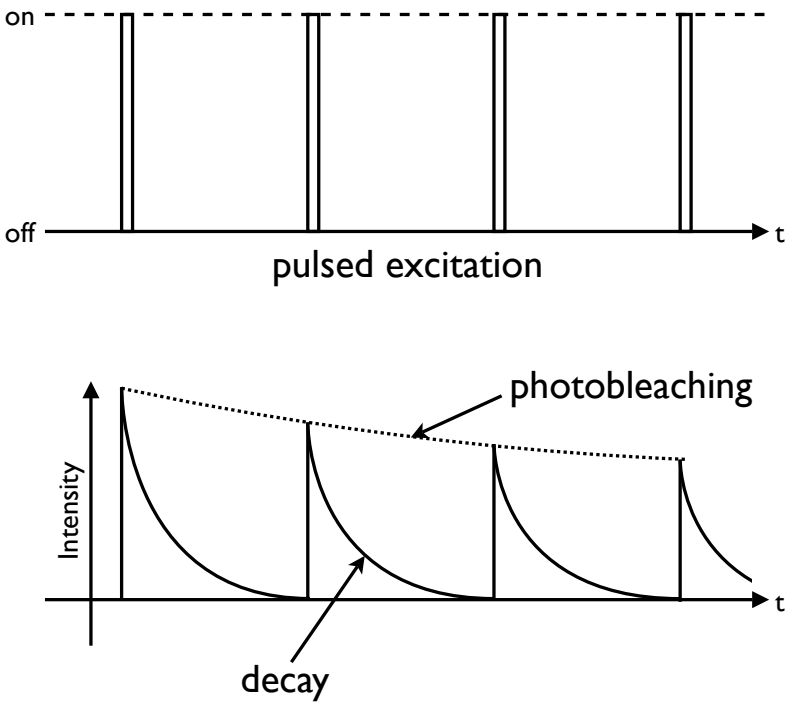

Figure 1.3: A diagram of a pulsed laser excitation and corresponding decrease in intensity with each subsequent excitation pulse.

In figure 1.3 the difference between decay and photobleaching is clearly displayed for a pulsed excitation. The decay process can be seen to be occurring on a much faster timescale than the photobleaching, which is the cumulative effect of fluorescence loss from subsequent emission/excitation cycles. Typically the timescale of photobleaching as a result of pulsed excitation can be observed to be anywhere from milliseconds to minutes, depending on the incident power. Figure 1.4 shows a typical example of fluorophore photobleaching (1). Here a series of images taken at 2-minute intervals show different rates of photobleaching occurring for different fluorophores, but all fluorophores show a marked decrease in intensity by the end of the 10-minute time-frame.

Photobleaching is typically an undesired side-effect of exposure to light. However, techniques like Fluorescence Recovery after Photobleaching (FRAP) are now used to measure the mobility of fluorescent molecules, by quickly bleaching a small spot on the fluorescence surface using a very intense focussed laser beam. The fluorescence signal is then monitored as it recovers, to determine information about the way fluorophores move within the sample (21).

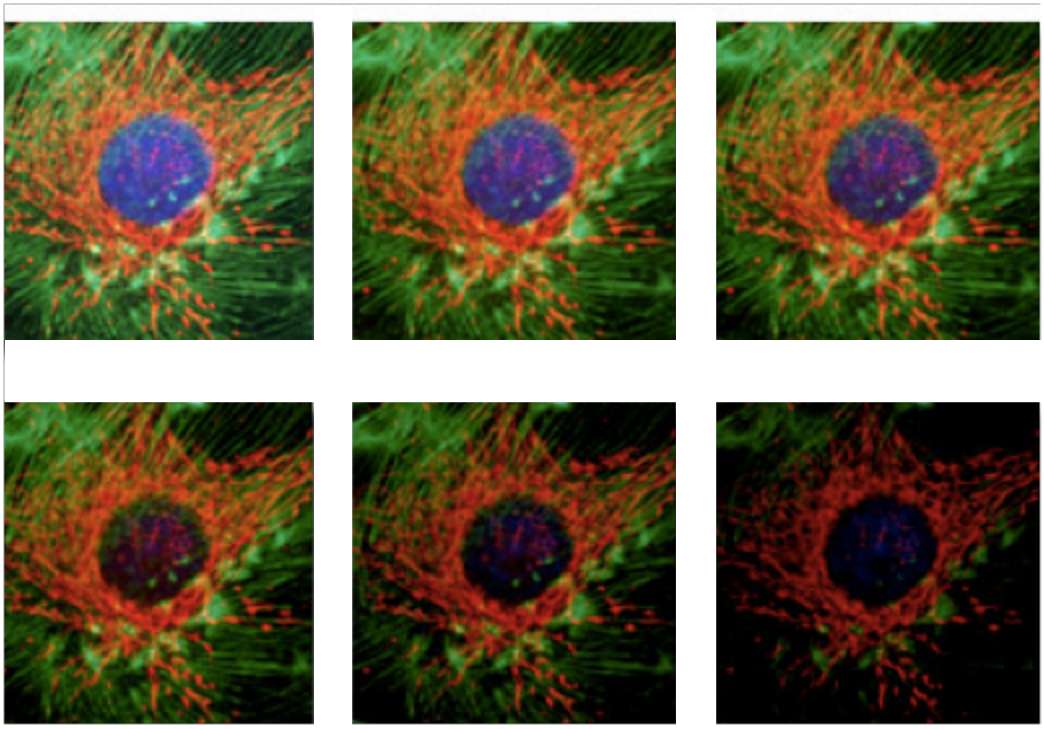

Figure 1.4: A series of images taken from (1) depicting the photobleaching process. The images show a cell with the nucleus stained blue (DAPI), the mitochondria stained red (MitoTracker Red) and the actin cytoskeleton stained green (phallodin derivative). Each image was taken at 2 minute intervals, and a reduction in intensity of all three fluorophores can be seen over the 10 minute period, but each fluorophore photobleaches at comparatively different rates – the DAPI fastest, and the MitoTracker Red slowest.

1.2.4 Fluorescence Resonance Energy Transfer and Self-Quenching

When the emission spectrum of a fluorophore (called the donor molecule) overlaps with the absorption spectrum of some other molecule (called the acceptor molecule) it is possible for a dipole-dipole interaction to be established. This interaction allows the non-radiative transfer of energy from the donor to the acceptor, in that no photons are emitted in the energy transfer process (22). As a result, assuming both species to be fluorescent, there is a decrease in the fluorescence intensity and lifetime of the donor, and an increase in the fluorescence intensity of the acceptor when compared to a complex containing only the donor or acceptor. The lifetime of the donor undergoes a reduction as the presence of the acceptor introduces another pathway for the excited state to decay to the ground state.

The efficiency of this energy transfer, defined as the fraction of donor molecules de-excited via energy transfer to the acceptor is of the form

$$E = \frac{1}{1+\left(\frac{R}{R_0}\right)^6} \tag{1.5}$$

and the rate of energy transfer is similarly given as

$$k_{RET} = \left(\frac{1}{\tau_D}\right) \times \left(\frac{R}{R_0}\right)^6, \tag{1.6}$$

where τ_D is the fluorescence lifetime of the donor molecule, R is the distance between the donor and acceptor molecules, and R_0 is a characteristic distance known as the "Förster radius". R_0 is also the distance at which 50% of the energy is transferred (23). It can be seen that the transfer rate varies inversely to the 6th power with the distance between acceptor and donor. This is because the transfer rate varies with the square of the electric field produced by the donor. The electric dipole induced in the donor by the incident electric field has two components, one that varies as $1/R$ and the other that varies as R^{-3}. Far away from the molecule the $1/R$ term dominates, but at the small distances involved in FRET the dominant component of the field decays as R^{-3}. This high distance sensitivity means that FRET is capable of resolving inter-molecular interactions on the length scale of R_0, which is far below the diffraction limit (24).

While this thesis doesn't concern itself with FRET specifically, the mechanism by which FRET occurs can be responsible for a phenomenon known as fluorescence quenching, which is hugely important in fluorescence imaging. Fluorescence self-quenching is a process that occurs when the quenching of an excited fluorescent molecule is caused by the proximity of that molecule to another of the same species (25). One of the mechanisms by which this occur is known as homo-FRET – identical to FRET, but in this instance rather than having two different species of fluorophore, there is only one. In this case, an excited molecule might, rather than emitting a photon, non-radiatively transfer that energy to a similar neighbouring molecule and cause it to emit instead. Thus it is observed that when fluorescence concentration increases, the emission intensity initially increases proportionally, but then

the relationship ceases to be linear. This phenomenon is usually observed in fluorophores with a small Stokes shift. When in sufficiently close proximity it is possible for a molecule to be excited and emit a photon which is then immediately reabsorbed by a neighbouring molecule prior to its detection.

1.3 The State of the Art in Plasmonic Fluorescence Modification

A large body of work on single nanoparticle fluorescence enhancement informs the research in this thesis, but a brief summary of some of the most influential work is included here.

The resonance properties of single gold nanoparticles are well established, and both Novotny and Sandoghdar's groups have done research into the response of single fluorescent molecules to gold nanoparticles (4,7,8,26). Novotny's group investigated the rate of fluorescence of a single molecule as a function of its distance from a gold nanoparticle, excited by some incident laser. They demonstrated for the first time the continuous transition that occurs from fluorescence quenching to fluorescence enhancement with increasing distance between the fluorophore and the nanoparticle. These results were achieved by attaching the gold nanoparticle to a pointed optical fibre and varying the height of the fibre above the fluorescent molecule by attaching it in turn to a tuning fork crystal. Similarly Sandoghdar's group utilised fibre tips carrying 100nm gold nanoparticles to demonstrate a very high fluorescence intensity modification, more than 20 times, and a 20-fold shortening of the excited state lifetime. They too, clearly showed the role of LSPRs in the excitation and emission modification of fluoroescent molecules.

Looking this time at fixed single nanoparticles, some excellent work has been done by David Ginger's group in the University of Washington concerning the enhancement of fluorescence intensity relative to the degree of spectral overlap between silver nanoprisms, and the fluorescent dye molecules functionalized on their surface (10). This work showed evidence of a strong fluorescence enhancement that depended on the degree of overlap between the LSPR of the nanoprism and the emission of the dye. They also published a paper considering the overlap between the emission of CdSe quantum dots and the LSPR spectra of silver nanoprisms and its effect on intensity and lifetime (11). This paper again showed evidence of strong fluorescence enhancement where overlap between the spectra occurred, as well as a correspondingly located fluorescence lifetime reduction for a collection of different

dyes and a broad range of LSPR values. Similarly, work has been done by Silvia Costa's group concerning the influence of the distance between gold nanoparticles and fluorophores on the extent to which fluorescence is enhanced (27). By depositing polyelectrolyte layers they were able to control the distance between single gold nanoparticles and a fluorophore, and examining a population of nanoparticles, enhancement of absorption and emission were confirmed.

The work in this thesis hopes to add in some small way to this existing body of work, by building on the pioneering work of groups like Novotny and Sandoghdar and approaching similar problems to those addressed by Ginger and Costa's groups, but using different sample configurations and analysis techniques. Ginger's work uses silver nanoprisms which provide a broad range of LSPR profiles, but which are complex nanostructures and, as such, it can be very difficult to model. Especially in the case where these nanoprisms are functionalized, potential irregularities in the shape of the structure might mean that it is very difficult to accurately determine the location of the fluorophores relative to the locally enhanced field. It is hoped that the use of spherical gold nanoparticles, a much simpler structure, in this thesis will prove amenable to future theoretical and computational investigation. Additionally, this thesis is interested in determining the lifetime response to a nanoparticle of fluorescent dyes, rather than quantum dots. Although quantum dots are favourable in terms of their photostability and their comparatively large stokes shift, their photophysics can be complex, and thus their unmodified lifetime decays may not be mono-exponential, and as such the options for fitting the lifetime decays are more limited. Both Ginger and Costa's group opted to use a stretched exponential fit (more will be said on the topic of selecting an appropriate fit in section 4.5), which, while providing an excellent fit to the data, can complicate the analysis of the extent of the plasmonic modification of the fluorescence, and as such most of the data in this thesis will be fitted using a bi-exponential which allowed a simple and intuitive parameterisation of the extent of fluorescence lifetime modification.

1.4 Summary

This chapter has aimed to briefly outline motivations for this project, give some context to the work, and to introduce one of the key topics, the principles of fluorescence. In the following chapters this thesis will outline the background theory to surface enhanced

fluorescence, and will give some background on the experimental techniques relevant to in this field. It will discuss the effects on fluorescence lifetime and intensity enhancement of a single gold nanoparticle, separated from a thin fluorescent-doped polymer film by a SiO_2 spacer layer of varying thickness. Additionally it will address the effects of LSPR spectrum and fluorescence emission spectra overlap on the extent to which intensity enhancement and lifetime reduction is observed in a thin layer of dye-doped polymer located in close proximity to a single spherical gold nanoparticle. This thesis hopes to offer a novel method of analysis for these problems.

Chapter 2 - Principles of Plasmon Enhanced Fluorescence

This chapter concerns itself with giving an overview of the electromagnetic theory involved in the enhancement of fluorescence by simple plasmonic structures. A basic definition of localised surface plasmons is included, as well as simple model calculations for the modification of the electric field in the presence of a sub-wavelength spherical nanostructure. Additionally the mechanisms by which fluorescence excitation and emission are enhanced are outlined.

2.1 Surface Plasmon Polaritons

Surface plasmon polaritons, or surface plasmons (SP) as they are often known, are electromagnetic waves that propagate along the interface of some conductor and some insulator (28,29). They occur when the oscillations of the free electrons in the metal are coupled into incident electromagnetic radiation, effectively trapping it on the surface of the metal. These SPs are responsible for some very interesting optical phenomena, allowing substantial enhancement of the local electric field, and thus the manipulation of light matter interactions relevant in surface enhanced spectroscopy (29).

In figure 2.1 a) the basic schematic of a surface plasmon can be seen, with areas of higher and lower electron density given by + and – respectively. When Maxwell's equations are solved under the appropriate boundary conditions (28) a surface plasmon dispersion relation of the form

$$k_{SP} = k_0 \sqrt{\frac{\varepsilon_d \varepsilon_m}{\varepsilon_d + \varepsilon_m}} \tag{2.1}$$

is derived, where ε_d is the frequency dependent permittivity of the dielectric, and ε_m is the frequency dependent permittivity of the metal (21).

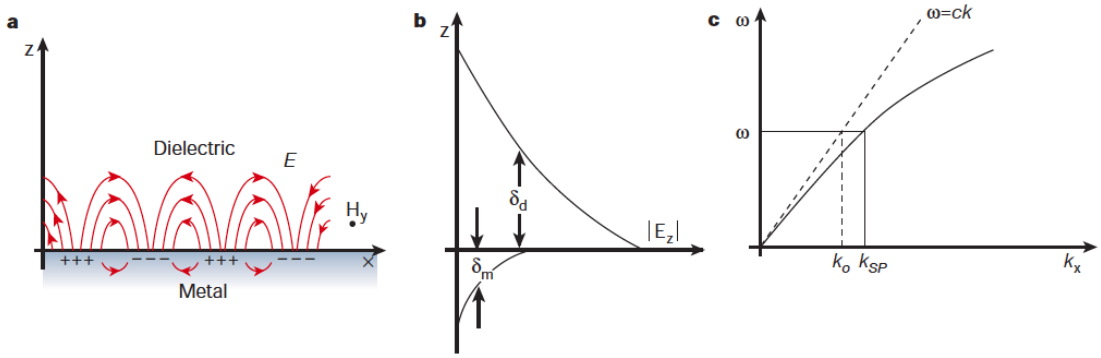

Figure 2.1: a) A surface plasmon propagating along a metal/dielectric interface. b) The variation of the electric field with distance z from the metal/dielectric interface. c) The dispersion curve for the surface plasmon, indicating a disparity between the wave-vector of the incident light, and that of the surface plasmon. Figure taken from (29).

From this equation it is clear that in order for the generation of SPs to be possible it is necessary that ε_d and ε_m have opposite signs. Metals meet this condition as ε_m is both negative and complex, with the imaginary part of ε_m responsible for absorption. However, this results in a momentum mismatch existing between the free space phonon, $\hbar k_0$ (where $k_0 = \omega/c$ is the free-space wavevector) and the momentum of SP mode, $\hbar k_{SP}$, corresponding to the same frequency – the momentum of the free space phonon is less than that of the bound SP, as can be seen in figure 2.1 c). This discrepancy is associated with the energy required to bind the SP to the interface, and must be overcome if light is to be used to generate an SP at the metal/dielectric interface. This can be achieved in a number of ways. The use of a prism, allows for a sufficient increase in the momentum of the incident light or alternatively, surface plasmons can be generated locally either through the presence of a topological surface defect (30,31), or through the use of a periodically roughened surface (14,32). The other result of the interaction between the incident light and the surface charge is that, unlike the manner in which SPs propagate along the surface, the field perpendicular to the surface decays much more quickly, both in the metal and in the dielectric, as can be seen in figure 2.1 b). In the metal the rate of this decay, δ_m, is dictated by the skin depth, whereas in the dielectric medium above the metal the rate of decay, δ_d, is of the order of half the wavelength of the incident electromagnetic radiation. This means that the evanescent field in the metal decays much more rapidly than the field in the dielectric, and the highest electric field enhancements will therefore be found directly at the dielectric interface.

2.2 Localised Surface Plasmons in Nanostructures

In contrast to Surface Plasmons, Localised Surface Plasmons (LSPs) occur when a SP is confined to the dimensions of a sub-wavelength metal particle, and is therefore non-propagating. As shall be demonstrated in the following sections, this confined electrical oscillation leads to a resonance known as the Localised Surface Plasmon Resonance (LSPR) where the light is optimally coupled into the electron cloud. These LSPRs are strongly dependent on the type of nanostructure – its size, its composite material and the environment in which it resides. These properties lead to a highly tunable resonance value across the visible spectrum.

The properties of LSPRs, particularly for gold and silver nanoparticles, have been exploited for thousands of years. Due to the modification of transmitted and reflected light by both scattering and resonance enhanced absorption, different colours are exhibited by the particles, and these were used for decorative purposes long before their physical properties were understood. One of the most notable examples is the Lycurgus Cup, a late Roman cut glass cup where the glass contained gold and silver nanoparticles causing the glass to appear greenish when viewed under reflected light, but to display a characteristic red hue when illuminated from within the goblet with a white light source, due to the absorption of the shorter wavelengths (33).

The LSP operates in the following manner – when a small metal nanoparticle is subject to electromagnetic radiation the electron cloud is displaced relative to the nuclei. Coulomb attraction between the electrons and the nuclei will then lead to the electrons oscillating with respect to the nuclei. The principle of this effect is shown in the schematic of a localised surface plasmon seen in figure 2.2, but here the extent of the displacement is exaggerated to show how the electric field might be induced – in actuality the displacement of the electron cloud is less then 1Å.

In the following sub-sections the dielectric function of a Drude metal is calculated, and that information used to show the electric field in the region of a small metal nanosphere, and thus demonstrate the existence of a resonant mode within the nanosphere.

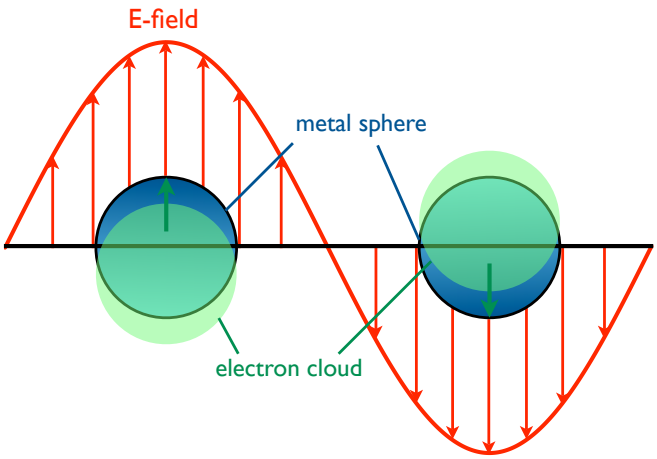

Figure 2.2: A diagram depicting plasmon oscillation for a small metal sphere in an electric field. The electron displacement relative to the nuclei is less then 1Å.

2.2.1 The Dielectric Function of a Drude Metal

At visible wavelengths it is appropriate to use a plasma model to approximate the optical properties of noble metals (including silver and gold). The plasma model consists of a free electron gas which exists in the region of a fixed lattice of ion cores (34). In this model, known as the Drude model, electron-electron interactions are neglected, as is the lattice potential information, both of which make substantial contributions to the permittivity. This approximation means that great care must be taken over which wavelengths this model can be considered sufficient. Instead it is assumed that the optical mass of the electron, m, incorporates some of the information contained within the band structure. The electrons oscillate in response to the applied electric field and the oscillation is damped by collisions occurring with a characteristic collision frequency of $\gamma = 1/\tau$, where τ is the relaxation time of the free electron gas.

An electron within the plasma, subject to an external electromagnetic field $\mathbf{E}$, will have an equation of motion of the form;

$$m\ddot{\mathbf{x}} + m\gamma\dot{\mathbf{x}} = -e\mathbf{E} \tag{2.2}$$

Assuming that the electric field is of the form $\mathbf{E}(t) = \mathbf{E}_0 \exp(-i\omega t)$, then the solution will similarly be of the form $\mathbf{x}(t) = \mathbf{x}_0 \exp(-i\omega t)$. $\mathbf{x}_0$ is a complex amplitude which allows for a

phase shift between the incident and the response fields, and thus the solution takes the form of the equation,

$$\mathbf{x}(t) = \frac{e}{m\left(\omega^2 + i\gamma\omega\right)}\mathbf{E}(t). \tag{2.3}$$

The macroscopic polarization $\mathbf{P} = -ne\mathbf{x}$ is therefore of the form

$$\mathbf{P} = -\frac{ne^2}{m\left(\omega^2 + i\gamma\omega\right)}\mathbf{E}, \tag{2.4}$$

where n is the electron concentration, and considering the fundamental equation for displacement $\mathbf{D}$ derived from Maxwell's equations takes the form $\mathbf{D} = \varepsilon_0\mathbf{E} + \mathbf{P}$, $\mathbf{D}$ in this instance can be expressed as;

$$\mathbf{D} = \varepsilon_0\left(1 - \frac{\omega_p^2}{\omega^2 + i\gamma\omega}\right)\mathbf{E} \tag{2.5}$$

and where the plasmon frequency of the free electron gas is defined as $\omega_p = ne^2 \big/ \varepsilon_0 m$. As such the complex dielectric function of the free electric gas in a Drude metal can be expressed as;

$$\varepsilon(\omega) = 1 - \frac{\omega_p{}^2}{\omega^2 + i\gamma\omega} \tag{2.6}$$

This result will become relevant in the next section where we consider the form that the polarisability of a small sub-wavelength sphere takes in the electrostatic approximation.

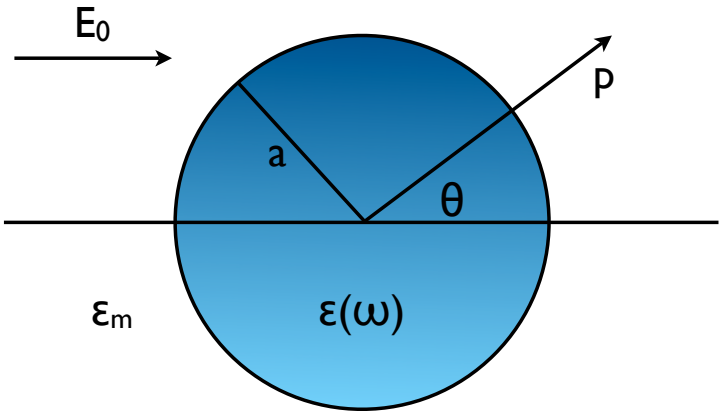

Figure 2.3: A subwavelength isotropic metal sphere in an electrostatic field.

2.2.2 Excitation of a Sub-wavelength Metal Particle

In the instance that particle size, d, is relatively small in comparison to the wavelength of incident light, that is $d << \lambda$ the quasi-static approximation holds true. This means that the phase of the incident electromagnetic radiation can be considered to be uniform over the volume of the sphere, thus allowing the approximation to be made that the particle exists in a static electric field when calculating the modification of the local electric field. This solution is considered to be acceptable for the description of the optical properties of nanoparticles with a size less than 100nm (28).

Consider a system consisting of a homogenous, isotropic sphere of radius a located in a non-absorbing isotropic medium of dielectric constant ε_m. The nanoparticle is then subjected to a uniform static electric field $\mathbf{E} = E_0\hat{\mathbf{z}}$. The configuration can be seen in figure 2.3.

In order to solve the electrostatic approach a solution for the Laplace equation for the potential $\nabla^2\Phi = 0$ is required, from which it is then possible to calculate the electric field $\mathbf{E} = -\nabla\Phi$. Examples of this calculation are widespread (28,34,35). The general solution for the Laplace equation then is of the form;

$$\Phi(\mathrm{r},\theta) = \sum_{l=0}^{\infty}\left[A_l r^l + B_l r^{-(l+1)}\right]P_l(\cos\theta) \tag{2.7}$$

where $P_l(\cos\theta)$ are the Legendre Polynimials of order l, θ is the angle between the position vector $\mathbf{r}$ at point P and the z-axis. Physical constraints demand that potentials remain finite at the origin, and thus the potentials inside, Φ_{in} where $r < a$, and outside, Φ_{out} where $r > a$, the sphere can be written as

$$\Phi_{in}(r,\theta) = \sum_{l=0}^{\infty} A_l r^l P_l(\cos\theta) \tag{2.8}$$

$$\Phi_{out}(r,\theta) = \sum_{l=0}^{\infty} \left[B_l r^l + C_l r^{-(l+1)} \right] P_l(\cos\theta). \tag{2.9}$$

Utilising the boundary conditions at $r \to \infty$ and at the surface of the sphere $r = a$ the values of the coefficients A_l, B_l and C_l can be determined. Since at infinity the field outwith the sphere must tend to the unmodified field, that is $\Phi_{out} \to -E_0 z = -E_0 r\cos\theta$ as $r \to \infty$, $B_1 = -E_0$ and $B_l = 0$ for $l \neq 1$. The boundary conditions at the surface of the sphere then define A_l and C_l. Continuity of the electric field at the boundary requires that the tangential components of the electric field at the interface must be equal, and therefore;

$$-\frac{1}{a}\frac{\partial \Phi_{\text{in}}}{\partial \theta}\bigg|_{r=a} = -\frac{1}{a}\frac{\partial \Phi_{out}}{\partial \theta}\bigg|_{r=a}. \tag{2.10}$$

Similarly, the normal components of the displacement field must also be equal

$$-\varepsilon_0 \varepsilon \frac{\partial \Phi_{\text{in}}}{\partial r}\bigg|_{r=a} = -\varepsilon_0 \varepsilon_r \frac{\partial \Phi_{out}}{\partial r}\bigg|_{r=a}. \tag{2.11}$$

These boundary conditions require that $A_l = C_l = 0$ for $l \neq 1$. As a result the potentials Φ_{in} and Φ_{out} can be seen to be of the form;

$$\Phi_{in} = -\frac{3\varepsilon_m}{\varepsilon + 2\varepsilon_m} E_0 r\cos\theta \tag{2.12a}$$

$$\Phi_{out} = -E_0 r\cos\theta + \frac{\varepsilon - \varepsilon_m}{\varepsilon + 2\varepsilon_m} E_0 a^3 \frac{\cos\theta}{r^2} \tag{2.12b}$$

Our interest is predominantly in the form of Φ_{out}. It can be considered as taking the form of the externally applied field superimposed upon a dipole located at the centre of the nanoparticle. As such Φ_{out} can be re-defined in terms of the dipole moment $\mathbf{p}$ as;

$$\Phi_{out} = -E_0 r\cos\theta + \frac{\mathbf{p}\cdot\mathbf{r}}{4\pi\varepsilon_0\varepsilon_m r^3} \tag{2.13}$$

$$\mathbf{p} = 4\pi\varepsilon_0\varepsilon_m a^3 \frac{\varepsilon-\varepsilon_m}{\varepsilon+2\varepsilon_m}\mathbf{E_0}. \tag{2.14}$$

The introduction of a dipole to describe the polarisation of the sphere is justifiable under the following circumstances. Assuming that the amplitude of the electric field illuminating the sphere is of the form $E_0\exp(i\mathrm{k}z)$ then, again considering a sphere of radius a, if it is assumed that where $\mathrm{k}a << 1$ then it can be shown that both $E_0\exp(-i\mathrm{k}a)$ and $E_0\exp(i\mathrm{k}a)$ are approximately equal to each other, and to unity. In this case the field to which the sphere is exposed is shown to be approximately uniform over the volume encompassed by the sphere (34).

It can be seen then that the magnitude of $\mathbf{p}$ is proportional to the magnitude of the incident electric field, $|\mathbf{E_0}|$. In order to calculate the resonant conditions it is beneficial to define $\mathbf{p}$ in terms of the polarisability, where

$$\mathbf{p} = \varepsilon_0\varepsilon_m\alpha\mathbf{E_0} \tag{2.15}$$

where α, the complex polarisibility of a small, uniform, sub-wavelength sphere in the electrostatic approximation is thus defined as;

$$\alpha = 4\pi a^3 \frac{\varepsilon-\varepsilon_m}{\varepsilon+2\varepsilon_m}. \tag{2.16}$$

From this expression it is clear that a resonant condition for the polarisbility of the sphere must exist when $|\varepsilon+2\varepsilon_m|$ is at a minimum. When considering a metal with dielectric response as expressed in equation 2.6, as defined in section 2.2.1, it can be seen that, in the

case of very small or slowly varying $\mathrm{Im}[\varepsilon]$ the resonance condition for polarisability can be simplified to the form;

$$\mathrm{Re}[\varepsilon(\omega)] = -2\varepsilon_m . \tag{2.17}$$

It is this feature of the polarisability that makes some metals much more suitable for surface enhanced spectroscopy than others.

Naturally, it is unlikely that the nanoparticles utilised in the experiments for this thesis will all be perfectly spherical, but for spheroids and ellipsoids the theory becomes significantly more complicated, requiring rigourous computational modeling. As such it is considered sufficient to demonstrate that a clear resonance characteristic can be seen in metal particles able to demonstrate the condition in equation 2.17 depicted above, since such a computational model is outwith the scope of this project.

2.2.3 Distance Dependence of the External Electric Field

It is worth at this point pausing briefly to consider the distance dependence of this induced reflection field. It can be shown that a field external to the metal sphere can be represented by a dipole field (36) defined as

$$\mathbf{E}_\mathbf{r}(\vec{r},\omega) = \ddot{T}(\vec{r})\,\mathbf{p}(\omega) \tag{2.18}$$

$$\ddot{T}(\vec{r}) = \frac{1}{4\pi\varepsilon_0\varepsilon_m}\frac{3\hat{r}\hat{r} - \ddot{I}}{r^3} \tag{2.19}$$

where $\vec{r} = r\hat{r}$, r is the distance between the point of observation to the centre of the metal sphere, and $\hat{r}$ is a direction vector representing the direction from the observation point to the centre of the sphere, and $\ddot{I}$ is a unit tensor. The assumption that $r << \lambda$ still holds true, and therefore retardation effects can be ignored.

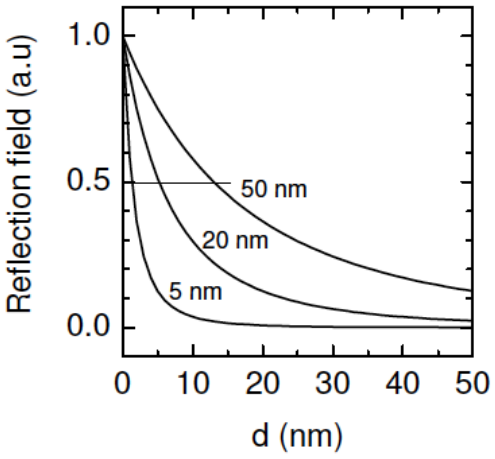

Figure 2.4: A figure taken from (2) showing the distance dependence of three small metal spheres of radius 5, 20 and 50nm, where d is the distance from the surface of the sphere. The fields are normalised to the maximum value of the field at the sphere surface.

If 2.18 and 2.19 are combined with 2.13 and 2.14 then the reflection electric field can be defined as

$$\mathbf{E}_{\mathbf{r}}(\vec{r},\omega) = \frac{3\hat{r}\hat{r} - \vec{I}}{r^3}\frac{\varepsilon_m - \varepsilon}{\varepsilon_m + 2\varepsilon} a^3 \mathbf{E}_{\mathbf{0}}(\omega) \tag{2.20}$$

where $\mathbf{E}_{\mathbf{0}}(\omega)$ is the incident electric field and a is the radius of the metal particle, and thus the total electric field, that is the incident field plus the reflection field, is

$$\mathbf{E}_{\mathbf{r}}(\vec{r},\omega) = \left[\vec{I} + \frac{3\hat{r}\hat{r} - \vec{I}}{r^3}\frac{\varepsilon_m - \varepsilon}{\varepsilon_m + 2\varepsilon} a^3\right]\mathbf{E}_{\mathbf{0}}(\omega). \tag{2.21}$$

It is then possible to determine the distance dependence of the reflection field in 2.20. Figure 2.4 shows this, where all fields are normalised to the maximum value of the field at the sphere surface, and a rapid decay in reflection field with increasing distance is observed. The decay length (that is the distance at which the field amplitude is half that of the maximum value observed at the surface of the sphere) is found to be approximately $0.26\,r$ (2), where r is the radius of the sphere. This means that a shorter decay length for the reflection field is observed for smaller spheres.

2.3 Surface Enhanced Fluorescence

2.3.1 The Modified Electric Field

Calculation of the enhancement undergone by a fluorescent molecule in the presence of an incident electric field in the region of a nanoparticle requires the consideration of three elements of the molecular response; the local electromagnetic field acting on the molecule, the response of the molecule to the field, and the resultant emission of the molecule (37).

In a situation where a molecule, or some arrangement of molecules is situated in the region of a solid surface, represented by a dielectric interface, the resultant field experienced by a molecule located at $\mathbf{r}_0$ when subjected to some incident laser beam can be summed up in the following form;

$$\mathbf{E}_l(\mathbf{r}_0,t) = \mathbf{E}_0(\mathbf{r}_0,t) + \mathbf{E}_r(\mathbf{r}_0,t) + \mathbf{E}_{im}(\mathbf{r}_0,t) + \mathbf{E}_L(\mathbf{r}_0,t). \tag{2.22}$$

This expression shows the different components that contribute to the spectroscopic effects observed, and these will briefly now be outlined.

$\mathbf{E}_0(\mathbf{r}_0,t)$ is the form of the **incident field** in the absence of both the solid and the molecules. In the presence of the solid a second field is introduced, $\mathbf{E}_r(\mathbf{r}_0,t)$, which is known as the **reflected field**, as mentioned above, and occurs as a result of the polarisation of the solid by the incident electric field. Together, these fields are known as the **primary field**, which takes the form

$$\mathbf{E}_p(\mathbf{r}_0,t) = \mathbf{E}_0(\mathbf{r}_0,t) + \mathbf{E}_r(\mathbf{r}_0,t) \tag{2.23}$$

and describes the total electric field in the absence of any local molecules. The magnitude of the primary field is responsible for the magnitude of the induced dipole and therefore the rate of excitation experienced by a molecule in a given position $\mathbf{r}_0$ (38).

When molecules are then added to the system there are two other fields present. The first of these is **image field**, $\mathbf{E}_{im}(\mathbf{r}_0,t)$. When a molecule is subjected to the primary field, its polarisation induces a corresponding polarisation in the solid. This polarisation in turn

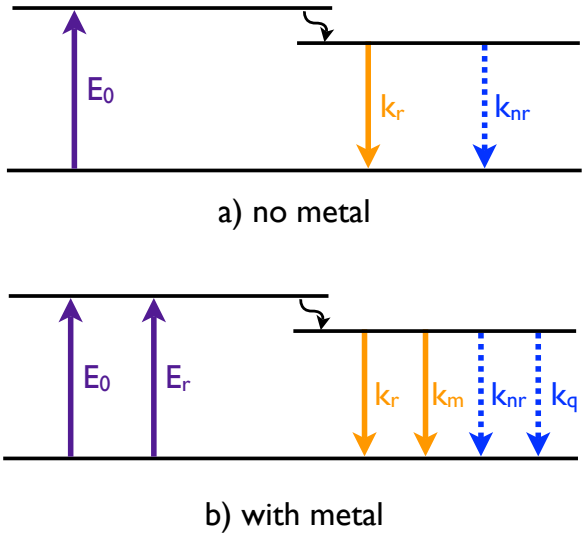

Figure 2.5: The effects of the addition of metal in close proximity of a fluorescent molecule – a) shows the excitation and decay components of fluorescence in the absence of a metal, b) shows additional components in the presence of a metal.

modifies the electric field located at $\mathbf{r}_0$, introducing the extra component known as the image field. The final component is known as the **Lorentz field**, $\mathbf{E}_L(\mathbf{r}_0,t)$, and is simply the electromagnetic field induced by the presence of other localised polarised molecules. Similarly, the sum of these fields is known as the secondary field, and takes the form;

$$\mathbf{E}_s(\mathbf{r}_0,t) = \mathbf{E}_{im}(\mathbf{r}_0,t) + \mathbf{E}_L(\mathbf{r}_0,t). \tag{2.24}$$

The influence of this secondary field affects the molecule by modifying its polarisability, the end result of which is a modification of the fluorescence lifetime (37).

2.3.2 Additional Excitation and Emission Components

The decay rate, γ_0, quantum yield, Q, and lifetime, τ, of an unmodified fluorophore are described by equations 1.1, 1.2 and 1.3 respectively. If the fluorophore is approximated as a point dipole then the intensity of an unmodified fluorophore in free space can then be expressed as

$$S = C\left|E_0(\omega_{abs})\right|^2 \sigma_{abs}(\omega_{abs}) Q(\omega_{fluoro}), \tag{2.25}$$

where C is a calibration constant representing the efficiency of photon detection, $\left|E_0(\omega_{abs})\right|^2$ is the intensity of the incident electromagnetic field at the molecular absorption frequency, $Q(\omega_{fluoro})$ is the quantum efficiency at the fluorescence wavelength, and $\sigma_{abs}(\omega_{abs})$ is the absorption cross section, a measurement of the probability of absorption of an incident photon by the molecule in question (37,39).

In the presence of a dielectric or metal structure, additional excitation, radiative emission and non-radiative emission terms are introduced, as can be seen in figure 2.5. These new terms include a modified excitation term, E_r, a modified radiative rate term, k_m, and a modified non-radiative term which represents the quenching of the molecule, k_q. As such the expressions for modified radiative decay rate, k_r', the modified total decay rate, γ', the modified quantum yield, Q', and modified lifetime, τ' are given as follows;

$$k_r' = k_r + k_m \tag{2.26}$$

$$\gamma' = k_r + k_{nr} + k_m + k_q = \gamma_0 + k_m + k_q \tag{2.27}$$

$$\tau' = \frac{1}{\gamma_0 + k_m + k_q} \tag{2.28}$$

$$Q' = \frac{k_r'}{\gamma'} \tag{2.29}$$

and assuming that the absorption cross section remains unchanged, the intensity expression takes this form,

$$S' = C'\left|E_p(\omega_{abs})\right|^2 \sigma_{abs}(\omega_{abs}) Q'(\omega_{fluoro}), \tag{2.30}$$

where the primes indicate a modified function, and $\left|E_p(\omega_{abs})\right|^2$ is the intensity of the primary field at the molecule and at the molecular absorption frequency.

It is therefore possible to define an expression for a modification factor for the fluorescence intensity by taking the ratio of S' to S of the form

$$\chi = \frac{S'}{S} = \frac{C'}{C}\frac{Q'(\omega_{fluoro})}{Q(\omega_{fluoro})}\left|\frac{E_p(\omega_{abs})}{E_0(\omega_{abs})}\right|^2 \tag{2.31}$$

It is clear to see that the extent to which a modification occurs is dependent on the extent to which the excitation rate, the quantum yield, the emission rate and the collection efficiency are modified.

The specifics of how these additional factors will act to modify both excitation and emission will be discussed in more detail in the following sections.

2.3.3 Modification of Fluorescence Excitation

An enhancement in fluorescence excitation implies an increased rate of molecular transitions from the ground state to an excited state. This is due to a modification in the primary field as defined in equation 2.23, where an increase in the incident electric field effectively means that more photons will interact with the molecule than previously, and it is this interaction that is responsible for the additional excitation term E_r. As such, despite an increase in fluorescence intensity proportional to the enhancement of the electric field, it is not expected that the lifetime should be modified – the system is simply pumped harder. Additionally, given that the enhancement of the electric field is greatest at the nanoparticle surface, it would make sense to assume that the closer the fluorophore is to the nanoparticle the greater the excitation enhancement that will be observed, but this must be carefully balanced against the quenching effects that occur when a fluorophore is brought into close proximity to a metal surface (40).

2.3.4 A Classical Model for Modification of Fluorescence Emission

The modification of fluorescence emission in particular has been broadly studied. Much work has been done considering a classical model, particularly in the seminal work of Chance, Prock and Silbey in the 1970s (41,42) and also by Gersten and Nitzan (43). The

development of the classical model described well a series of experiments that had first been carried out not long before by Drexhage and his coworkers (44). They described the response of a fluorophore undergoing some interaction with a planar dielectric surface. In these calculations a fluorophore can be approximated as a point dipole, p. While this is not the case – in reality the charge distribution induced by the electric field extends over all dimensions of the molecule – it is adequate as the size of the molecule is small in comparison to the size of the variation in the applied electric field, and holds providing the distance between the molecule and the nanoparticle is large compared to the molecular size. With this approximation a simple classical approach to the theoretical model can be outlined, following the reasoning given in (45,46).

What is needed in order to determine the behaviour of p, some expression that calculates the interaction of the dipole field reflected from the dielectric surface and the original dipole field at the location of the dipole is required. This is calculated using the following steps. Initially the dipole field is defined in terms of a summation of plane waves, and then the amplitude and phase each of these plane wave components is calculated when they are reflected off the planar surface. These are then combined to form some net reflected field. This field then interacts with the dipole field, thus modifying the spontaneous emission rate. For the sake of transparency, a few approximations must also be made in such a model. In addition to assuming the fluorophore to be a point dipole the dielectric surface is assumed to be perfectly flat, and the interface between the dielectric and the surrounding medium to be infinitely sharp. The medium in which the dipole is embedded is lossless, and at the emission wavelength neither it nor the dielectric exhibit gain. With these conditions and limitations clear, the fluorophore can be considered to be an oscillating dipole $\vec{p}$, such that the equation of motion for the dipole moment is

$$\frac{d^2\vec{p}}{dt^2} + k_0 \frac{d\vec{p}}{dt} + \omega_0 \vec{p} = \frac{e^2}{m} \vec{E}_{im}(\vec{r}_0), \tag{2.32}$$

where k_0 is the oscillator damping rate in free space, ω_0 is the resonant frequency in the absence of damping, e is the electric charge, m is the effective mass of the particle and $\vec{E}_{im}(\vec{r}_0)$ is the electric field at the position of the dipole as a result of the reflection of the emitted electric field by the dielectric surface. This is the same as the image field described in section 2.3.1. The solution to this equation is therefore of the form

$$\vec{p} = \vec{p}_0 \exp(-kt)\exp(i\omega t). \tag{2.33}$$

When this is substituted into equation 2.32, and the real and imaginary components are equated, the modified damping rate, k, and the frequency shift, $\Delta\omega$, can be found. The modified damping rate is seen to be of the form

$$k = k_0 + \frac{e^2}{m\omega_0 |p|^2} \mathrm{Im}\left(\vec{p}^{\,*} . \vec{E}_{im}(\vec{r}_0)\right) \tag{2.34}$$

and frequency shift is of the form

$$\Delta\omega = \omega - \omega_0 = -\frac{{k_0}^2}{8\omega_0} - \frac{e^2}{m\omega_0 |p|^2} \mathrm{Re}\left(\vec{p}^{\,*} . \vec{E}_{im}(\vec{r}_0)\right), \tag{2.35}$$

where * denotes the complex conjugate (37). In this equation k is the equivalent of the inverse of the fluorescence lifetime, that is $1/\tau$. Equation 2.35 thus makes it clear that in order to accurately determine the modified decay rate, it is essential that $\vec{E}_{im}(\vec{r}_0)$, the reflected field at the dipole position be calculated.

It is now worth considering more carefully what these equations might mean. Firstly, it is important to consider the effect on $\vec{E}_{im}(\vec{r}_0)$ that the orientation of the fluorescent dipole to the dielectric surface will have. This problem can be seen most clearly seen when considering the image charge induced in a perfect mirror in figure 2.6 a). In the case of a dipole with orientation perpendicular to the surface, the image charge serves to reinforce the electric field of the dipole, causing an enhancement, whereas a dipole with orientation parallel to the surface produces an image charge that cancels out the dipole. The effect that these different orientations have on the decay rate is shown in figure 2.6 b), and the decay rates for dipoles oriented perpendicular seem to show local maxima at the same location that dipoles oriented parallel to the surface seem to show local minima, and these will in turn modify k and $\Delta\omega$ in equations 2.28 and 2.29.

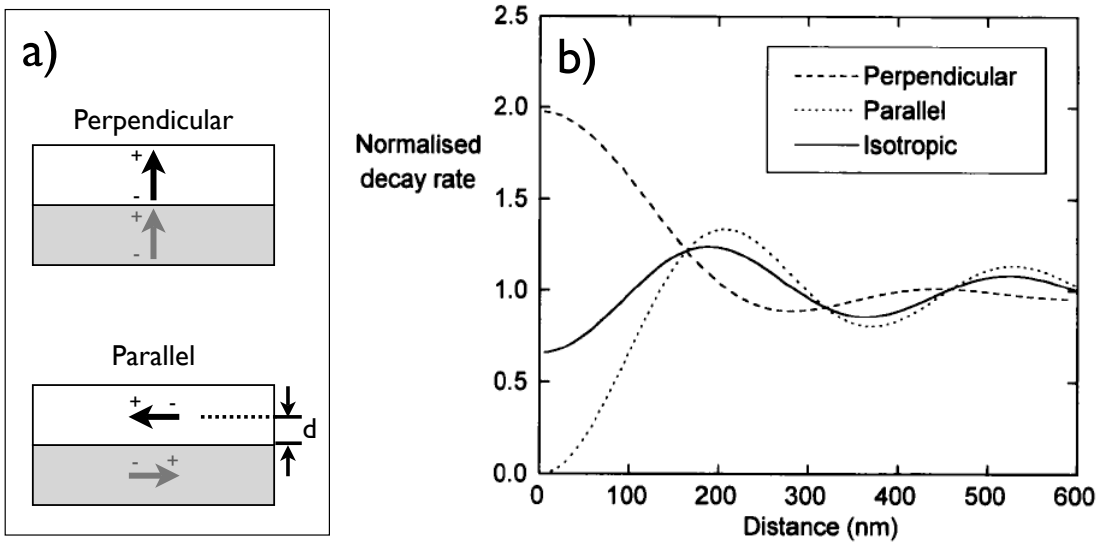

Figure 2.6: a) The effects of dipole orientation near a plane-mirrored surface. The paler grey dipole represents the image dipole induced by the presence of the dipole. b) The calculated decay rates for different dipole orientations in front of a perfect mirror, and with varying distance. Taken from (45).

Additionally, the reflected electromagnetic radiation can either be in phase or out of phase with the dipole oscillation of the fluorophore, thus determining whether or not the photonic mode density (PMD) is high or low, and whether emission will be enhanced or inhibited. Also as distance increases between the dipole and the dielectric the oscillation strength will decrease as the dipole is considered to be a point source, and so the normalised decay rate will tend to 1 at infinite distance from the dipole. These characteristics are clearly demonstrated in figure 2.7.

Figure 2.7 also demonstrates a very important feature when considering fluorescence near a metal. For very small dipole-dielectric distances a strong lifetime quenching is observed, as the electric field of the dipole couples into SPP modes, allowing a non-radiative decay pathway from the excited state of the fluorophore. This causes the lifetime, and therefore the quantum yield, to decay rapidly to zero. The exact mechanisms via which quenching takes place can be found in Barnes paper "Fluorescence near Interfaces" (45), but will be outlined briefly here:

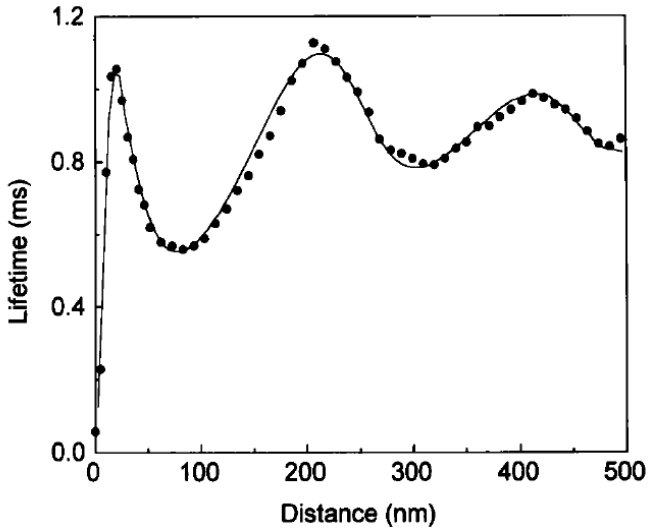

Figure 2.7: The phosphorescence lifetime of Eu^{3+} ions in the presence of an Ag mirror, as a function of separation distance between the ions and the mirror, taken from (45), where the solid line is a theoretical fit.

The process of quenching, by which energy is transferred from the dipole to the dielectric, occurs on length scales less than $\lambda/4$. In order for this transfer of energy to occur from the molecular dipole to the exciton, both energy and momentum must be conserved. As such, the three quenching mechanisms are as follows; firstly, the dipole energy can be absorbed by the bulk of the dielectric, where momentum occurs due to scattering from impurities and phonons (intraband), as well as crystal potential (interband) scattering. Secondly, energy can be absorbed when an exciton is formed on the surface of the dielectric, and this time scattering from the surface potential allows for momentum matching. Finally, in the case when a molecule is in very close proximity to the surface then it is possible the required momentum to couple into the surface may be provided by high-wave-vector components in the dipole near field. Further detailed discussion of the relative importance of each of these methods of quenching is beyond the scope of this thesis, but can be found in (45) should the reader be interested.

2.3.5 Comparison of the Classical Model to the Quantum Model

The classical model described above is an approximation of a quantum process, and therefore it is necessary to make sure that the results of the classical model are comparable

with quantum results. Spontaneous emission from a two level fluorophore occurs at a transition rate k which, when calculated using perturbation theory, is described as Fermi's Golden Rule (40)

$$k = \frac{2\pi}{\hbar}\left|\langle f|H'|i\rangle\right|^2 \rho\left(E_{i\to f}\right) \tag{2.36}$$

where the transition rate is said to be given by the matrix element of the perturbation, H', between the initial, i, and final, f, states multiplied by the density of states at the transition frequency, $\rho\left(E_{i\to f}\right)$, also known as the optical field density, or the photonic mode density (PMD) (45,47).

This model agrees well with the classical theory outlined above. In the classical model variation in the incident image field results in a modification of lifetime, and similarly when the image field is modified, the PMD is similarly modified. Indeed, the classical prediction of the modified decay rate agrees with the quantum prediction, although the classical model is found to underestimate the frequency shift, with the quantum model yielding a more accurate estimate (48).

2.3.6 Fluorescence Near a Small Gold Sphere

Having outlined the mechanisms by which fluorescence is enhanced in the previous sections, it is useful to briefly look at a worked example. Figure 2.8 is taken from a paper by Huang and Richards (49) wherein the mechanisms for fluorescence enhancement near a gold tip are discussed. It will be the basis for a brief discussion of fluorescence in the region of a small gold sphere.

Firstly, it is worth noticing that in each graph shown above an optimal enhancement of fluorescence is observed at a fluorophore to nanoparticle distance of the order of a few nanometres, or a few tens of nanometres, depending on the specific conditions of the fluorophore and the nanoparticle. This is due to the balance between fluorescence quenching and fluorescence enhancement, as explained in section 2.3.5.

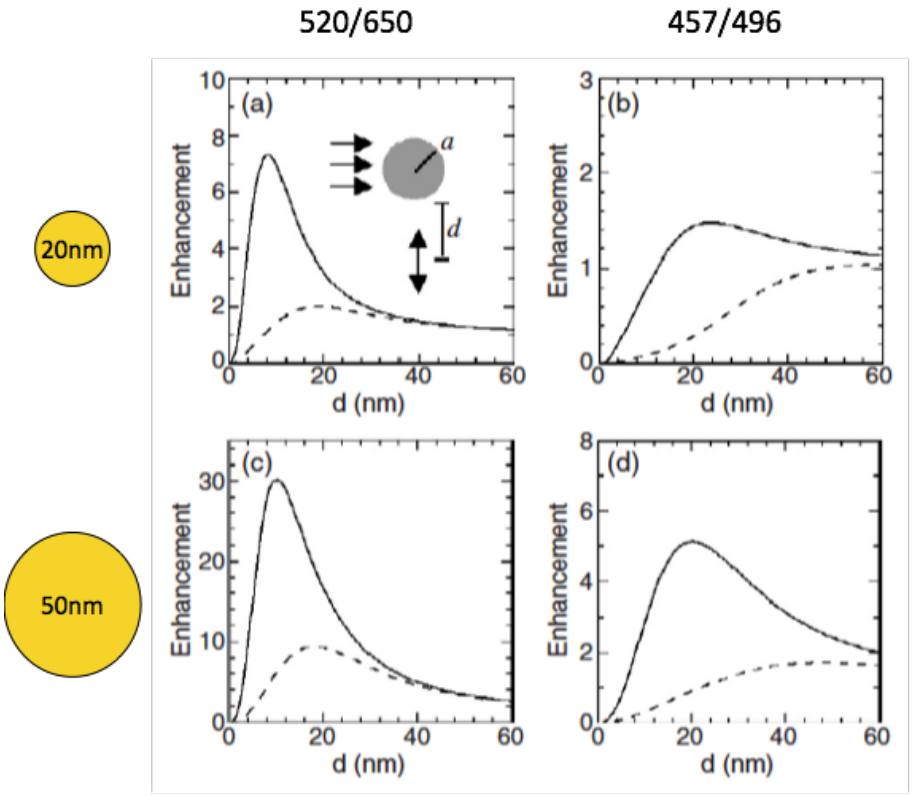

Figure 2.8: A schematic taken from (49), this shows the enhancement observed in a fluorescent dipole in the region of a gold nanoparticle. The configuration is shown in the inset in a), and the incident light polarization is parallel to the dipole orientation. Dashed lines indicate a quantum yield of 1, and solid lines a quantum yield of 0.1. The radius of sphere is 20nm for graphs a) and b), and 50nm for graphs c) and d), with a) and c) having excitation and emission wavelengths of 520nm and 640nm respectively, and b) and d) of 457nm and 496nm respectively.

Also, variation in quantum yield causes a huge variation in both the spatial location of the fluorescence enhancement, that is the distance between the nanoparticle and the fluorescent molecule where enhancement is optimised, and the extent to which the fluorophore is enhanced. The smaller quantum yield fluorophores display a much larger enhancement than their large quantum yield counterparts. This is due to the fact that when considering enhancement of emission, if quantum yield is already 1 then all decay is radiative, and then efficiency cannot be improved. However if quantum yield is small there is a large non-radiative decay component, and in that case the presence of a gold nanoparticle and the subsequent modification of the local field can open up additional radiative decay pathways, thus enhancing the fluorescence intensity.

The size of the sphere will also have an effect on the enhancement. According to the quasi-static principle, which was briefly outlined in section 2.2.2 the larger the sphere the stronger the observed enhancement. This is due to the fact that, a larger sphere will produce a larger local field enhancement, and consequently a greater effect on the radiative decay rate, while the non-radiative decay rate undergoes less modification.

Finally, the LSPR of the gold nanoparticle will determine the relationship between excitation and emission wavelength, and fluorescence enhancement. The enhancement of the local electric field and the transfer of energy are both processes with some resonant frequency, as shown in section 2.2.2, and thus the enhancement of the local field is dependent on the incident light wavelength. The LSPR of the small gold nanoparticle in this system is taken to be around 520nm, and it can be seen from figures 2.8a) and 2.8c) that enhancement is at a maximum either when this LSPR coincides with the excitation of the fluorophore, and is far from the emission of the fluorophore. Conversely, when excitation occurs far from the location of the LSPR and emission of the fluorophore instead shows some overlap with the LSPR, the extent of the fluorescence enhancement is much smaller.

2.4 Summary

This chapter has provided a definition of a surface plasmon, and an explanation of their origin, and shown that the effect of confining such a SP to some sub-wavelength nanoparticle is a localized surface plasmon resonance, or LSPR. Additionally the concept of modification to fluorescence emission in the presence of some metal surface, via a modified local electric field, was discussed, as well as how this field enhancement specifically affects the excitation and emission of the fluorophore. Finally this chapter briefly addressed the specific enhancement observed in the region of a single nanoparticle.

Chapter 3 - Experimental Methods

3.1 Chapter Outline

A wide variety of measurement and fabrication techniques were used during this thesis. This chapter aims to outline the most important measurement techniques and offer brief discussion as to their suitability for the task and to describe the fabrication techniques utilised. Fluorescence lifetime microscopy (FLIM) and Time Correlated Single Photon Counting (TCSPC) are described, as well as other interrogation techniques such as extinction and emission spectroscopy, dark field imaging and atomic force microscopy.

All measurements are carried out on an inverted confocal microscope where sample scanning is performed using a piezo-stage. Samples are then illuminated with a supercontinuum laser, acting as the source for both time resolved fluorescence, and dark field light scattering microscopy and spectroscopy, the mechanism for which will be discussed in more detail later on. The specific details of both the fluorescence and dark-field configurations will be discussed in more detail in the following sections.

3.2 Fluorescence Lifetime Imaging

3.2.1 Confocal Imaging Setup

As mentioned previously, all FLIM measurements are all carried out on an inverted confocal microscope (Nikon TE2000-E, Nikon Corporation, Japan). Samples are excited by a supercontinuum laser (SC-450-2; Fianuim, UK) of pulse repetition frequency 20MHz and pulse duration of 400fs. This acts both as the source for time-resolved fluorescence measurements, which will be outlined here, and dark field light scattering microscopy, which will be described later on.

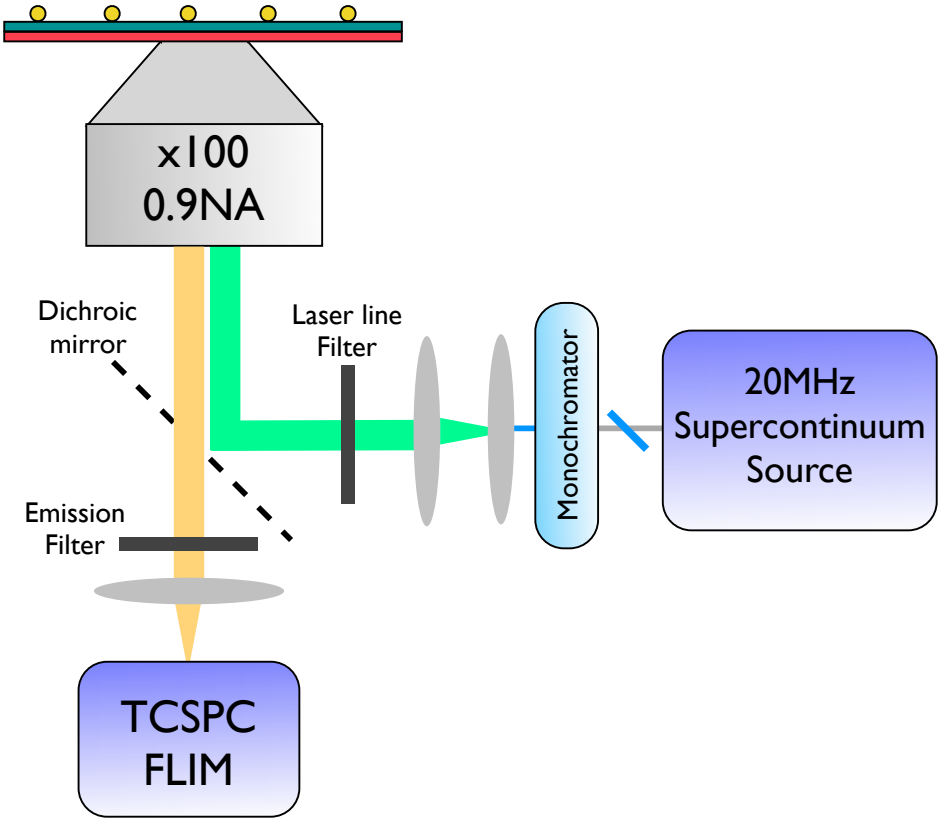

Figure 3.1: The confocal FLIM setup used in this project.

As can be seen in figure 3.1 light from the supercontinuum source is passed through a prism monochromator and laser line filter to determine excitation wavelength. This system allows excitation at a broad range of wavelengths, although typically excitation occurs between 488nm and 532nm. Once focused on the sample the laser power is then adjusted until photon count rates are between 10^3 and 10^5 photons per second – the power required to achieve this varies from sample to sample, depending on dye concentration, and the quantum yield of the dye, but power does not exceed 2mW.

Initial measurements, before the implementation of the dark field system, were performed with a 100x, 1.45NA oil immersion lens (Nikon Corporation, Japan). The bulk of the subsequent measurements were then performed with a 100x, 0.9 numerical aperture (NA) air objective lens (Nikon Corporation, Japan) – this switch occurred due to the requirements of dark field microscopy, which will be explained in section 3.5.

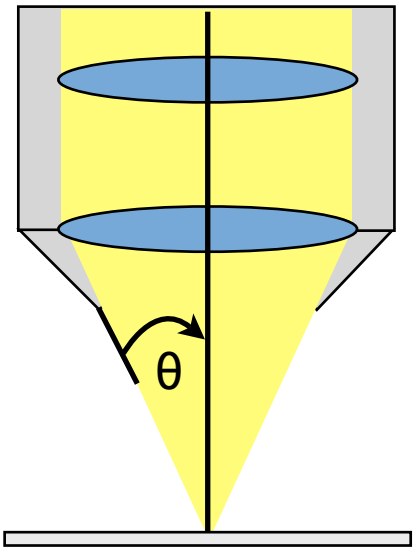

Figure 3.2: The angular aperture, θ, as dictated by the numerical aperture of the lens.

Without considering the requirements of dark field microscopy, both of these objectives have different advantages and disadvantages. The numerical aperture, NA, describes the angles over which the lens can accept light, and takes the form

$$\mathrm{NA} = n \sin\theta \tag{3.1}$$

where n is the refractive medium between the sample and the objective lens, and θ is half of the angular aperture, as shown in figure 3.2. The larger the numerical aperture, the greater the capacity of the lens to collect light, and so in principle, the larger the numerical aperture the better. However, oil immersion lenses can be problematic in that they lose focus comparatively quickly, and the oil they require means that samples can only be imaged via a coverslip, otherwise the sample will likely be irrevocably damaged.

The sample is then scanned through the focused laser beam using a piezo-flexure stage (Newport XY Translation Stage, Model M406). The laser light is directed through a dichroic mirror and an emission filter – the specific filters used for each detection scheme will be described in each of the relevant results sections. Emitted light is then detected using an avalanche photodiode (Id-100; Id Quantique, Switzerland) and a synchronized time correlated single photon counting (TCSPC) module (SPC-150; Becker and Hickl, Germany), the mechanism of which will be explained in section 3.3.

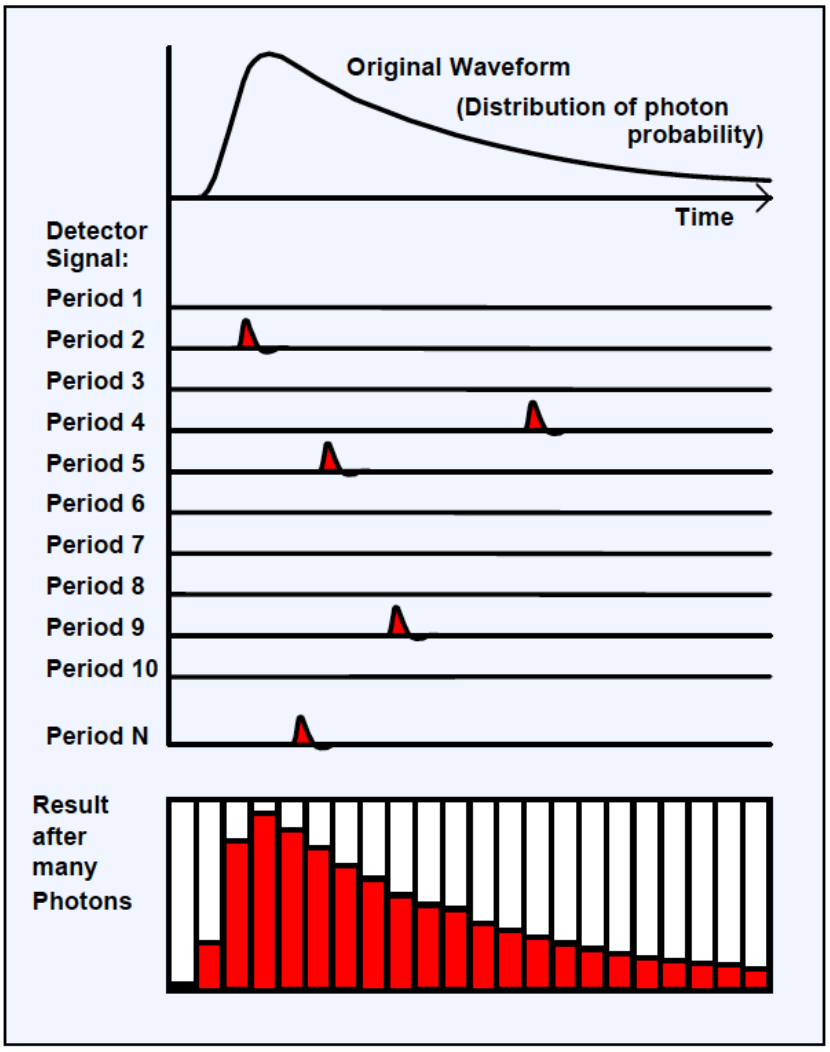

Figure 3.3: The principle of the TCSPC technique, taken from (50). A histogram of many photon detection events is created, forming a distribution of photon probability.

3.3 Time Correlated Single Photon Counting (TCSPC)

The principle of TCSPC is as follows; a high frequency pulsed laser is used to excite single photon emission, and TCSPC then detects the location and arrival times of individual photons from this periodic light signal. For a high frequency signal detected at low light levels it can be assumed that no more than one photon is detected in each 50ns signal period (50). Upon the detection of a photon the arrival time of the pulse induced in the detector is measured, and over many consecutive signal periods a histogram of arrival times builds up. This histogram represents a distribution of the probability that a photon was emitted at any given point, and a pictorial depiction of this process can be seen in figure 3.3.

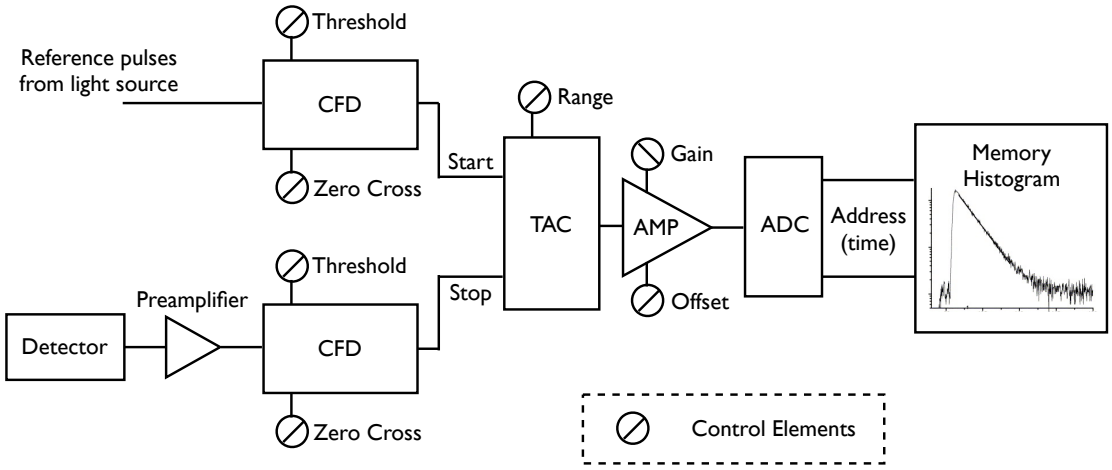

Figure 3.4: A standard TCSPC instrumentation.

3.3.1 TCSPC Instrumentation

The instrumentation of the classic TCSPC setup takes the form seen in figure 3.4 (51). Upon the arrival of a single photon at the detector a pulse is produced. The detector amplitude is random, and so a Constant Fraction Discriminator (CFD) is used to threshold the signal produced by the photon in order to ensure that the timing of the pulses isn't biased. Similarly a CFD is used to obtain a trigger pulse from the laser for timing reference. Both of these pulses are then passed to the Time Amplitude Converter (TAC), which measures the arrival time of the photons with respect to the reference pulse from the laser by using the trigger pulse to turn on a current charging a capacitor, and the photon arrival to turn the current off. The charged capacitor is then converted to a voltage and passed through a biased amplifier (AMP) to amplify the signal, which then passes to the Analog-to-Digital Converter (ADC), which determines the arrival times of the photons.

There are certain factors that determine the maximum signal detectable via TCSPC. Firstly, the time that it takes for the detector and electronic system outlined above to process the detection of a photon is not infinitesimally small, and therefore while this processing is happening, a subsequent photon event cannot be detected. This is known as "dead-time", and decreases the possibility that a photon will be detected, and so acquisition time must be increased to ensure sufficient photon counts are collected. Additionally, should more than one photon arrive within the detection period this can cause a distortion in the form of the

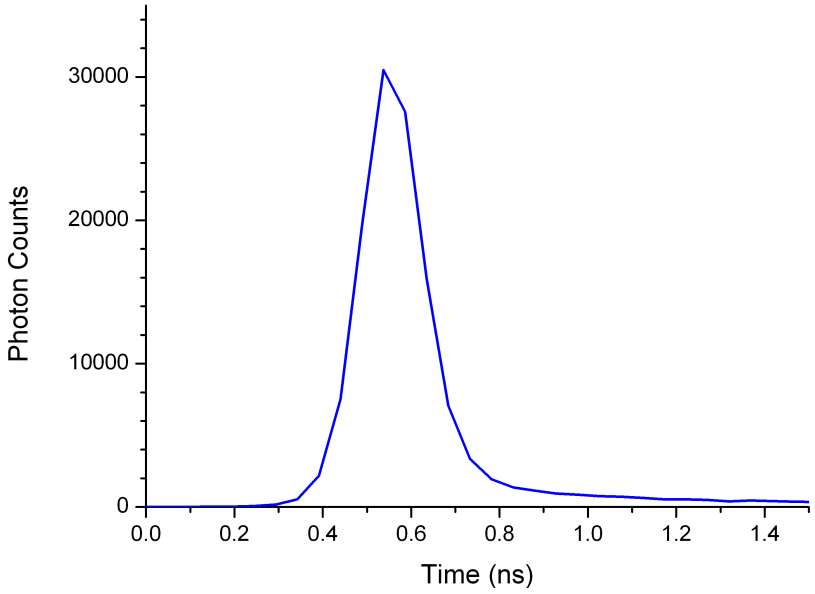

Figure 3.5: The instrument response function (IRF) from the avalanche photo diode (APD) used in all the experiments in this thesis. The FWHM is estimated to be 120 ps.

fluorescence decay – a problem known as "pile-up" (52). In order to avoid this the excitation rate, and hence the detection rate can simply be decreased, thus minimising the likelihood of multiple photons hitting the detector in each cycle.

3.3.2 Time Resolution of TCSPC

The time resolution of the lifetime measurement depends on the accuracy at which the arrival time of individual photons can be determined. This in turn relies on three factors – the repetition rate of the pulsed laser, the Instrument Response Function (IRF) and the Transit Time Spread (TTS). Additionally it is inappropriate to use TCSPC to measure a fluorescence lifetime that is longer than the signal period between pulses, but as all fluorescence lifetimes within this thesis – which vary from around 1ns to 6ns – are significantly shorter than the signal period of 50ns this presents no problem.

The achievable resolution of the instrument depends on the Instrument Response function (IRF) of the single photon counting avalanche photodiode (SPAD), determined from a sample with no lifetime, a value typically collected by reflecting a small amount of laser light off a scattering sample with no emission filter. This response decay profile is indicative of the

shortest decay that can be measured by the instrument, and the width of it depends both on the detector itself, and the system electronics. The response of the APD used for all experiments in this thesis can be seen in figure 3.5. In this case the full width half maximum (FWHM) is estimated to be 120 ps.

In both PMTs and avalanche photodiodes there is a varying time delay between the absorption of a photon at the photocathode and the corresponding output pulse at the anode – an effect known as Transit Time Spread (TTS). In a SPAD variation on the depth at which photons are absorbed contributes to different carrier avalanche conditions, and therefore to different avalanche transit times. The penetration depth of the light in question will therefore depend on the wavelength of the light detected – if detecting over a broad range of wavelengths this will become a more pertinent concern. Additionally in the case of very high photon count rates it is possible that subsequent photons will arrive prior to the recovery of the reverse voltage breakdown caused by the previous photon (53). These considerations mean that the time resolution of the measurements will be improved by only considering a narrow wavelength selection, and by ensuring that the light levels are sufficiently low that no photons arrive prior to voltage breakdown recovery.

3.3.3 FLIM and TCSPC

As described above, a basic TCSPC measurement records the arrival times of photons within a signal period, and through the formation of a histogram of those arrival times, a single 1D signal decay curve is produced. Should information about additional parameters, such as spatial coordinates, be desired, the point of interest must be changed, and a further reading taken. This is a time consuming and inefficient way of interrogating a non-uniform sample (54).

A much simpler option is to record the arrival of photons at the detector not only as a function of time, but of some other parameter also – in this case spatial coordinates. As the sample is scanned through the laser focus a map can be built up, where each individual pixel is assigned a signal decay curve. A sample image is shown in figure 3.6.

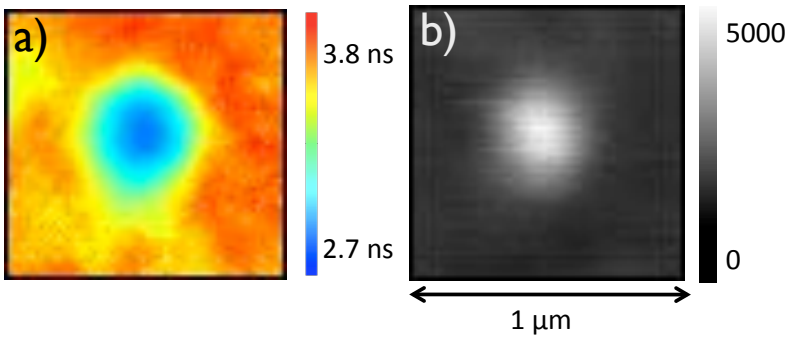

Figure 3.6: a) A sample fluorescence lifetime image, and b) its fluorescence intensity counterpart.

TCSPC is not restricted to collecting only spatial information; it can also be used to measure different wavelengths, time from the start of the experiment, or indeed any parameter of either the photons themselves, or the state of the experiment. However, in this thesis only spatial information is required.

3.4 Extinction and Spectroscopy

Extinction spectroscopy is a technique that involves the measures of the degree to which incident light is absorbed or scattered by a sample. A beam of light of known wavelength and intensity is incident upon a sample, and the transmitted light is measured and compared to the incident light. Extinction spectroscopy is broadly used in this project, both for the examination of dye spectra, and for the determination of LSPR values for large plasmonic nanostructures.

Two systems were used to acquire the extinction spectra. The first was a Perkin-Elmer UV800 dedicated extinction spectrometer. This was appropriate for looking at large sample areas, as the aperture within the spectrometer allowed a 1mm x 1mm region to be examined, which made it ideal for dye spectra measurements. This setup would then scan a monochromatic beam incident on the sample though some pre-determined range of the electromagnetic spectrum (usually the visible range) and would measure the transmitted intensity at each wavelength. Then using the Beer-Lambert law

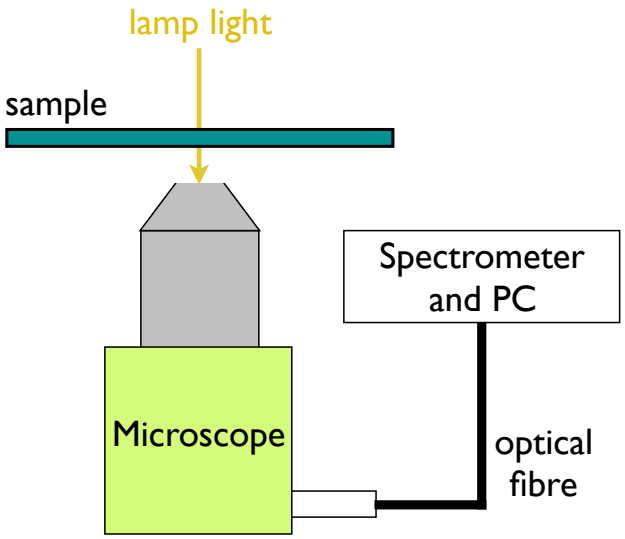

Figure 3.7: Schematic of the setup used to obtain extinction spectra using the inverted microscope.

$$I(\lambda) = I_0 \exp\left(-\alpha(\lambda)\Delta x\right) \tag{3.2}$$

where I_0 is the incident light intensity, $\alpha(\lambda)$ is the extinction coefficient, and Δx is the thickness of the material through which the beam passes, the extinction coefficient can be calculated for each wavelength, and an extinction spectra can be generated. This setup is ideal for interrogating large uniform samples, but since the examination region couldn't be substantially reduced, was unsuitable for non-uniform samples, or individual nanostructures.

The alternative setup used to make these measurements is shown in figure 3.7. It is a modification of the confocal microscope setup, which consists of a lamp producing light incident on the sample, which is then collected and focused collected onto the core of a 365µm optical fibre, which gives a detection area on the sample of roughly 3µm, due to the x100 magnification of the lens. The fibre is then coupled into a spectrometer (AvaSpec-2048, Avantes, The Netherlands). Unlike the dedicated spectrometer, this setup doesn't scan through the visible spectrum, but instead a white light source is used and the collected wavelengths are binned to produce a spectrum. This setup when used as in figure 3.7 was appropriate for either dye extinction or bulk LSPR measurement, but could also be used to

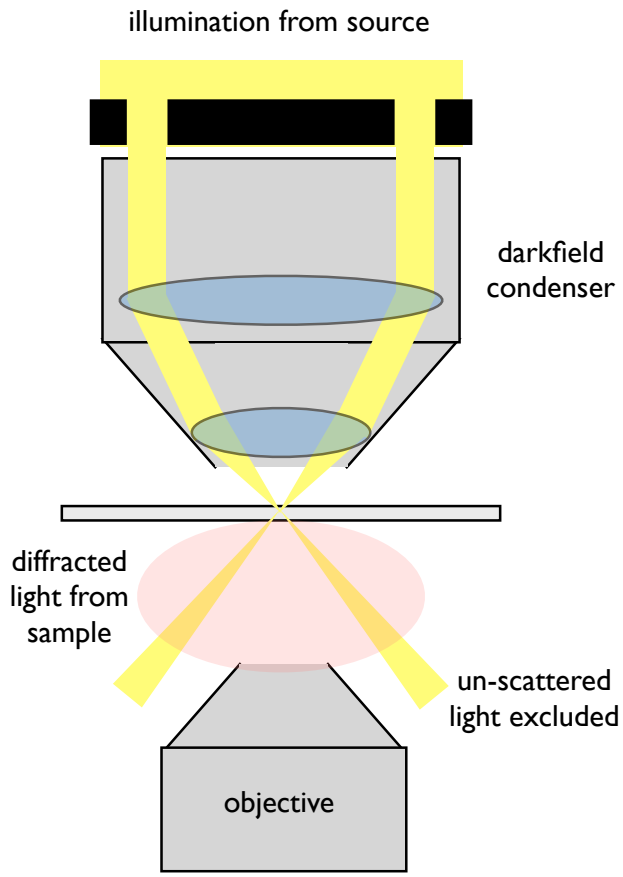

Figure 3.8: An optical scheme for a standard condenser dark field setup.

measure emission spectra when instead the sample was illuminated with a laser, and the light filtered through a laser line emission filter.

This setup proved an appropriate method for measuring much smaller areas of interest, either in bulk nanostructure samples or dye samples, but even with a small optical fibre it was impossible to detect the absorption spectra from individual gold nanoparticles, either those 60nm or 100nm in diameter. This was due to a poor signal to noise ratio because of the relatively tiny size of the nanoparticle in comparison to the detection area. In order to determine the LSPR of an individual nanoparticle, dark field microscopy was necessary, using the methods outlined in the following section 3.5.

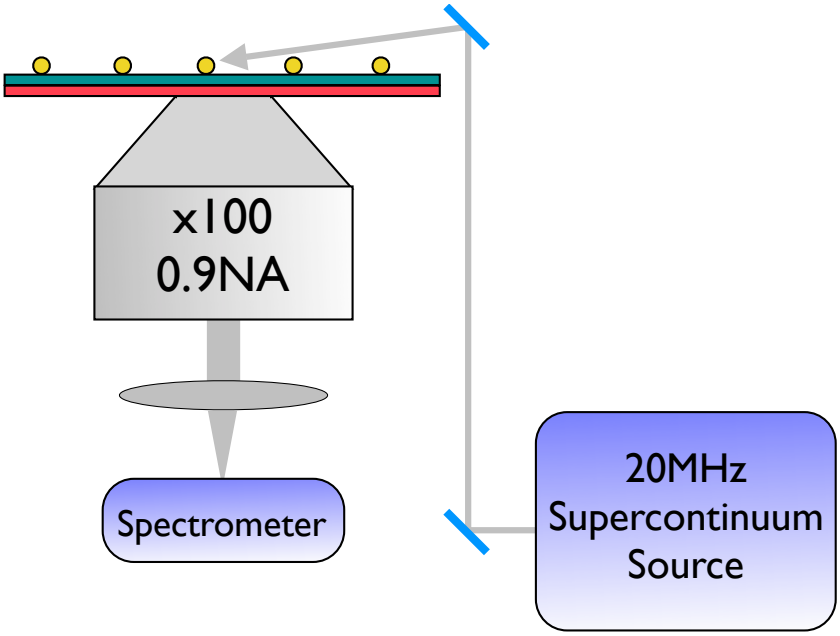

Figure 3.9: The setup used in this project for darkfield imaging. Light is incident at a very high grazing angle so only the light scattered by the individual gold nanoparticles will be focused onto the spectrometer.

3.5 Dark Field Imaging

Dark field microscopy is used in this project both for the location of individual nanoparticles, and also to measure the spectra of scattered light from them. It differs from conventional transmitted light microscopy in that in transmitted light microscopy both the un-diffracted and the scattered light rays are collected by the objective. However when imaging a sample where the un-diffracted component far exceeds the scattered component the contrast can be very low and so the images are often very bright with poorly visible structural details (55). To combat this, in dark-field microscopy a sample is illuminated and light collected such that only scattered light from the sample is detected, and transmitted light is excluded. This means that small objects that only scatter a small amount of light can be clearly seen against a black background.

Fundamentally, the exclusion of unscattered light rays is achieved by illuminating the sample at some indirect angle, such that direct rays cannot be collected by the objective. The principle of dark-field microscopy and a standard means of achieving this is depicted in

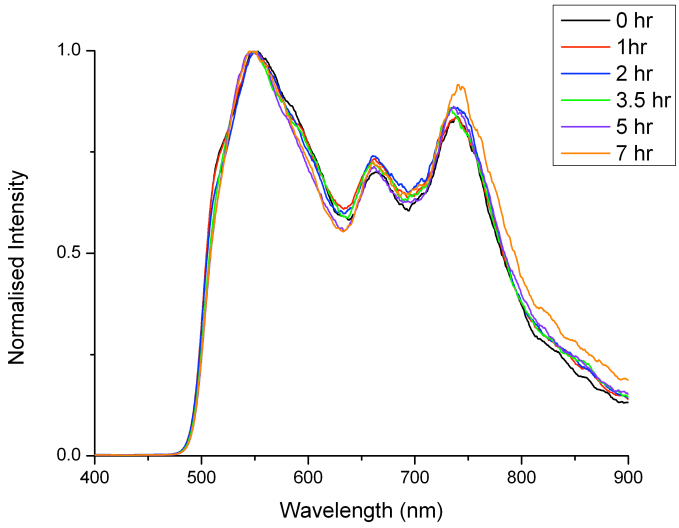

Figure 3.10: A graph showing the structured emission of the Fianium supercontinuum laser. The laser shows huge variation in intensity as wavelength varies, but the spectral shape remains constant over a long period of time.

figure 3.8. Here a portion of the light is excluded by the use of some kind of mask. This means that light incident on the sample is not perpendicular to the surface, and can thus be excluded depending on the angle of collection.

A simpler method, and the one used in this project is shown in figure 3.9 – in this case the sample is illuminated with laser light at a very large incident angle. This allows the collection of scattered light, while the direct illumination from the laser source is eliminated as it grazes off the top of the sample. This is an ideal method because it allows very swift switching back and forward between the wide-field FLIM and dark field setups. Here a CCD camera is connected to the microscope, allowing wide-field imaging of the scattered light, which in turn allows the location of individual nanoparticles to be accurately determined. In order to then measure the scattered spectra and the LSPR of the nanoparticle the scattered light is collected onto the core of a 365µm optical fibre, which gives a detection area on the sample of roughly 3µm. The fibre is then coupled into a spectrometer (AvaSpec-2048, Avantes, The Netherlands), which allows light scattering spectra to be obtained.

The only problem with this setup is that the laser light used for illumination is a highly structured source, as seen in the laser stability graph in figure 3.10. As such data needs to

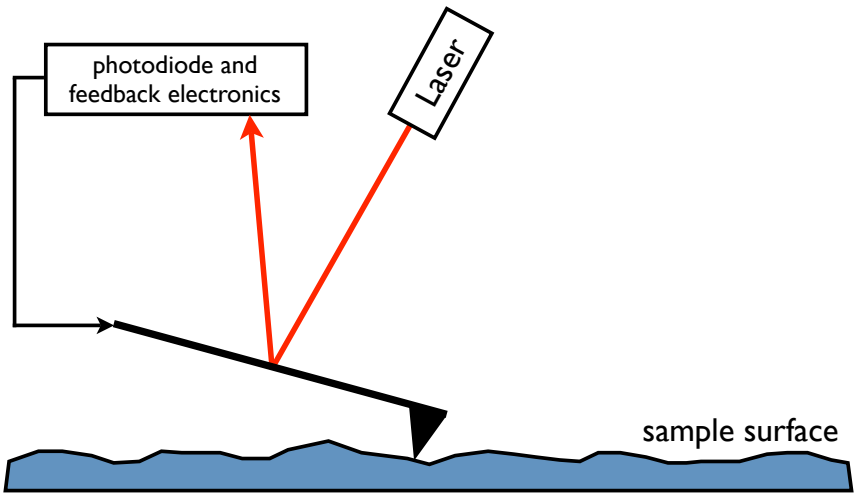

Figure 3.11: The tapping mode configuration for AFM, used in this project.

be normalised with respect to this laser spectrum to ensure that LSPR spectrum peaks are not a result of the structuring of the laser.

3.6 Atomic Force Microscopy

The atomic force microscope (AFM) was developed in 1986 by Binnig and his colleagues (56) as a development of their Nobel Prize winning scanning tunneling microscope (STM) (57). The resolution of AFM is inferior to STM, but it can be used with both conducting and non-conducting samples. The AFMs used in this project are a Veeco Explorer with a 100x100µm Topometrix scanner and a Bruker Ikon, both of which are used with sharp Veeco/Bruker tips with an approximate radius of curvature of 10nm.

AFM measures the force between a sharp oscillating tip and the sample, in a configuration that can be seen in figure 3.11. The general principle of the AFM is that it works by raster-scanning the tip across a sample, and measuring the change in the force exerted on the tip by defects or topological features on the sample surface.

There are two primary AFM configurations and both will be outlined here, although only the latter is used for imaging in this thesis. Firstly, the AFM can be used in contact mode. This means that the tip remains in contact with the surface as it moves across it, and any interaction with topological features on the surface will cause variation in the force acting

on the tip and will result in tip deflection. This detection is measured by determining the degree to which a laser spot reflected off the back of the cantilever is deflected. The electronics within the AFM then compensates for the alteration in force, and adjusts the height of the cantilever in order to keep the force on the cantilever constant. This alteration in height is monitored to form a topographical image of the sample.

Alternatively, and preferentially in this project, the AFM can be used in tapping mode. This, as the name suggests, involves tapping the surface with a tip oscillating at the resonant frequency. The tip is scanned over the sample and as it encounters topographical features on the sample surface the force exerted on the tip alters, as in contact mode AFM. The difference in force alters the amplitude of the oscillating cantilever, and the electronics alter the tip height above the sample such that the amplitude of oscillation does not change. The alteration in force exerted on the tip is measured as a function of the tip position in order to form a topographical image. Tapping mode AFM is preferable to contact mode AFM as dragging a tip along the surface is likely to damage both the tip and the surface, whereas in tapping mode the tip makes less contact with the surface and so damage to either is less likely.

Generally AFM resolution in the sample plane, that is in the x and y axes, is dependent solely on the radius of the tip, but resolution perpendicular to the plane, that is in the z axis, can be much higher depending on the nature of the surface in question. However there are a number of factors that can cause AFM image quality to be adversely affected and the resolution to be decreased. If the tip is not sharp, or if there is some artifact on it – a common occurrence when the tip has been in use for some time – it is possible that this artifact will hit the surface rather than the sharp point of the tip. Occasionally the tip will encounter some dust or loose debris on the surface and it will become stuck to the tip and until shaken loose, either by the action of scanning or by some external interference, the tip will essentially be useless. Tips and samples therefore need to be treated with the greatest of care in order to prevent these issues.

AFM is used in a variety of different ways in this project. It can be used to measure the surface roughness of a sample, surface topography, and also – if a scratch is made – the thickness of a deposited layer. When measuring the thickness of a deposited layer, a small scratch is made in the layer, conventionally using a razor blade, ensuring that the substrate on which the layer is deposited is not scratched and creating a valley in the deposition layer.

AFM can then be used to measure the thickness of the layer. Care must be taken, as at the "cliff edge" there might be a small region where debris from making the scratch piles up, and therefore it is prudent to measure the height difference between the bottom of the valley, and some distance further away from the edge.

3.7 Sample Fabrication Techniques

This subsection is dedicated to an explanation of the techniques used in sample fabrication, while the configuration of the samples themselves will be discussed in the later chapters. Unless otherwise stated, all chemical consumables were purchased from Sigma Aldrich.

3.7.1 Glass cleaning

Prior to sample deposition all the glass coverslips are thoroughly cleaned to ensure that no traces of organic matter remained on the surface, and to make sure that the glass surface is highly hydrophilic. Both of these characteristics are essential to ensure a high sample quality. All glass is initially rinsed in de-ionised water, and then fully submerged in an acid piranha solution consisting of 1 part Hydrogen Peroxide (H_2O_2) to 4 parts concentrated Sulphuric Acid (H_2SO_4) for an hour. The glass is thoroughly rinsed in de-ionised water once again, and then submerged in a base piranha consisting of 8 parts deionised water, one part Hydrogen Peroxide, and one part Ammonium Hydroxide (NH_4OH). The solution is then heated to around 60°C to activate the reaction and left for an hour, at which point the coverslips are thoroughly rinsed again, and stored submerged in deionised water and covered to make them air tight. Once cleaned the coverslips can be stored for up to a week depending on their use, but if left longer than that they will lose their hydrophilic properties, and therefore best practice dictates that they be used as soon as possible.

3.7.2 Spin coating

Much of the sample fabrication was done using the technique of spin coating, particularly for the deposition of single gold nanoparticles (BBInternational), and for the deposition of dye embedded polymer layers. In this technique a dilute solution is deposited on a surface, and the surface is the accelerated until the desired speed is achieved. The speed of rotation causes the liquid to be forced off the edges of the sample, and the film thins until either the

thickness reaches some equilibrium, or until sufficient solvent has evaporated off, and the viscosity has sufficiently increased to cause the formation of a solid layer.

Much work has already been done determining the optimum polymer concentration and spin speed to produce ultra-thin films of different thickness (58). Initially both PMMA and PVA were considered for use in the polymer films, but ultimately it was decided that PMMA would be a better candidate. It is highly soluble in chloroform, but insoluble in water, which means that nanoparticles suspended in water could be directly spin-coated onto the surface of the dye-embedded polymer if required. Through a combination of use of the existing literature referenced above and a process of trial and error the most appropriate solution concentrations and rotation speeds can be determined – in this case a solution of two parts 0.08% (by mass) PMMA and one part 50microM dye both in chloroform, rotated for 60s at a speed of 4000RPM. It is important that the polymer film contains dye molecules that are sufficiently concentrated that it could be assumed that, within resolution limits, the dye layer is both uniform and continuous, but sufficiently disperse so as not to cause fluorescence self-quenching, as explained in section 1.2.4.

In addition to the spin coating of dye layers, this technique was also used to deposit single gold nanoparticles of varying sizes – 20, 60 and 100nm (BBI Solutions). These gold nanoparticles were purchased in aqueous solution, and the spin coating process was required to produce a monolayer of single gold nanoparticles – either on top of some spacer layer as mentioned earlier, or simply on a hydrophilic glass substrate – sufficiently far apart that they were optically resolvable. Evidence for the success of this technique will be shown in section 4.2.1.

3.7.3 Thermal Evaporation

Thermal evaporation deposition is a technique whereby thin films, often of metals of other dielectrics, are deposited by evaporating the desired material under a high vacuum. When the gaseous particles come into contact with the substrate they condense back into a solid state.

In the thermal evaporation process a small quantity of the material with which the film is to be made is placed in a tungsten evaporation source, or “boat” – a long flat filament with a

small groove in it. A large current is then passed through the boat such that the source material is heated to boiling point, it evaporates, and is deposited onto a sample located directly above. The thickness of the layer deposited is measured using a quartz crystal oscillator positioned adjacent to the sample. As the mass of the source material on the quartz crystal increases the resonant frequency at which the crystal oscillates alters, and therefore knowing the molecular or atomic mass of the material being deposited the thickness of the layer can be calculated.

In general, the higher the vacuum, the higher quality the film deposited. However, a few things need to be taken into consideration when deciding how best to deposit a film. Firstly, the relative ease with which different materials will evaporate will make a significant difference to the quality of film, and what it is possible to evaporate onto. For example, it is considerably easier to evaporate silver, with a boiling point of 2435K, than it is to evaporate gold, with a boiling point of 3129K. Additionally a very slowly deposited film will be smoother than a film deposited quickly. Typically, although this depends on the material being deposited, this means that the rate of deposition will be around 0.1nm per 5-10 seconds. However if the substrate onto which deposition is taking place has any heat sensitivity, care must be taken to balance the desire for a smooth film with the risk of heat damage from prolonged exposure to the hot filament – a concern particularly pertinent when considering deposition onto polymer films. This can partly be addressed by moving the source further from the sample, but will most likely involve some compromise being made with the speed of deposition.

3.8 Summary

This chapter has described the experimental techniques employed throughout this project. These include fabrication techniques such as spin coating and thermal evaporation, as well as a description of sample imaging techniques, including fluorescence lifetime imaging (FLIM) and time correlated single photon counting (TCSPC), extinction spectroscopy, dark field imaging, and atomic force microscopy (AFM).

Chapter 4 - Initial Experiments, Configuration and Analysis

This chapter concerns itself with initial measurements and means of analysis for the samples studied in work described in later chapters. Here alternative configurations and the choice of materials used in the sample will be discussed, as well as measurements that were made to ensure that sample quality was high. Finally, alternative methods of fitting the data will be outlined, and cases made for which is the most appropriate.

4.1 Sample Configuration

The experimental system of interest here is fundamentally a configuration where some quantity of fluorophore is located in the region of some plasmonic nanostructure, and there are a huge variety of ways in which this can be achieved. However, this project is concerned with bulk rather than single molecule properties, and so it was decided to embed the dye in some very thin polymer layer, which allows a highly uniform layer of dye to be deposited over a very large area.

As this project concerns itself with the bulk response of a collection fluorophores to single spherical gold nanoparticles there are then two primary configurations that are used for measurements. The method of fabrication for each will be described, and then the benefits and limitations of each will be discussed in more depth.

4.1.1 Dye-Spacer-Nanoparticle

The first of these is a dye-spacer-nanoparticle sample, as can be seen in figure 4.1. This sample consists of a thin layer of dye embedded in poly methyl methacrylate (PMMA), less than 20nm thick, onto which a spacer layer of varying thickness of silicon dioxide (SiO_2) is thermally evaporated. Finally the nanoparticles are spin coated onto the top of the spacer layer. AFM measurements using the scratch method as described in section 3.6 were used to confirm the thickness of the polymer layer, which was found to be around 20nm.

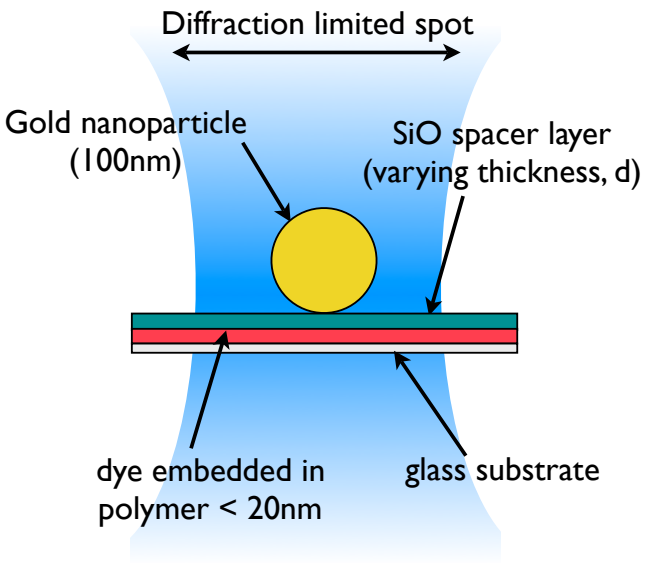

Figure 4.1: Schematic showing the configuration of a Dye-Spacer-Nanoparticle sample.

This sample structure both highly reproducible and well defined. However, for an unknown reason taking dark field scattering measurements from such a structure proved to be very difficult. The ratio of signal to noise was already very low for other LSPR measurements, and in this configuration the noise level was simply too high.

This sample will be used in chapter 5 when considering the variation of intensity enhancement and lifetime reduction with spacer thickness.

4.1.2 Nanoparticle-Dye

The second sample configuration is that of a nanoparticle-dye sample. In this case, single gold nanoparticles are spin-coated onto very clean glass, and then a layer of dye-doped PMMA is spin coated on top. This sample is by far the easiest to fabricate, and by carefully controlling the speed of spin-coating large numbers of very uniform samples can be produced.

The only potential pitfall with this problem is that it's very difficult to know exactly the sample configuration – various possible configurations are shown in figure 4.2. Ideally the sample would conform to either figure 4.2a) or figure 4.2b) as these are likely to be the

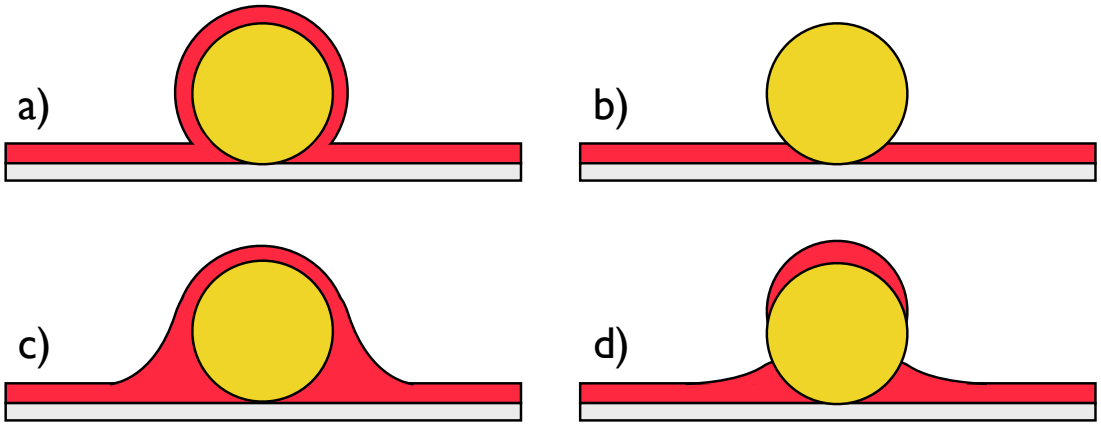

Figure 4.2: Possible different Nanoparticle-Dye sample configurations showing varying degrees of dye-doped PMMA coverage on the nanoparticle.

easiest to model, however the likelihood of there being no dye on the top of the nanoparticle, or a completely uniform layer of dye over the whole nanoparticle is very slim. It is much more likely that some compromise between the two is reached, where some dye is on top of the sample, but potentially not a complete layer as seen in figure 4.2d), or that there is some "pooling" of the dye layer in the region where the distance between the nanoparticle and the surface is at a minimum as seen in figure 4.2c). However, unless detailed modeling of the response of the dye to the nanoparticle is desired, this is potentially not a problem as the sample is still highly uniform and reproducible. This nanoparticle-dye configuration will be used in chapter 6 when discussing the relationship between LSPR and lifetime modification, as it proves ideal for dark-field measurements.

4.2 Sample Quality

The samples produced need to be of a high quality in order to ensure both uniformity between samples and that the data is trustworthy. This means that it is very important to be sure that not only are the deposited nanoparticles well dispersed, but also that they're on very high quality substrates, with low surface roughness. Evidence for both of these characteristics is outlined below.

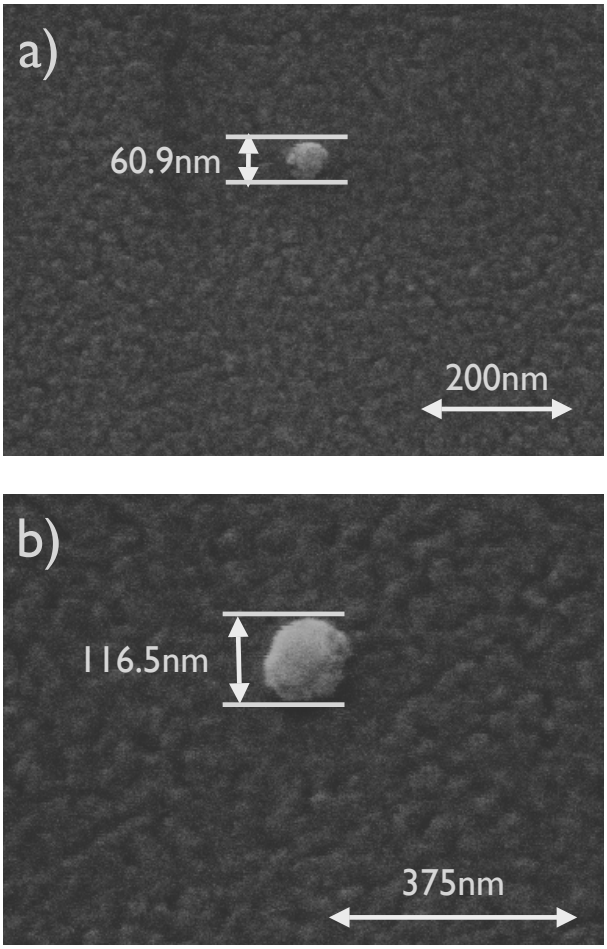

Figure 4.3: SEM images confirming that nanoparticles spin-coated onto a surface do not aggregate. Images are shown for both a) 60nm and b) 100nm gold nanoparticles.

4.2.1 A Single Nanoparticle?

In a sample where features to be imaged are smaller than the wavelength resolution limit it is very difficult to ensure that a single gold nanoparticle, rather than some aggregate of particles, is being interrogated. This is a particular problem when considering smaller gold nanoparticles with a diameter of 60nm – in such a sample it would be quite possible to have a cluster of these particles that could not optically be differentiated from a single gold nanoparticle. It is expected that a nanoparticle aggregate would also cause some fluorescence intensity enhancement, as it too produces a local field enhancement. However in the case of a nanoparticle dimer or trimer, enhancement occurs between the gaps in the nanoparticles and with different modes, and therefore different LSPRs (59). This means

that the strength of the local field enhancement and indeed the wavelengths that it might optimally influence would be quite different from a single nanoparticle case. Therefore, in order to ensure comparability of measurements it is very important to ensure that when nanoparticles are spin-coated onto a sample they do not aggregate. SEM images as shown in figure 4.3 were taken of nanoparticles spin coated onto a glass substrate, both for 60nm particles as in figure 4.3a) and for 100nm particles as in figure 4.3b). The nanoparticles were then coated with a thin layer of gold, around 5nm, to ensure sufficient conductivity for SEM imaging, which explains the discontinuous nature of the substrate and the slightly rough nature of the nanoparticle surface. Regardless of the slight surface and particle roughness, it can clearly be seen that the nanoparticles in these images are single spheres, and not some aggregate of particles. Ten individual nanoparticles were imaged both for 60nm and 100nm gold nanoparticles, and all the imaged nanoparticles were single nanoparticles.

4.2.2 A Smooth Spacer?

In samples where a spacer layer is required it is essential that the spacer be both easily defined and very smooth. Two methods of spacer production were considered, spin-coating a thin polymer layer, or thermal evaporation of a dielectric, in this case silicon dioxide (SiO_2).

Spin coating allows the production of a highly uniform thin film, in a variety of different materials. In the samples of interest in this project, the dye embedded PMMA layer is dissolved in chloroform before it is spin-coated. As PMMA is not water-soluble, this means that a thin layer of a water-soluble polymer, such as polyvinyl alcohol (PVA) which is highly water soluble, can then be spin coated onto the top of the sample without disrupting or dissolving the dye embedded PMMA layer. However, problems arise with this system in terms of determining the thickness of the layer of polymer being deposited. Using calibration curves like those found in (58) it is possible to estimate the thickness of the layer deposited, but to accurately control the layer thickness to within a few nanometres is very difficult.

Since this project required spacer layers of a highly defined thickness, thermal evaporation is a much better option than spin-coating. Thermal evaporation, as described in section 3.7.3,

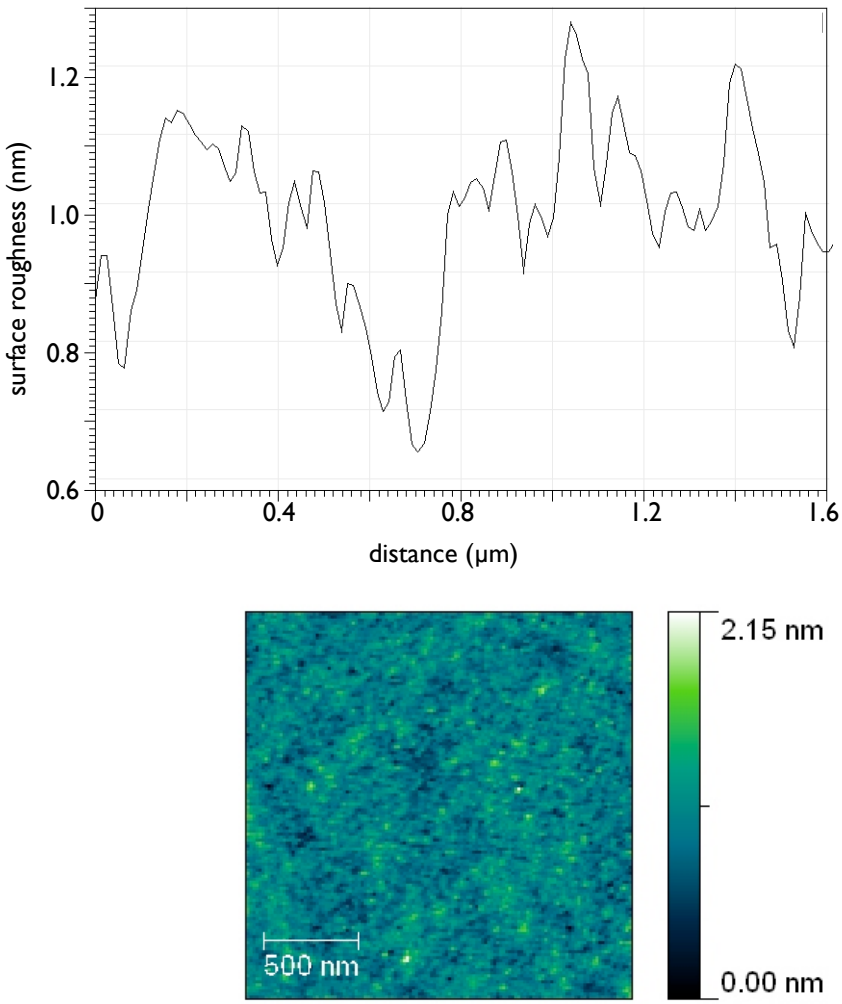

Figure 4.4: AFM images of the surface roughness of a silicon dioxide spacer layer. The variation in the surface roughness is of the order of 1nm.

allows very thin and well defined layers of materials to be deposited. The only consideration, as mentioned then, is as to the speed of deposition, and the material deposited. The two materials considered are silicon monoxide (SiO), and silicon dioxide (SiO_2). Silicon monoxide has a temperature of evaporation of 2153K and a refractive index of 2.29, whereas silicon dioxide evaporates at 2503K and has a refractive index of 1.52 (boiling points from (60) and refractive indices from (61)). In terms of temperature of evaporation this would seem to make silicon monoxide a more favourable choice, but since its refractive index doesn't match the refractive index of the glass, silicon dioxide was used as the spacer in all samples. The refractive index of silicon dioxide is both comparable with

that of the borosilicate glass substrate onto which the dye embedded PMMA is deposited, and with the refractive index of the PMMA itself, which is 1.49 (61).

Having settled on silicon dioxide as the optimum spacer layer material, the primary concern became ensuring that the surface was uniformly smooth. When deposition is particularly quick the smoothness of the film is compromised, and so to ensure that the deposition taking place was sufficiently slowly AFM measurements were taken of the surface, as seen in figure 4.4. Here it is clear that the surface roughness is low, less than ± 1nm.

4.3 Dye Selection

A key factor in sample preparation is the selection of an appropriate fluorescent dye. Various characteristics are taken into consideration when deciding which dyes are most suitable for measurement – quantum yield, excitation and extinction spectra and their overlap with the LSPR of the gold nanoparticles, as well as fabrication concerns like solubility, and the response of the dye to being fixed in polymer. A selection of dyes will be introduced and their characteristics discussed in this section.

4.3.1 Rhodamine 6G

Rhodamine 6G, or R6G, was used for all preliminary measurements in this project. R6G has a high quantum yield of 0.95 (62). Its chemical structure can be seen in figure 4.5a) and its absorption and emission spectrum can be seen in figure 4.5b), from which it is clear that the absorption peak occurs at 530nm and emission at 550nm. It is highly photostable, which means that photobleaching occurs over a long timeframe, and soluble in both water and chloroform. Its unmodified fluorescence lifetime was found to be 3.8 ns embedded in PVA, which means that it is long enough to be measured with a high degree of accuracy. Additionally figure 4.6 shows that the emission only shows a slight environmental sensitivity.

4.3.2 Nile Red

Nile red is a more complicated prospect than R6G. It is very poorly soluble in water, but both highly soluble and highly fluorescent in organic solvents (63), where, depending on how hydrophobic the solvent is, the excitation and emission maxima of the solvent vary by

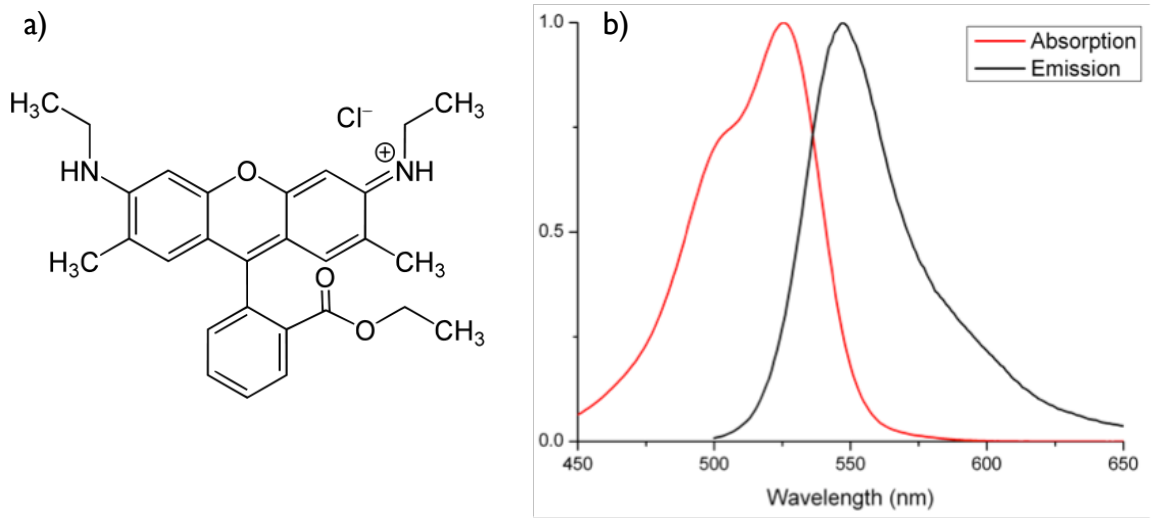

Figure 4.5: a) The chemical structure of Rhodamine 6G. b) The absorption and emission spectra for Rhodamine 6G dye embedded in a thick layer of PVA. The absorption peak is at 530nm, and the emission peak at 550nm.

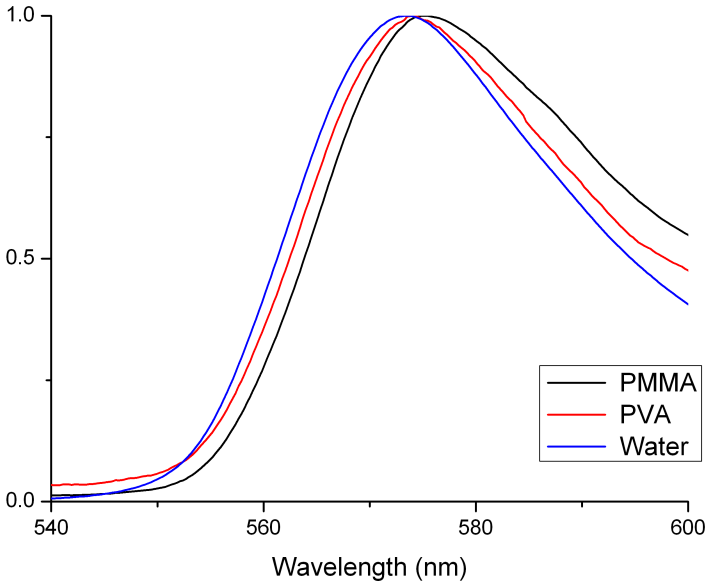

Figure 4.6: The emission spectra for Rhodamine 6G under a variety of different environmental conditions – in solution, or embedded in a thick film (>1µm) of either PMMA or PVA. There is very little change in the shape of the spectra of the peak emission wavelength.

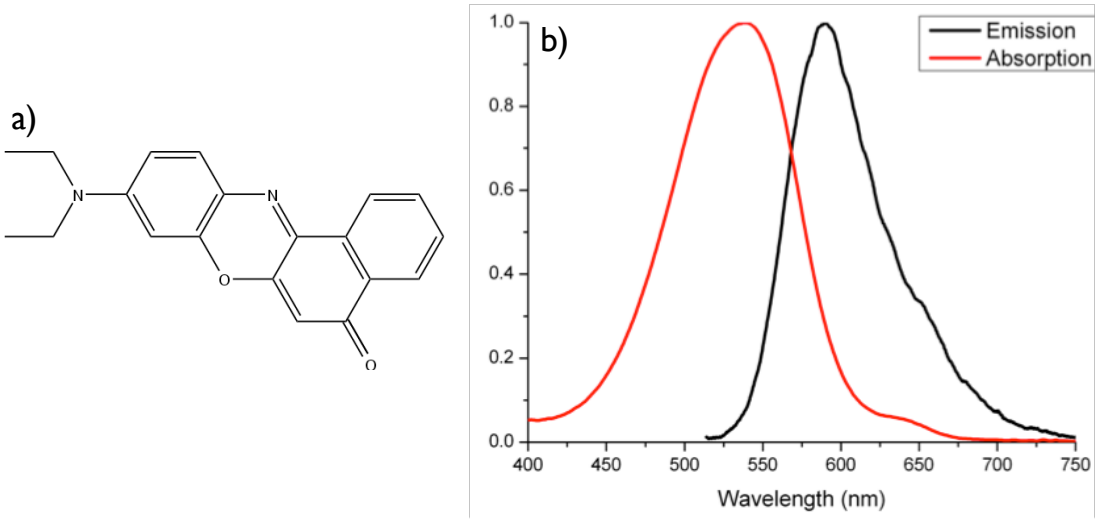

Figure 4.7: a) The chemical structure of Nile Red. b) The absorption and emission spectra for Nile Red embedded in PMMA. The absorption peak is at 537nm and the emission peak is at 590nm.

around 60nm. Fluorescence lifetime and quantum yield also vary depending on the polarity of the environment in which the dye is situated, but similar to R6G Nile Red has both a relatively long lifetime in an organic solvent, typically around 4ns, and a quantum yield around 0.7 (64).

A chemical structure for Nile Red can be seen in figure 4.7a), as well as an absorption and emission spectrum for Nile Red embedded in a PMMA film in figure 4.7b), with an absorption peak at 537nm, and an emission peak at 590nm. Typically unmodified fluorescence lifetime was between 3.2 and 4ns. This dye was used for a number of preliminary measurements but it was decided to use other dyes for final measurements, as depending on the environment it is in the lifetime response of the dye can be complicated and does not necessarily conform to a mono-exponential. This added a potential degree of complexity that was considered unnecessary.

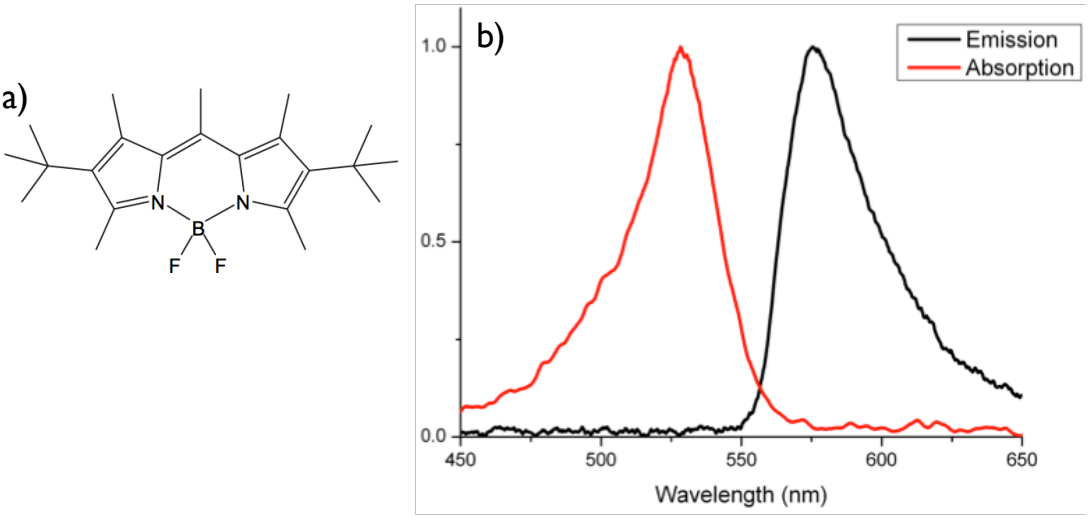

Figure 4.8: a) The chemical structure for PM597. b) The absorption and emission spectra for PM597 embedded in PMMA. The absorption peak is at 526nm and the emission peak is at 575nm.

4.3.3 Pyrromethene 597

Pyrromethene 597, or PM597 (Exciton) is a laser dye. It has a slightly lower quantum yield than the other dyes used in this project, around 0.4 (65). Its chemical structure can be seen in figure 4.8a), and its absorption and emission spectrum can be seen in figure 4.8b), with the absorption peak at 526nm and the emission peak at 575nm. It is highly soluble in chloroform, which was the solvent of choice for PM597 measurements, and shows good photostability. The fluorescence lifetime was measured to be around 6.0ns in chloroform.

4.4 Enhancement in the presence of a Single Nanoparticle

Having carefully constructed the most appropriate samples, it is now prudent to ensure that the samples demonstrate, at the most fundamental level, expected fluorescence behaviour based on the understanding of fluorescence modification gleaned from section 2.3. As such, there are two fundamental questions that it is useful to ask when considering the data – is a modification in intensity observed in the region of a single gold nanoparticle, and is a corresponding modification in fluorescence lifetime observed in the region of the same gold nanoparticle?

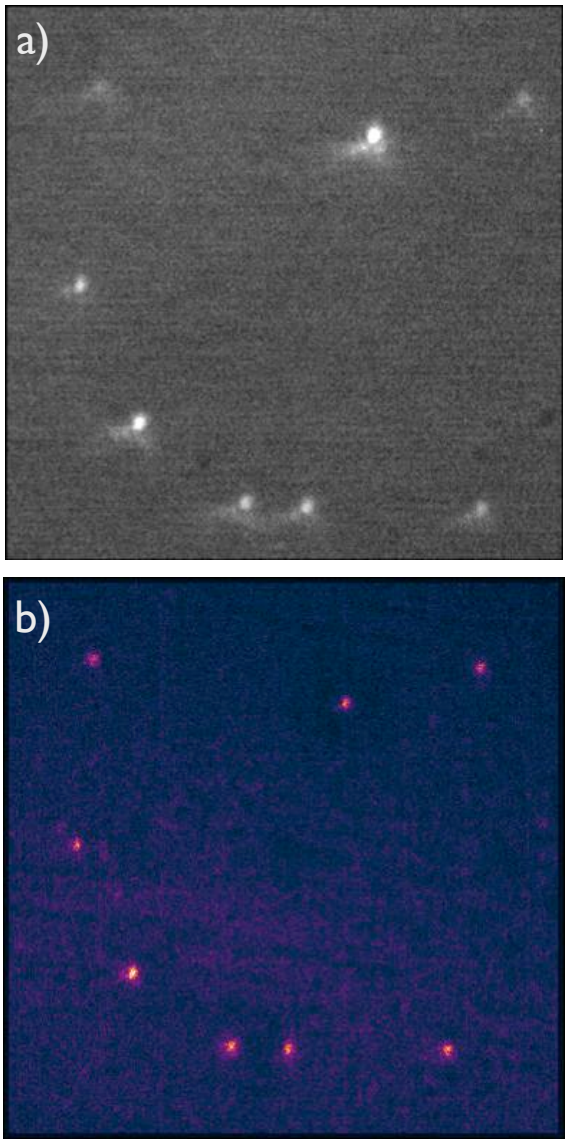

Figure 4.9: a) Dark field image of a 50µm region of a nanoparticle-dye sample. b) A false colour fluorescence intensity image of the same region of a nanoparticle dye sample. A strong correlation between the two images is clearly demonstrated.

Firstly, the case of fluorescence intensity enhancement in the region of a single nanoparticle. This is a simple thing to confirm, as all that is necessary is to check that the dark field image showing the location of the nanoparticles corresponds well to the fluorescence intensity image showing the modification in the region of the nanoparticle. This strong correlation can clearly be seen in figure 4.9, where figure 4.9a) shows the dark field image, and figure 4.9b) shows the fluorescence intensity enhancement seen in a Nile Red sample.

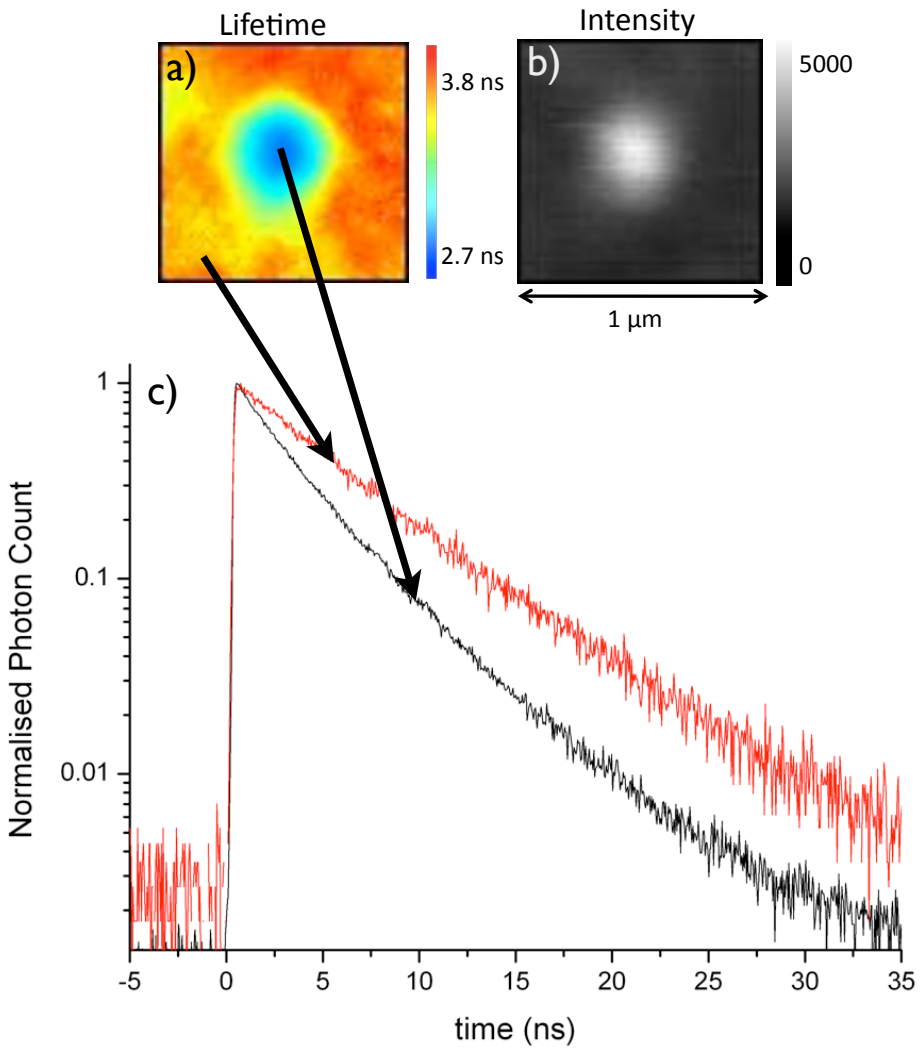

Figure 4.10: a) A 1µm fluorescence lifetime image of the modification observed in Nile Red in the region of a single gold nanoparticle. Lifetime data here is fitted to a monoexponential. b) A 1µm fluorescence intensity image of the modification in the region of a single gold nanoparticle. c) A graph showing the variation in photon counts with time at regions of different lifetime modification.

Secondly, where a modification in fluorescence intensity is observed, a corresponding modification in fluorescence lifetime can also be seen. This is demonstrated in figure 4.10, where a single fluorescence lifetime image of the modification in the region of a single nanoparticle is shown in figure 4.10a), and its fluorescence intensity equivalent in figure 4.10b). Looking at individual lifetime curves in figure 4.10c) it can be seen that far from the centre of the nanoparticle the lifetime is substantially longer than the lifetime observed at

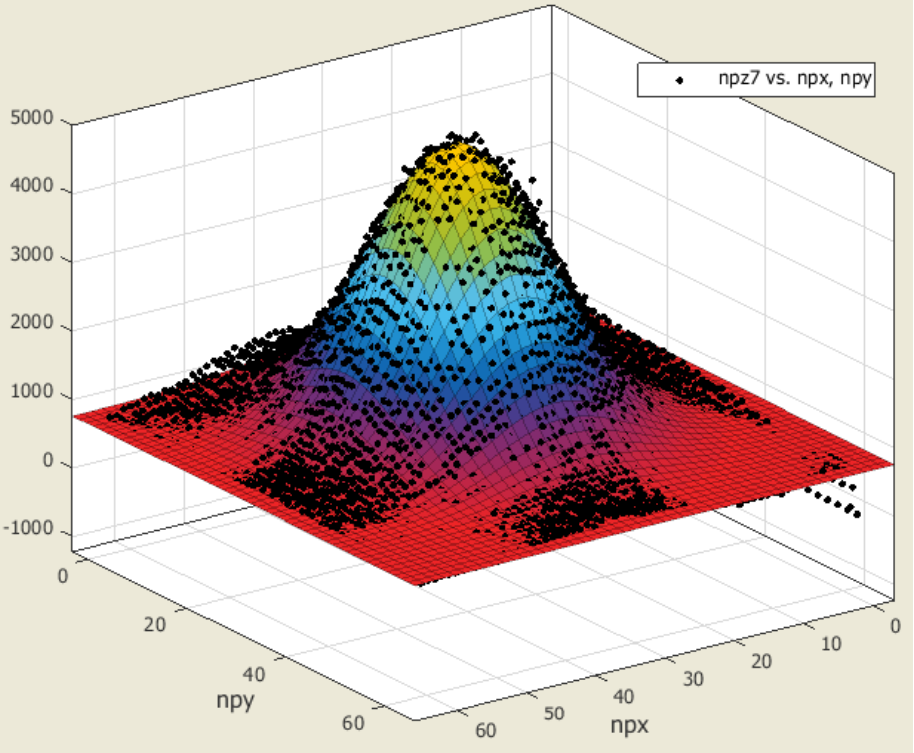

Figure 4.11: A Gaussian surface fitted to intensity data for a single nanoparticle on polymer embedded dye.

the centre of the nanoparticle. This is as expected, and acts as confirmation that the samples do indeed consist of dye in the region of a nanoparticle and this, in conjunction with the information about sample structure seen in section 4.2 confirms a high sample quality.

4.5 Data Fitting

4.5.1 Fitting Methods

Each image collected can be analysed both to determine the modification of the fluorescence lifetime, and the modification of the fluorescence intensity. All single nanoparticle images are 64 x 64 pixels, and measure 1µm x 1µm – significantly over the Nyquist limit, which results in some oversampling, but ensures that sufficient data is collected. The methods for each analysis will be outlined.

Initially the centre of the nanoparticle must be located. In order to do this the data is imported into MATLAB, where fluorescence intensity is then fitted to a Gaussian of the form

$$A = a + b\exp\left(-\left(\frac{(x-x_0)^2}{D_x^{\,2}} + \frac{(y-y_0)^2}{D_y^{\,2}}\right)\right) \tag{4.1}$$

where x_0 and y_0 are the coordinates of the centre of the nanoparticle and D_x and D_y give some measure of the breadth and width of the confocal fluorescence images of the dye in the vicinity of the nanoparticles. Additionally, the prefactors a and b can be used to calculate the intensity enhancement, with the ratio of modified intensity to unmodified intensity given by the equation

$$\eta = \frac{a+b}{a} \tag{4.2}$$

A sample fitting can be seen in figure 4.11. Once the centre of the nanoparticle has been determined and the intensity enhancement calculated, it is then possible to consider the fluorescence lifetime enhancement. This can present a much more complicated scenario than fluorescence intensity enhancement, for a number of reasons.

When considering a uniform sample where only an unmodified fluorescence lifetime is present, the data for all dyes in this project can usually be fitted to a mono-exponential decay. A sample of this data and the fit can be seen in figure 4.12 and it is clear from the residuals shown below that this fit shows a high level of conformity.

Considering now a modified nanoparticle sample, and having found the centre of the nanoparticle using the method described above, the data around the nanoparticle is "binned", which means that rather than taking data from only the central pixel where the signal is highest, data is collected from the entirety of the nanoparticle region. The nanoparticle itself is either 60 or 100nm, and for a 1µm image of 64 x 64 pixels each pixel has a size 15.6 nm. It would then seem that simplest thing to do here is to take the number of pixels that is nearest the size of the nanoparticle – 4 pixels for a 60nm particle, and 6 or 7 for a 100nm particle – and simply bin those. However, additional considerations must be made in order to ensure sufficient photon counts. The more complicated the decay, the

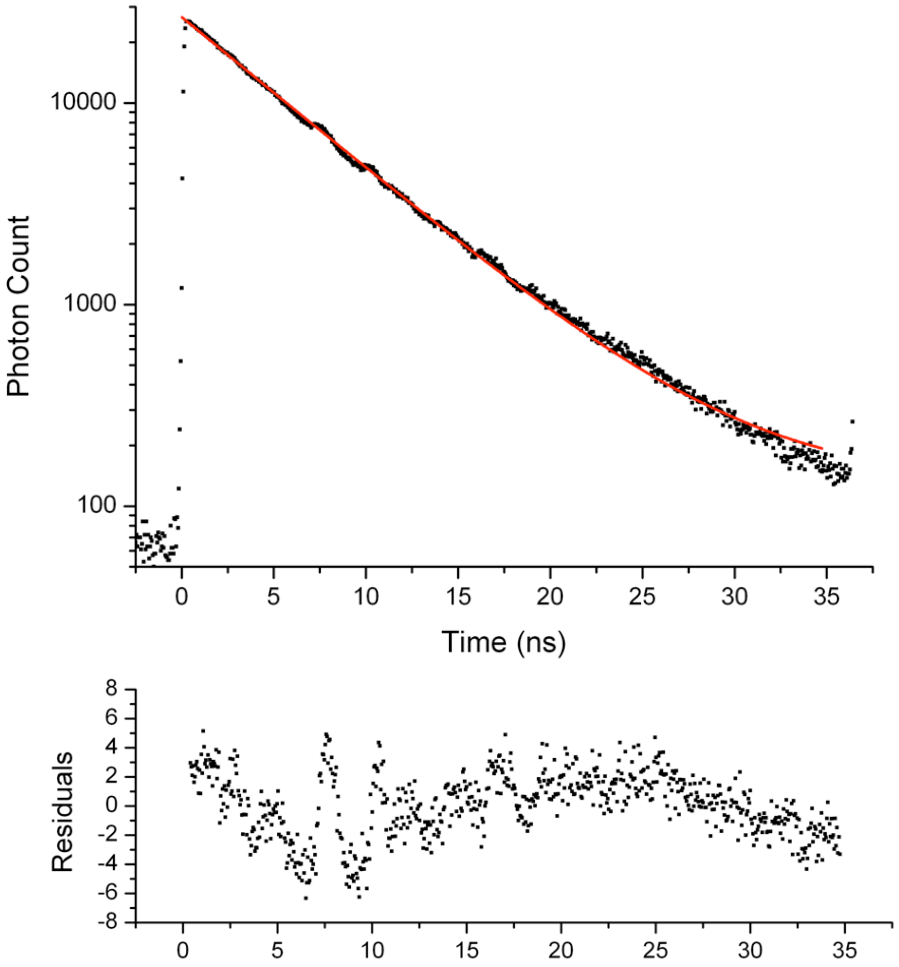

Figure 4.12: An unmodified fluorescence decay data from a PM597 sample, with a monoexponential decay fitted. The χ^2 value is 4.82 with no fit parameters dictated. Underneath the difference between the data and the fit is plotted in the form of residuals (weighted by 1/sqrt(fit)). Despite the relatively high χ^2 value, visually this data conforms reasonably well to a mono-exponential fit. The slight oscillation observed in the residuals comes from unavoidable electrical interference, rather than being an artifact of a poor fit. Additionally the residual size is at least two orders smaller than the magnitude of the maximum decay photon count.

more counts are required to get a good fitting – a mono-exponential fit requires far fewer photon counts than a bi-exponential fit to give the same degree of accuracy. Since, as will be explained shortly, many of the measurements in this thesis require the fitting of a bi-exponential the highest priority is ensuring that sufficient photon counts are taken that a bi-exponential can be confidently fitted. This means that the peak photon count needs to be of the order of 10^3 at the least, and ideally is of the order of 10^4. As such, if a smaller bin does not provide sufficient photon counts, it is prudent to simply expand the bin, but the pros ad cons of this will be discussed in more detail later on.

Choosing how to fit the data from this sample is non-trivial. Measurements are all diffraction limited, so rather than just observing a fluorescence modification where a film of dye is a fixed distance from a film of metal within the spot, there will be many fluorescent molecules at different distances from the metal nanoparticle that optically cannot be resolved. This means that physically, the system conforms to an infinite series of exponentials, which looks like

$$I(t) = A_0 \exp\left(\frac{-t}{\tau_0}\right) + \sum_{m=1}^{\infty} A_m \exp\left(\frac{-t}{\tau_m}\right) \tag{4.3}$$

where τ_0 is the unmodified fluorescence lifetime, and the second half of the equation represents an infinite sum of modified lifetimes. While this equation is physically accurate, it is very difficult to extract any useful information from. An alternative fitting is required, admittedly one which is slightly less accurate, but which will allow a simpler parameterisation of what is being observed. The TRI2 software developed by Paul Barber and his colleagues (66) that is used offers a selection of fitting options, three of which were considered here for fitting nanoparticle data.

Firstly the mono-exponential fit, of the form

$$I(t) = A \exp\left(\frac{-t}{\tau}\right). \tag{4.4}$$

This was quickly ruled out as it fails to take into account the size of the large modified spot, which will include both modified and unmodified lifetime values, and therefore provided a very poor fit to the data.

Secondly the stretched exponential fit, of the form

$$I(t) = A\exp\left(\left(\frac{-t}{\tau}\right)^{1/h}\right) \tag{4.5}$$

This provided a much better fit than the mono-exponential, but there is no intuitive physical interpretation for the h term.

Finally the bi-exponential fit, of the form

$$I(t) = A_0\exp\left(\frac{-t}{\tau_0}\right) + A_m\exp\left(\frac{-t}{\tau_m}\right) \tag{4.6}$$

where τ_m represents some average of all the modified lifetimes within the focal spot. The unmodified term will dominate, but this provides a much more accurate fit of the data than a mono-exponential. Although it is a less accurate fit than the stretched exponential, it allows for a parameterisation of the distribution of modified lifetimes – a single number that can be used to describe the extent of the modification in the presence of the nanoparticle. For this reason it is the bi-exponential fit that will be used for fitting lifetime modified data in this project.

To get an appropriate value for τ_0 a lifetime measurement is taken for each sample in a region where there are no nanoparticles present. This is because despite a high sample quality there is still a small amount of local variation in unmodified lifetime – less than 0.2ns, but enough that care should be taken. Once a value for τ_0 is established and an appropriate bin size defined for the data, equation 4.6 can be fitted to the lifetime decay.

There are a couple of common sense "sanity checks" that should be done to ensure high data quality. Firstly, any non-spherical nanoparticles can be excluded in case they are aggregates. Secondly, nanoparticles are excluded where the signal to noise ratio is very

poor – it is possible that if the nanoparticles are located in a region that has been scanned before that photobleaching will have taken place, and insufficient photon counts have been taken.

4.5.2 Caveats to the Bi-exponential Fitting

Despite the decision that a bi-exponential fit is the most appropriate method for the analysis of lifetime modified data, care must be taken, both in the analysis process, and in the way that this τ_m parameter is used.

Firstly, for the analysis process. It was mentioned earlier in section 5.5.1 that when small bins provided insufficient photon counts it was prudent to simply expand the size of the bin in order to ensure sufficient photon counts to give a well fitted bi-exponential. This is true, however the need for the photon counts to be sufficiently high needs to be dealt with carefully. The diffraction-limited spot, with a size of around 300nm, defines the image of the fluorescence enhancement in the region of the nanoparticle. This means that resolving objects at a length scale smaller than the diffraction limited spot is impossible using conventional fluorescence techniques and, as this is the case, what is being observed at each point is actually a convolution of all the modified and unmodified lifetime information within that diffraction limited spot. Should the bin size become too large, there is a risk that the small modified-fluorescence component seen in equation 4.6 will be overwhelmed by the much larger unmodified-fluorescence component. If this is the case the fitting of the bi-exponential will become highly unreliable. This does not mean that bin size cannot be expanded; simply that care must be taken.

Secondly, for the interpretation of the data. As mentioned in the previous section, modified lifetime values, τ_m, or values for the ratio of modified to unmodified lifetime, τ_m/τ_0, are used to parameterise the distribution of modified lifetimes measured within the sample. This is a single useful number that we can use to describe the lifetime response of the system. It cannot be used to give an exact value for the reduction in fluorescence lifetime observed in the region of the nanoparticle, but it can be used to determine trends observed in the data. However, in order to make comparison between data points, the methodology adopted for analysis must be consistent across the sample set. A set of nanoparticles with τ_m values determined using a bin size of 6 pixels for example cannot be compared to a set of

nanoparticles whose τ_m values were determined using a larger or small bin size – this bin size adjustment would serve to change the relative weighting of the modified and unmodified components, and would make any comparison between the two unfair. However, bearing in mind this restriction this parameter can be used to identify trends and dependencies in the data.

4.6 Summary

This chapter has introduced all the sample configurations that will be used in further experimental sections, and has established that the samples fabricated for those measurements are of a high quality. Additionally, it has introduced all of the fluorescent dyes that will be used in this project, and discussed appropriate fitting methods for determining both the intensity enhancement, and the fluorescence lifetime.

Chapter 5 – Effects of Spacer Thickness on Lifetime and Intensity Modification

This chapter investigates the variation in intensity enhancement and fluorescence lifetime modification when a fluorescent-doped polymer film is separated from a single gold nanoparticle by some spacer layer of varying thickness. Large nanoparticle populations in the region of various fluorescent dyes were interrogated in order to give a statistical distribution of these modifications. Here two different sample configurations are outlined, and the reasoning behind the choice of configuration explained. A number of "proof of principle" measurements are discussed, and then two phases of results for two individual nanoparticle populations are outlined, along with their findings and potential limitations.

5.1 Sample Structure and Expectations

This chapter principally concerns itself with the dye-spacer-nanoparticle sample as outlined in section 4.1.1. All measurements, apart from those taken at the very beginning of the project, were taken using this sample configuration, and so all discussion of the effects from here on in will assume this geometry.

These samples enable a single gold nanoparticle to be located at some fixed distance from an effectively infinite thin film of dye-doped polymer, in order to determine the extent to which the emitted fluorescence is modified by the presence of the nanoparticle depends on its proximity. Consider figure 5.1, where this configuration is depicted with three different sample thicknesses. In figure 5.1c) a sample with no spacer layer is depicted. This means that, considering the information in section 2.3.6, it is expected that the dye in direct contact, or very close proximity to the gold nanoparticle will experience fluorescence quenching. It is anticipated that the dye that is located slightly further away – a few tens of nanometres from the gold nanoparticle, again based on the information from section 2.3.6 – will experience the greatest fluorescence intensity enhancement or lifetime modification, and the extent of this modification will decrease with increasing distance from the nanoparticle. Figure 5.1a) shows a sample with a spacer thickness of 50nm. Here, in contrast to the sample with no spacer layer, there is no dye close enough to the gold

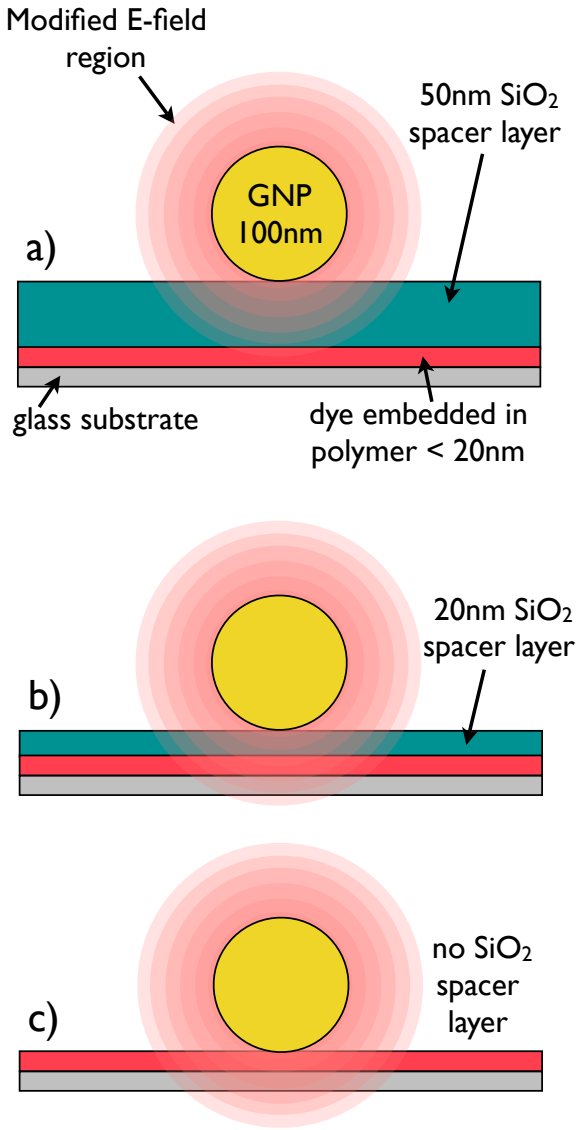

Figure 5.1: A generalised depiction of the problem in this chapter. This figure shows, broadly to scale, the extent to which the modified e-field from a gold nanoparticle with a diameter of 100nm overlaps with the polymer embedded dye region for spacer thicknesses of a) 50nm, b) 20nm and c) no spacer layer.

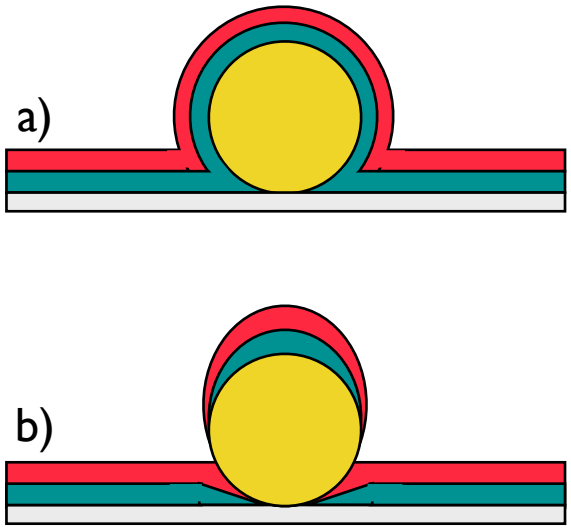

Figure 5.2: The a) best case and b) worse case scenarios for the likely sample configuration for preliminary measurements. The green layer is the silicon dioxide spacer layer, and the red layer is the dye embedded polymer, as seen in figure 5.1.

nanoparticle to undergo quenching. Indeed, there is no dye in the region of optimal intensity enhancement or lifetime modification. It is therefore expected that, the extent to which intensity or lifetime is modified in such a sample would be less. The modification seen in the region of samples such as those seen in figure 5.1b) will lie somewhere in-between figures 5.1a) and 5.1c).

The exact values used for the spacer thicknesses varied. However, it was stated in section 2.2.3 that the distance dependence of the reflection field is such that the value of its decay length is $0.26r$, where r is the radius of the metal nanoparticle. This means that in the case where the diameter of a metal nanoparticle is 100nm – the typical size for all spacer thickness variation measurements – then r is 50nm, and the decay length of the modified electric field will be expected to be around 13nm. A bi-exponential fit is used to determine a value for the modified lifetime τ_m. This method requires care in its use as when the magnitude of the modified component is too small relative to the magnitude of the unmodified component the fitting becomes very unreliable. As such, it is only a useful method when there is a reasonably substantial modified lifetime component. Throughout the experimental process it became clear that once the fluorophore/nanoparticle separation distance increased above 50nm the fitting became increasingly unreliable and the associated

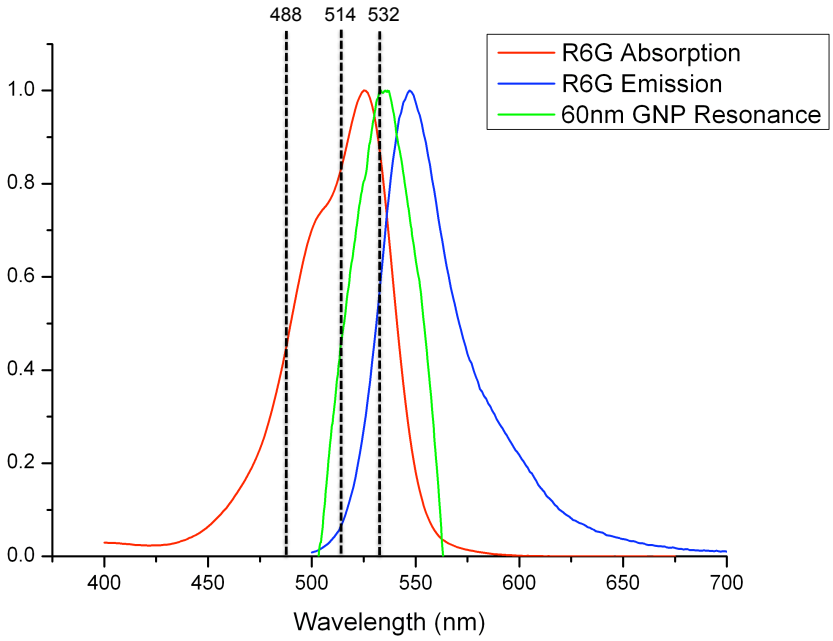

Figure 5.3: The fluorescence spectrum of R6G, with the excitation wavelengths, and the bulk LSPR spectrum for 60nm GNPs.

errors became very large. As such it was decided to restrict measurements investigating the distance dependence of the enhancement to between 0 and 50nm separation.

Thus, as the thickness of the spacer layer is varied, it is expected that the proportion of the dye subject to quenching due to the proximity to the metal, and the proportion of the dye subject to optimal fluorescence enhancement will similarly vary. Consequently a variation in intensity enhancement will be seen as this spacer sample thickness is altered, and similarly when the data analysed using a biexponential, as outlined in section 4.5, a variation will be seen in the value of average modified lifetime, or τ_m.

5.2 Initial Measurements and Proof of Principle

Initial measurements were taken using R6G doped PVA layers and 60nm gold nanoparticles. These samples were of a slightly different configuration to those used later in the experiment – rather than a dye-spacer-nanoparticle sample, these were nanoparticle-spacer-dye samples, of a configuration as seen in figure 5.2. The dye layer was R6G in PVA,

either 50µM, 100µM or 250µM R6G and 0.25% PVA, the spacer layer was silicon monoxide (SiO) and was thermally evaporated in the same manner as the dye-spacer-nanoparticle samples, and the gold nanoparticle size was 60nm. The overlap of the emission/excitation spectrum of R6G and the bulk resonance of the 60nm gold nanoparticles can be seen in figure 5.3. The fluorescence filters used for detection were a Nikon FITC dichroic mirror at 505nm and a Comar long-pass 538nm filter.

This sample configuration was initially used because of sample wetting problems, to allow dark field measurement, and because of concerns that nanoparticle aggregates might be formed – further experimentation as outlined in chapter 5 proved that these worries were unfounded. The problem with this sample configuration however is much like the problem with the nanoparticle-dye sample outlined in section 4.1.2 – it is very difficult to be absolutely sure of what you are looking at. In figure 5.2a) the "best case" scenario for sample configuration is shown, and in figure 5.2b) the "worst case" scenario. The likelihood is that the actual configuration was some compromise between the two – it would be very difficult to get a uniform spacer layer deposited onto a nanoparticle using thermal evaporation, given that the material to be deposited on the surface is not approaching the sample from all angles. It therefore seems probable that the thickness of the spacer layer on the nanoparticle will be greater on the top than it will be on the sides, but it is not possible to tell the extent to which the sides of the nanoparticle are bare. Similarly, it is unlikely that the dye embedded polymer layer deposited onto the nanoparticle uniformly covers the spacer layer. However, later samples used the newer configuration after it was made clear that there were no nanoparticle aggregates formed on top of the spacer layer even with the difficulties in wetting the sample (see section 4.2.1). This was preferable as it was not only much easier to be sure of its configuration, but it was also a much simpler system to model computationally – an extension to the investigation that the group remains interested in pursuing.

From the initial measurements using the nanoparticle-spacer-dye samples three things became apparent – a distribution of modified lifetimes is observed, these modified lifetimes are not affected by the excitation wavelength, and they are also density independent up to a point. These characteristics will be further discussed in the following sub-sections.

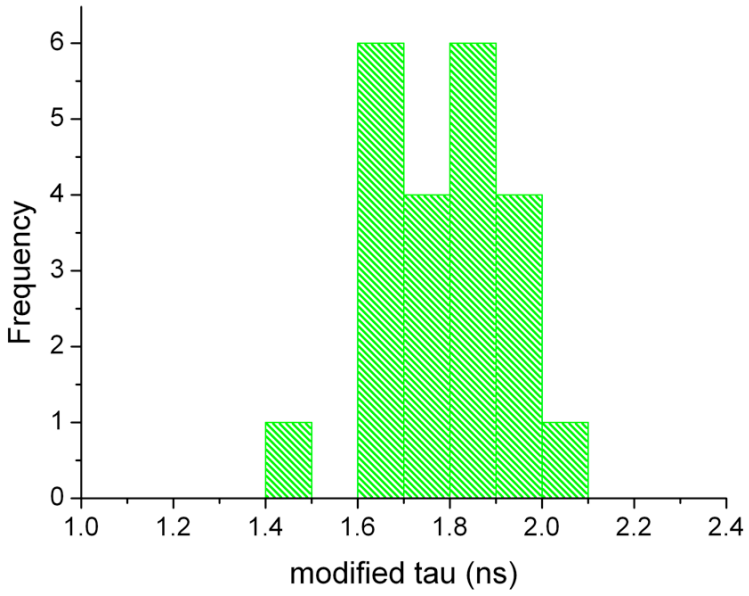

Figure 5.4: A sample distribution measured modified lifetime values for a nanoparticle-spacer-dye sample of R6G embedded in PVA.

5.2.1 A distribution of modified lifetimes is observed

A distribution of values for the modified lifetime is observed for the sample, as can be seen in figure 5.4. It is thought that this lifetime distribution is due to a slight variation both in the size and the shape of the nanoparticle – the manufacturers, BBInternational, give a size variation value of 60±5nm. This is assumed to cause a variation in the LSPR and thus a variation in the overlap between the LSPR and the emission spectra of the dye, which in turn is expected to alter the extent to which the lifetime and the intensity is modified. Whether or not this holds true will be discussed in more detail when considering the relationship between the LSPR of individual nanoparticles, and the modification in their vicinity, but for the moment the distribution is attributed to this non-uniform nanoparticle characteristic.

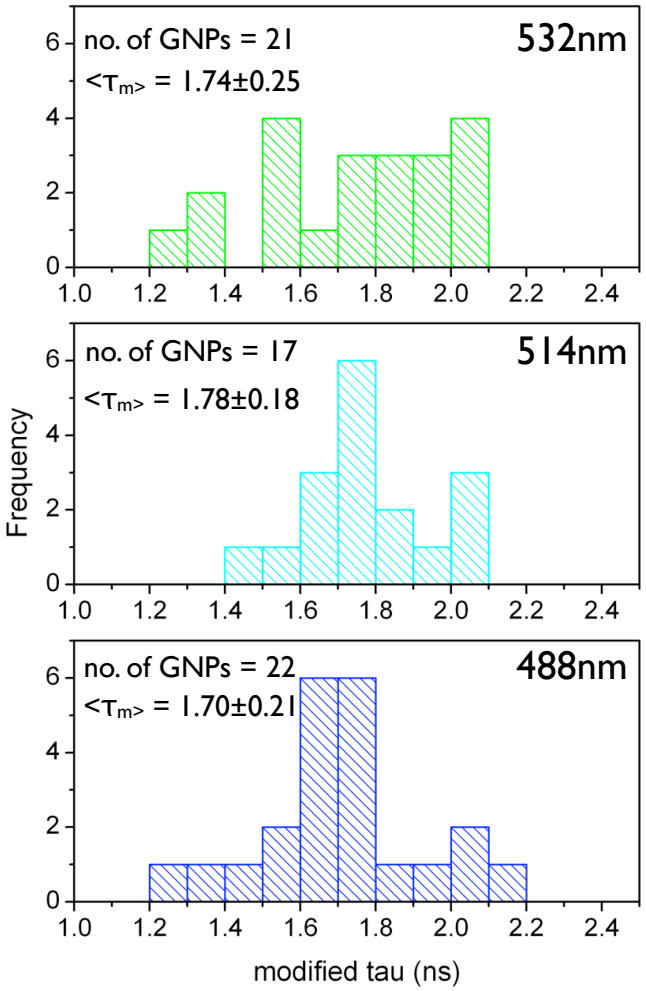

Figure 5.5: The wavelength dependence of the distribution of modified lifetime values.

5.2.2 The modified lifetime distribution is excitation wavelength independent

As a proof of principle the sample was excited at three different wavelengths, and the lifetime distribution measured. It is anticipated that altering the excitation wavelength should have no effect on the modified lifetime value, as all that is being changed is the efficiency with which the dye is being pumped which, unless the fluorophores were near to saturation, might be responsible for a modification in fluorescence intensity but should have no lifetime influence. This independence is illustrated in figure 5.5 – variation in the shape of the modified lifetime distribution can be seen, but the average value for modified lifetime is similar across different excitation wavelengths, and the variation in the shape of the distribution is likely to be due to the number of nanoparticles being statistically insufficient.

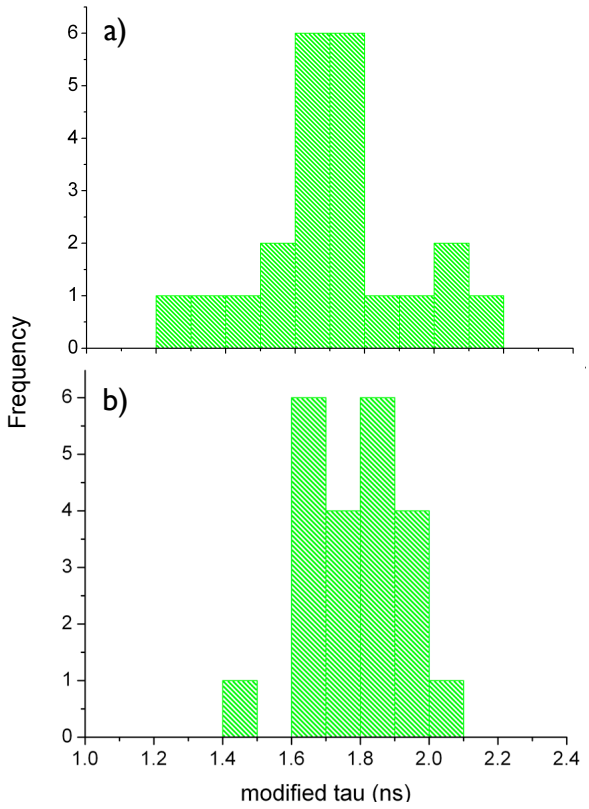

Figure 5.6: The dye concentration of the distribution of modified lifetime values – a) 50µM concentration, and b) 250µM concentration.

As a result subsequent measurements were all taken where the dye was excited at the excitation maximum, as far as this was possible due to filter/dichroic constraints.

5.2.3 Modified lifetime values are density independent

Two very different densities were measured to determine the effect that the concentration of the dye in the dye-polymer layer had on the distribution of modified lifetime – one low concentration sample with a R6G concentration of 50µM, and one high concentration sample with a dye concentration of 250µM. The resulting modified fluorescence lifetime distributions can be seen in figure 5.6. It was expected that a difference in density would not affect the average value of modified lifetime, and indeed it does not, with the average modified lifetime values for the 50µM and 250µM samples measured to be 1.66±0.21ns and 1.75±0.15ns respectively. A slight difference is observed in the widths of the distributions, but again the number of nanoparticles sampled here is not large enough for it to be

conclusively determined that this is statistically significant. It is possible that in the much less concentrated sample that the fluorophores are sufficiently disperse in the polymer layer that the arrangement of fluorophores cannot be considered to be consistent when comparing nanoparticles – that is for some nanoparticles there will be lots of fluorophores in close proximity to the nanoparticle, and for other nanoparticles this number will be fewer, thus causing a slightly broader distribution. However, this seems unlikely given the high fluorescence photon counts detected for these samples.

5.3 Phase One Measurements

Using a sample of the configuration seen in figure 4.1 a series of measurements were then made, this time varying the thickness of the spacer layer between the dye-embedded polymer and the nanoparticle. This configuration used 100nm gold nanoparticles in the vicinity of a PM597 doped PMMA and separated by a silicon dioxide spacer layer of varying thickness – a configuration believed to be optimal, as there is a high degree of overlap between the emission spectrum of PM597 and the LSPR of a 100nm gold nanoparticle. The samples were excited by light at a wavelength of 532nm, and detection took place using a Nikon dichroic wavelength 565nm, and a Comar long-pass 538nm filter – a configuration that ensured that laser bleed-through was not an issue.

In theory, five thicknesses of spacer layer were examined – no spacer, and 5, 15, 20 and 30 nm spacer thicknesses. However, there are problems with this assertion as the deposition of the silicon dioxide layer was not without issues. As mentioned previously silicon dioxide is preferable to silicon monoxide due to its favourable refractive index properties, but the difficulty, not of deposition, but of measuring the thickness of the spacer deposition here means that it is very difficult to state the thicknesses of these samples with any degree of certainty. The thickness of the spacer layer being deposited was measured using a quartz crystal oscillator as part of a film thickness monitor, but these oscillating crystals have a tendency to overheat when exposed to high temperatures for long periods of time, and, at the time that these measurements were taken, the department did not have access to a cooled quartz crystal oscillator. Due to silicon dioxide's high evaporation temperature and therefore the relative difficulty of deposition, the film thickness monitor would typically overheat at between 5 and 10nm deposition, meaning that the monitor would simply stop detecting additional deposition on the crystal. This meant that when depositing a thick

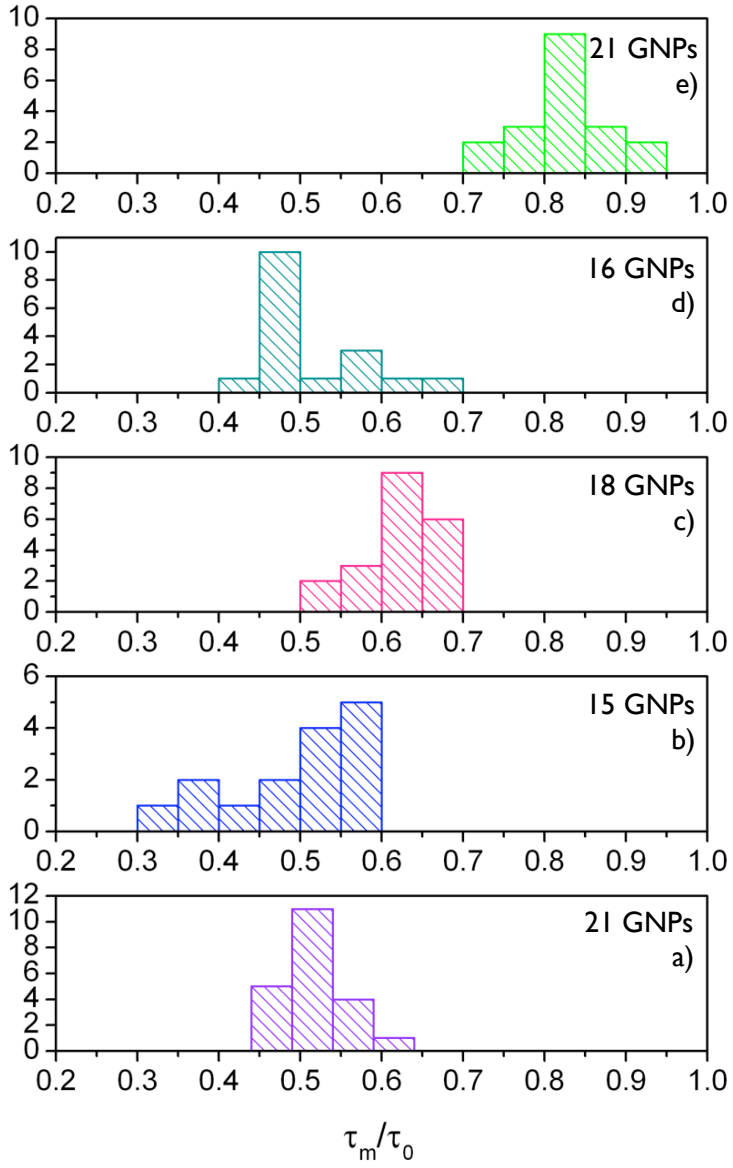

Figure 5.7: Variation of ratio of modified to unmodified fluorescence lifetime with spacer layer thickness for the first set of 100nm gold nanoparticles in the region of PM597 doped PMMA, deposited on nominal spacer thicknesses a) 0nm, b) 5nm, c) 15nm, d) 20nm and e) 30nm.

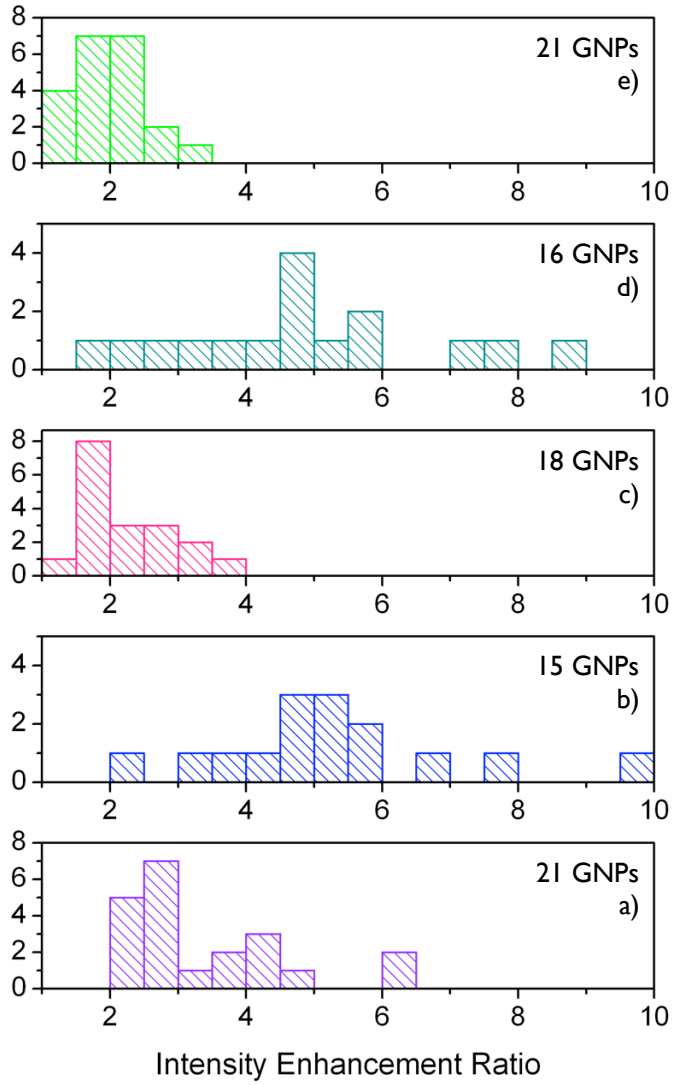

Figure 5.8: The variation in intensity enhancement ratio with spacer layer thickness for the first data set of 100nm gold nanoparticles in the region of PM597 doped PMMA, deposited on nominal spacer thicknesses a) 0nm, b) 5nm, c) 15nm, d) 20nm and e) 30nm.

sample care had to be taken to identify when the monitor had overheated, stop deposition, wait until the system had cooled sufficiently that the film thickness monitor was working again, and then recommence deposition. Checks were made to ensure that no compromise was made concerning the smoothness of the surface, but, despite best efforts, it was very difficult to ensure that accurate measurement of the surface thickness was similarly uncompromised.

In figures 5.7 and 5.8 the data from five samples with different spacer thicknesses is shown. These histograms show both the average modified lifetime to unmodified lifetime ratio τ_m/τ_0, (figure 5.7), and intensity enhancement ratio η, (figure 5.8), for sample of different spacer thickness, labelled a) to e). In theory, these letters correspond to spacer thicknesses of a) 0nm, b) 5nm, c) 15nm, d) 20nm and e) 30nm, however given the limitations outlined above these thicknesses must be considered only to be rough guidelines, especially samples c) d) and e) where the spacer thickness is greater – with the obvious exception of the sample without a spacer layer.

5.3.1 Spacer Thickness and Lifetime Modification

With the caveat outlined above in mind, firstly consider the relationship of τ_m/τ_0 to spacer layer thickness as depicted in figure 5.7. As mentioned previously, fluorescence lifetime modification occurs due to the near-field electromagnetic distribution associated with the nanoparticle LSPR introducing additional radiative decay pathways in the fluorophore, and the greater the strength of the local field, the greater the reduction in fluorescence lifetime. Here not much variation is seen between samples a), b) and d), with the average values for the ratios of τ_m/τ_0 seen to be 0.52±0.01, 0.49±0.02 and 0.51±0.02 respectively. However, clear differences are observed when considering both sample c) and sample e) with τ_m/τ_0 values of 0.62±0.01 and 0.83±0.06 respectively, values much greater than the value observed for any of the other samples, and seemingly demonstrating an increasing value of τ_m/τ_0 with distance from the sample. However, if this is the case, sample d) would seem to be an anomaly – although apparently nanoparticles are at a greater distance from the dye doped polymer the modification in lifetime seems to be greater than that seen in sample c). There does not seem to be a sensible physical reason for such an observation that would explain the variation in lifetime. Given that these two samples are only estimated to have a spacer sample thickness difference of 5nm, it seems likely that the error in the

measurement of the thickness is sufficiently high that it cannot be stated with any high degree of confidence which of these is thicker. However, regardless of these limitations, it can clearly be seen from this data that τ_m/τ_0 does show a substantial variation as the distance between the PM597 doped PMMA and the gold nanoparticle increases. This variation is expected, as the greatest reduction in lifetime occurs where the greatest enhancement in electric field is observed.

5.3.2 Spacer Thickness and Intensity Modification

Secondly, the apparent relationship between intensity enhancement ratio, η, and spacer layer thickness is considered, as seen in figure 5.8. Here a greater variation is seen between the different samples, but also each histogram a broader distribution than the distributions seen in the lifetime modification samples. Initially, a clear fluorescence intensity enhancement in the region of the nanoparticle can be seen for all the different spacer samples. It is worth taking a moment at this point to address the two causes of this fluorescence intensity enhancement.

Firstly, the presence of the nanoparticle can cause the fluorophore to be pumped harder – this happens because the presence of the electric field induced in the nanoparticle in turn introduces additional excitation pathways in the fluorophore. The extent to which this pumping occurs is proportional to the intensity of the electric field modification. The extent to which the nanoparticle is excited on resonance will determine how effectively the incident radiation is coupled into the polarisation induced in the nanoparticle, which will in turn influence the extent to which the surrounding fluorophores will be pumped. And, since optimal pumping occurs where the electric field is optimally enhanced, this enhancement exhibits a strong distance dependence. It is possible to make a rough estimate of the extent of this enhancement using equation 2.2.1. Ignoring the effects that the relative orientation of $\hat{r}$ and $\mathbf{E_0}(\omega)$ have on the magnitude of the reflection field, it can be seen that the maximum enhancement observed is therefore of the form

$$\frac{\varepsilon_m - \varepsilon}{\varepsilon_m + 2\varepsilon}\left(\frac{a^3}{r^3}\right) + 1. \tag{5.1}$$

At the surface of the metal the extent of the enhancement will be optimised, as a is equal to r, and r is at a minimum, and so the extent of the enhancement depends only on the values of ε_m and ε. The optical constants, n and k, for gold at the typical excitation wavelength used in this project can be found in the work of Johnson and Christy (67), and thus ε_m can be calculated using the relationship $\varepsilon = \varepsilon' + i\varepsilon''$, where $\varepsilon' = n^2 - k^2$ and $\varepsilon'' = 2nk$. Thus the maximum magnitude of the enhancement due to increased pumping of the fluorophore can be calculated to be approximately 3.9.

Alternatively, if the quantum yield is less than unity then the quantum yield can be increased in the region of the nanoparticle, thus increasing local fluorescence intensity. A low quantum yield occurs because there is a non-radiative decay pathway available to the excited state fluorophore that is similarly favourable to the radiative decay pathway. Indeed, in very small quantum yield fluorophores this non-radiative decay pathway is often preferred. As such, it makes sense that if the quantum yield of a fluorophore can be increased the intensity will similarly increase. The presence of a nanoparticle can modify the local photonic density of states such that additional radiative decay pathways are introduced in the fluorophore, thus improving the quantum yield of the dye. PM597 has a quantum yield of around 0.4, and so in the situation where quantum yield could be increased to unity, an enhancement factor of 2.5 is expected. It is clear from the histogram data in figure 5.8 that the dye in the region of many of the nanoparticles exhibited a fluorescence enhancement far greater than this. It is therefore logical to conclude that the intensity enhancement observed here results from a combination of the two enhancement methods addressed above.

These rough calculations would suggest that the magnitude of the fluorescence intensity enhancement observed in the nanoparticle would not exceed around 6.4. However, despite most particles exhibiting an enhancement consistent with these expectations, a greater intensity enhancement than this can be seen in a few particles in figure 5.8.

However, unlike the lifetime modification case samples a), c) and e) exhibit smaller average values for intensity enhancement ration, η, of 3.5±0.2, 2.3±0.2 and 2.0±0.2 respectively, than either samples b) or d), with average values of 5.3±0.3 and 4.9±0.9 respectively, exhibit. The reasoning for these smaller values however is not the same in every case. The small value of η for sample a), where there is no spacer layer, is likely due to fluorescence

quenching from close proximity to the metal, as described in the section 2.3.2, where extra non-radiative pathways are introduced when the fluorophore is in very close proximity to the metal. As such, when the nanoparticle moves further away from the dye the quenching effect is less noticeable, particularly when balanced against the enhancement from the strong local field. Therefore, it might be expected that in very close proximity quenching would be observed, reducing the intensity enhancement, then as the distance between the nanoparticle and the fluorophores increased an increase in η would be observed until it reached a maximum value of enhancement. Then, as distance between the nanoparticle and the fluorophores continued to increase, the enhancement would decrease again. The trend exhibited in this sample seems to correlate well with what would be expected from the theory, again with sample d) appearing to be anomalous, most likely for the reasons presented in the previous section.

5.3.3 Lifetime Modification and Intensity Enhancement

A plot can also be made of the intensity enhancement ratio, η against τ_m/τ_0. Figure 5.9b) shows a plot of all the single nanoparticle data collected in the phase one measurements. While the individual data populations can be difficult to discern, there is definitely a trend. It can be seen even more clearly in figure 5.9a) where the average values for each population are plotted. Broadly, it can be seen that as is τ_m/τ_0 decreases, intensity, η, is enhanced. This means that even if the nominal thickness values need to be treated with extreme caution, the data can still be interpreted as being a dependence between two physical quantities which in turn have some dependence on the underlying physical geometry.

5.3.4 Problems to be addressed

There are two problems with the data in this section. Firstly, not enough nanoparticles are measured to determine whether or not the shape of the distribution can be considered relevant. This is easily fixed by taking much larger nanoparticle population samples, and this is done in the following section. A second, and more important consideration is that of the uncertainty in the spacer thickness. This concern was addressed when the department bought a water-cooled film thickness monitor, and thus film thicknesses could be determined to a much higher degree of accuracy.

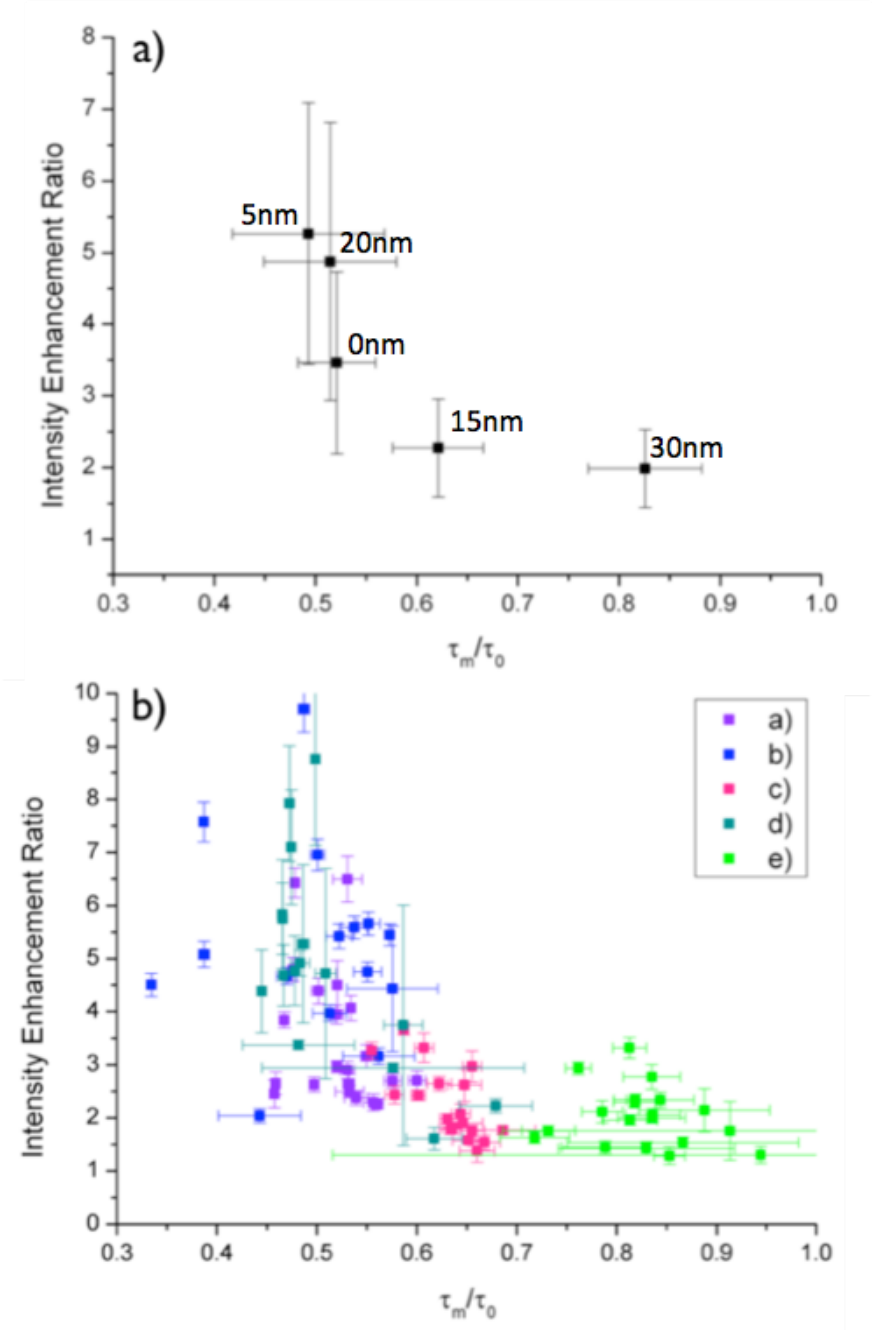

Figure 5.9: Two plots depicting the relationship between Intensity enhancement ratio and the average modified lifetime to unmodified lifetime ratio for the first data set of 100nm gold nanoparticles in the region of PM597 doped PMMA. a) Shows the entire population of particles plotted on one graph, and b) shows the average values.

5.4 Phase Two Measurements

In order to address the problems with a lack of statistical certainty in the previous section, a new set of data was measured. The same sample configuration was used, the same dye (PM597) and the same nanoparticle size (100nm). They were excited in a similar manner, and measurements were made using the same dichroic and filters. However, unlike the previous section, the spacer thicknesses are well defined, and the nanoparticle population sizes are much larger, with no less than 50 nanoparticles sampled for any sample (although some of those that did not meet the inclusion criteria outlined in section 4.5.1 might then have been excluded, which explains why not every histograms contain 50 nanoparticles.)

As before data collected from five samples with different spacer thicknesses is shown, both for the intensity enhancement ratio η, and for the average modified lifetime to unmodified lifetime ratio τ_m/τ_0.

5.4.1 Spacer Thickness and Intensity Modification

Histograms for showing η for nanoparticle populations of five different samples with spacer thickness values of 0nm, 10nm, 20nm, 30nm and 50nm are shown in figure 5.10. The data here matches well with the expected behaviour outlined in section 6.3.2 – quenching causes a much smaller η value when there is no spacer, and then an increase in η is observed until the enhancement is optimal and a gradual reduction in fluorescence intensity enhancement can be seen as spacer thickness increases.

The mechanism for intensity enhancement is no different from the mechanism described in the phase one measurements, but here a few enhancement outliers can be seen where a very significant fluorescence intensity enhancement is seen. This presumably happens because the LSPR has been blue-shifted so that it lies closer to the excitation spectrum, thus causing an enhanced excitation pumping rate, but this will be discussed in more detail in the following section.

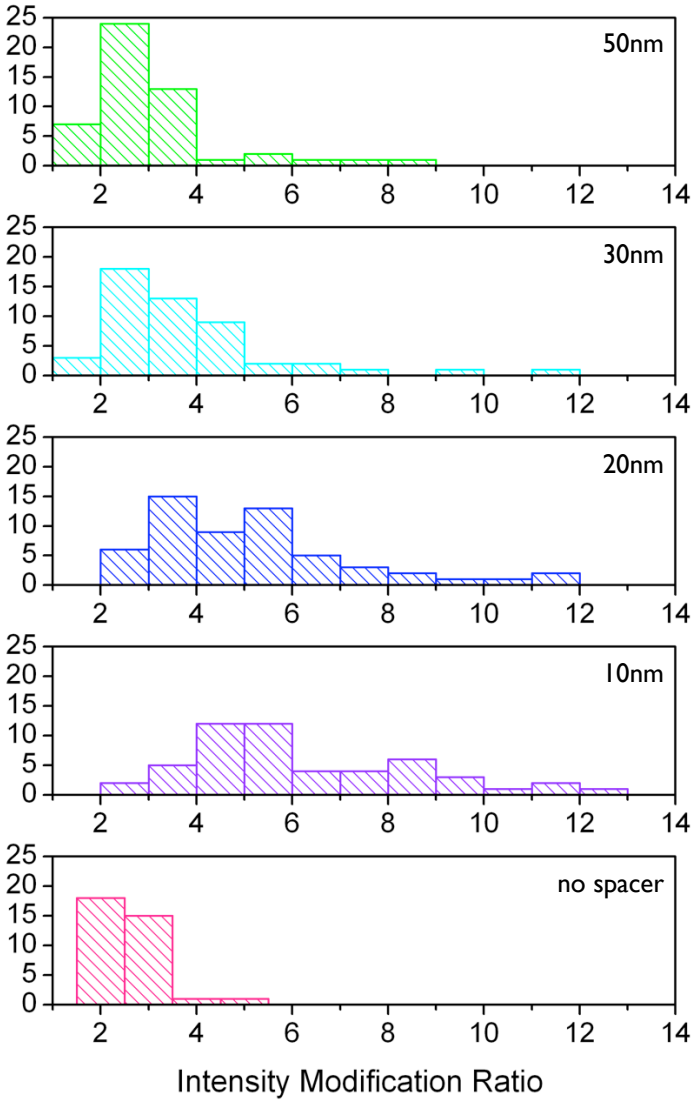

Figure 5.10: The variation in intensity enhancement ratio with spacer layer thickness for the second data set of 100nm gold nanoparticles in the region of PM597 doped PMMA.

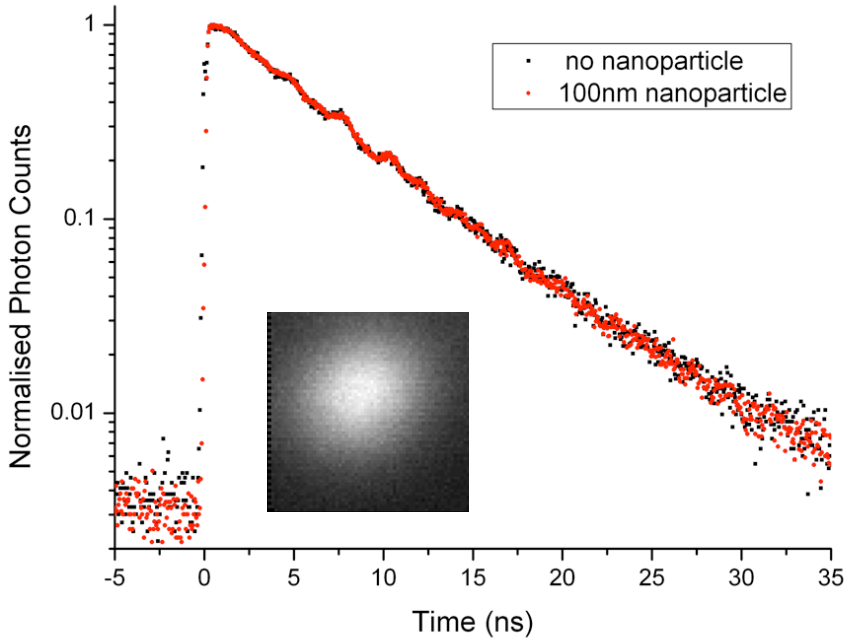

Figure 5.11: Lifetime modification for fluorescent molecules in the presence of a nanoparticle with a 20nm spacer layer. Note that there is no difference observed between a typical unmodified lifetime, and the fluorescence lifetime in the region of a nanoparticle, despite the clear fluorescence intensity enhancement seen in the image in the inset.

5.4.2 Spacer Thickness and Lifetime Modification

The relationship between τ_m/τ_0 and spacer thickness can now be examined, and it is at this point that problems in the data analysis became obvious. Data was collected for five samples, but for two of the samples, the 10nm and 20nm samples, there were problems in measuring the extent of the lifetime modification. A strong intensity enhancement was observed for these nanoparticles, but very little fluorescence lifetime modification.

Part of this problem was due to slightly lower photon counts than the previous data sets. It was thus decided that instead of taking a small bin size as discussed in previously, that all pixels within the image 64x64 pixel 1µm image would be binned, and the data re-analysed. This would ensure that sufficient photons would be considered to allow a high quality of fitting. However such an approach requires caution, as the increase of the bin size means that the relative magnitude of the unmodified lifetime component increases in comparison to the modified lifetime component. For the case of small lifetime modifications, this might

become restrictive, as reducing an already small modified-lifetime component further could dramatically increase the error. With care taken to ensure that this was not a problem, the data for all sample thicknesses was then re-analysed. This approach worked very well for the 0nm, 30nm and 50nm spacer samples, however despite these efforts the 10nm and 20nm samples showed almost no lifetime modification (as seen in the example nanoparticle shown in figure 5.11) despite showing a much larger fluorescence intensity modification than their thicker spacer layer counterparts. Much care had been taken to ensure that the intensity enhancements observed concurred with the location of nanoparticles using dark field, and all fluorescence enhancements did indeed take place in the vicinity of a nanoparticle. As such, at the time of writing, conclusions have been reached as to why such a strong enhancement would be observed, and yet no corresponding reduction in lifetime.

Having decided that no useful analysis could be done on the lifetime data for the 10nm and 20nm samples because of the difficulty in the analysis of the lifetime, attention then turned to the 0nm, 30nm and 50nm samples. Again, in order to ensure high photon counts, rather than just binning the central pixels of the nanoparticle, all pixels in the image were included. The histograms yielded for the variation of τ_m/τ_0 with varying thickness are shown in figure 5.12. However, these large nanoparticle number populations yielded results that show a disagreement, both with the results seen in the previous section, and with the results that would be expected from the theory expounded in chapter 2. Instead of seeing fluorescence lifetime modification ratio increase with increasing spacer sample thickness, here the fluorescence lifetime modification ratio seemed to decrease with increasing distance.

This means that the data in figure 5.13 does not show the same trend as was observed in figure 5.9. However, despite this, some nanoparticles with very high intensity enhancement ratio values can be seen, and they're not necessarily those with the largest τ_m/τ_0 values. This would seem to support the assertion that the large modification in intensity can come from excitation enhancement, possibly due to a blue-shifted LSPR.

In the light of these seemingly counter-intuitive results, it seemed prudent to then make sure that nothing in the analysis process was adversely affecting the results. The error values, both of the fit (that is the χ^2 value), and of the fitted parameters (that is the error in τ_m itself) were checked to see that they fell within sensible limits, which they did. Furthermore, in order to make sure that the data analysis was not being skewed by

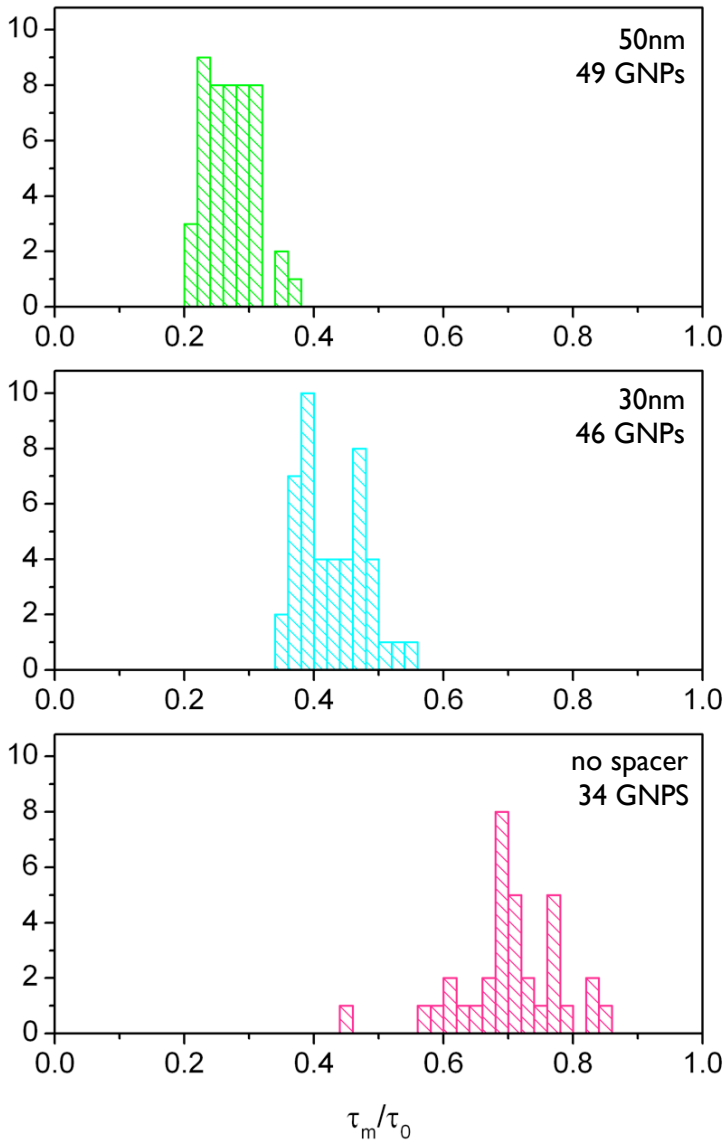

Figure 5.12: Variation of ratio of modified to unmodified fluorescence lifetime with spacer layer thickness for the second set of 100nm gold nanoparticles in the region of PM597 doped PMMA.

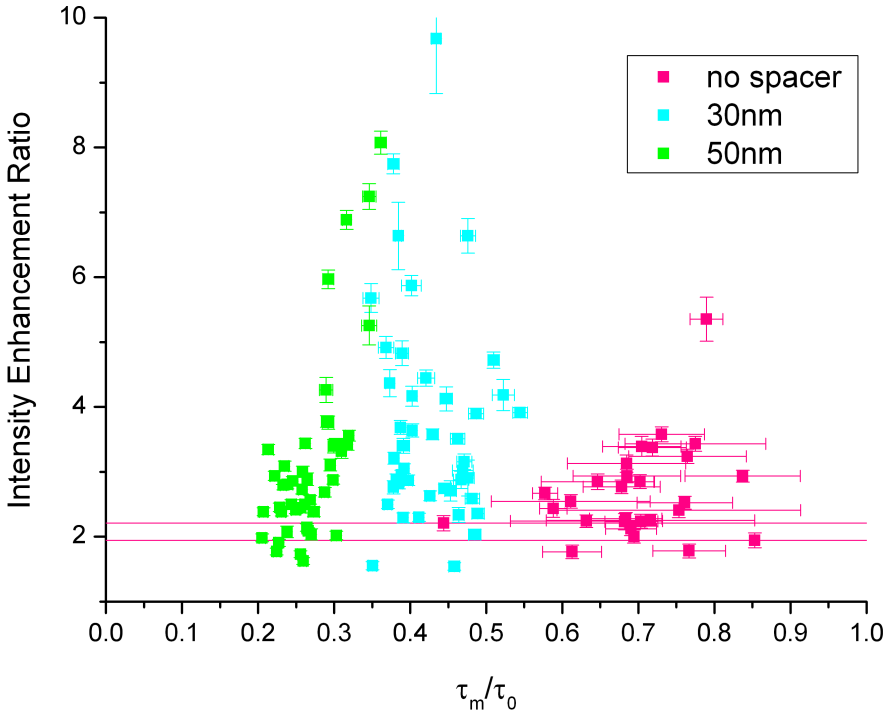

Figure 5.13: A graph depicting the relationship between Intensity enhancement ratio and the average modified lifetime to unmodified lifetime ratio for the last set of data 100nm gold nanoparticles in the region of PM597 doped PMMA.

manipulation of the unmodified lifetime, the data for the 30nm and 50nm spacer samples was then analysed with an unfixed τ_0 value. Conventionally, as explained in section 4.5, the analysis process involved taking a reference fluorescence lifetime measurement from a region with no nanoparticles, and using that lifetime as the τ_0 value. But, given that it is known that altering the τ_0 value can cause a large shift in the value of τ_m, would a significant difference in the value of τ_m be seen if, instead, the TRI2 software was allowed to fit both τ_0 and τ_m? Figure 5.14 shows a comparison between the τ_m/τ_0 values when τ_0 is fixed and those when τ_0 is unfixed. While a difference in distribution size, and a small difference in the mean values of the distributions are observed, these differences are not sufficient to explain why instead of the extent of the lifetime modification decreasing as spacer thickness increases the extent of the lifetime modification only increases.

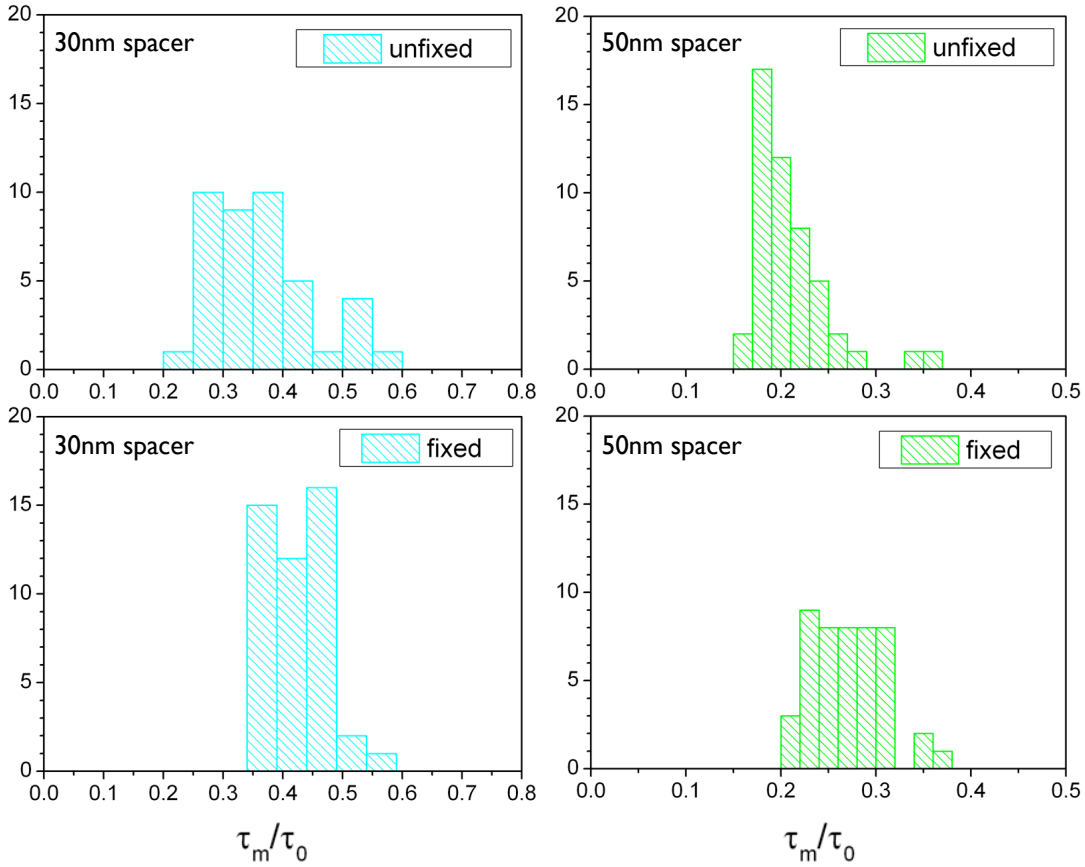

Figure 5.14: A comparison of τ_m/τ_0 values when the value of τ_0 is unfixed, and when it is fixed. While some variation is observed, it is insufficient to cause the strange trends observed when comparing data for different spacer sample thicknesses.

Given that both the fitting was good, and the analysis did not seem to be critically affected by the choice of a τ_0 value, there does not seem to be a clear explanation as to why this unexpected modification in fluorescence lifetime trend is observed, without further detailed theoretical analysis. It is however possible that the discrepancy is as a result of the nature of the fitting process for this simplistic parameterisation.

5.4.3 Spacer Thickness and Weighted Lifetime Modification

Given the counterintuitive trend observed in figures 5.12 and 5.13 for the variation of modified lifetime with spacer distance, particularly in the light of the seemingly physically sensible trend in intensity enhancement modification with distance, it was suggested that a

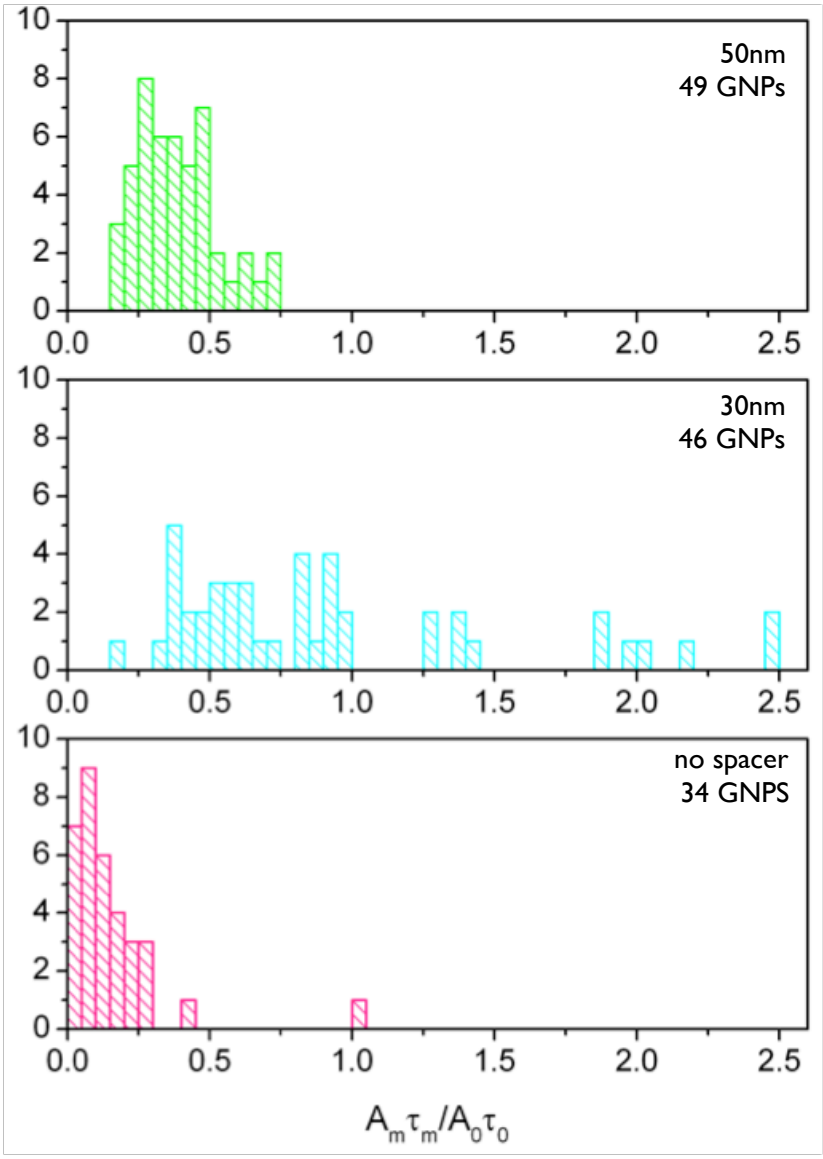

Figure 5.15: Variation of ratio of weighted modified to unmodified fluorescence lifetime with spacer layer thickness for the second set of 100nm gold nanoparticles in the region of PM597 doped PMMA.

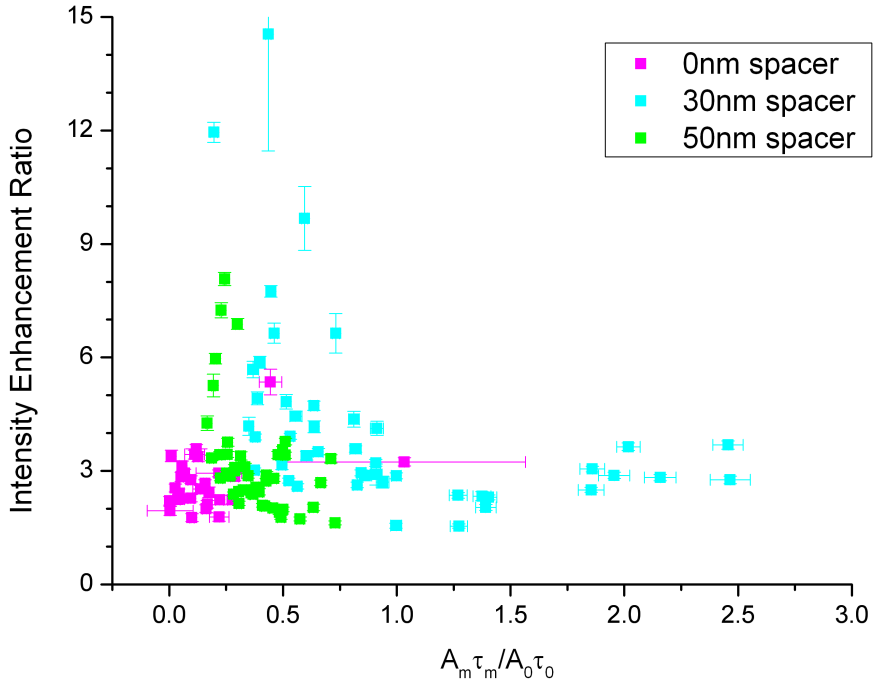

Figure 5.16: A graph depicting the relationship between Intensity enhancement ratio and the average weighted modified lifetime to unmodified lifetime ratio for the last set of data 100nm gold nanoparticles in the region of PM597 doped PMMA.

weighted lifetime fitting might explain this anomalous trend. Simply measuring τ_m / τ_0 does not take into account the relative magnitudes of the modified and the unmodified lifetime component. As such it was prudent to instead measure a weighted lifetime modification value of the form $A_m \tau_m / A_0 \tau_0$, where A_0 and A_m are the exponential pre-factors as seen in equation 4.6. As can be seen in figure 5.15, this additional weighting does seem to have some positive affect on the trend. Here the $A_m \tau_m / A_0 \tau_0$ values at a spacer thickness of 0nm are the smallest, most likely due to fluorescence quenching at the surface of the nanoparticle causing a much smaller modified component relative to the unmodified component. There is then a substantial increase in the $A_m \tau_m / A_0 \tau_0$ values for the 30nm spacer thickness sample, and then a reduction in the values again for the 50nm spacer thickness. This trend would seem to agree with the theory in a way that the trend in figure 5.12 failed to, and thus this weighted lifetime modification would be a more appropriate analysis method should this work be further developed.

5.5 Summary

This chapter utilised the enhancement from single gold nanoparticles separated from a fluorescent-doped polymer film by some spacer layer to demonstrate a strong distance dependence for both the ratio of modified to unmodified lifetime, τ_m/τ_0, and the intensity enhancement ratio, η. The bulk of the measurements were taken in two phases. The first phase had significant problems with the determination of the thickness of the spacer layer, but did indeed demonstrate a varying degree of enhancement for both τ_m/τ_0 and η in samples where the spacer layer thickness was known to be different. In addition a relationship between η and τ_m/τ_0 was investigated, showing that the maximum reduction in τ_m/τ_0 occurred at a point of increased η value. The second phase contained a more statistically favourable number of nanoparticle measurements, but problems occurred with the measurement of fluorescence lifetime modification for some of the samples. As such, the conclusions that can be drawn from these samples, despite their well-defined spacer layers, are limited in scope, particularly about lifetime trends. However, these samples exhibited a strong variation in intensity, with a low value where there was no spacer layer, or at long distances from the sample, but showing an increase at length scales inbetween the two. This ties in nicely with the theoretical assumptions in section 2.3.6, where fluorescence quenching is seen at very short distances, then a local enhancement maximum at slightly longer distances, and then as the distance increases the enhancement decreases.

Chapter 6 – The Effects of LSPR on Fluorescence Lifetime

6.1 Sample Structure and Initial Measurements

This chapter concerns itself with the nanoparticle-dye sample. This sample configuration is preferred since, despite the uncertainty about the specifics of the configuration as outlined in section 4.1.2, it is deemed to be more suitable for dark field microscopy than that of the dye-spacer-nanoparticle samples. All measurements were taken using an excitation wavelength of 532nm, and the filters used for detection were either a Nikon dichroic 505 (FITC), or 565 (TRITC) and a Comar long-pass 538nm filter.

Similar to the data in chapter 5, a distribution in the lifetime values is observed for a nanoparticle population. It was proposed in section 5.2.1 that this variation was due to variation in the LSPR spectra of nanoparticles, and this assertion is supported by the data seen in figure 6.1. Here the LSPR spectra and lifetime decays for three nanoparticles are shown. The three nanoparticles selected represent the maximum and minimum LSPR values observed, as well as a more typical LSPR value. In figure 6.1a) the extent to which the normalised LSPR and the emission spectrum of the dye in question, in this case Nile Red, is shown. The structure in the LSPR spectra is due to the fact that the laser source used for the scattering measurements is a spectrally structured source, as was discussed in section 3.5 and can be seen in figure 3.10. Efforts were made to compensate adequately for the spectrum of this source, but this proved complicated due to the fact that the extent to which light is scattered depends on the wavelength of the light. This meant that the structured profile of the laser spectra could not be used directly to correct for the structuring observed in the LSPRs of the nanoparticles. Initially the LSPR spectrum was compared to the scattering spectrum of light from roughened glass, but high noise levels made it a difficult task to distinguish between structure and noise at low signal levels. However, regardless of this structuring it can seen that the overlap extent between the LSPR and the fluorescence emission varies depending on the LSPR profile of the nanoparticle being interrogated. The question is then, does the spectral location of the LSPR relative to the emission spectrum of the Nile Red seem to affect the fluorescence lifetime modification? Figure 6.1b) shows the decay curves of the nanoparticles shown in figure 6.1a), in comparison to the decay curve of

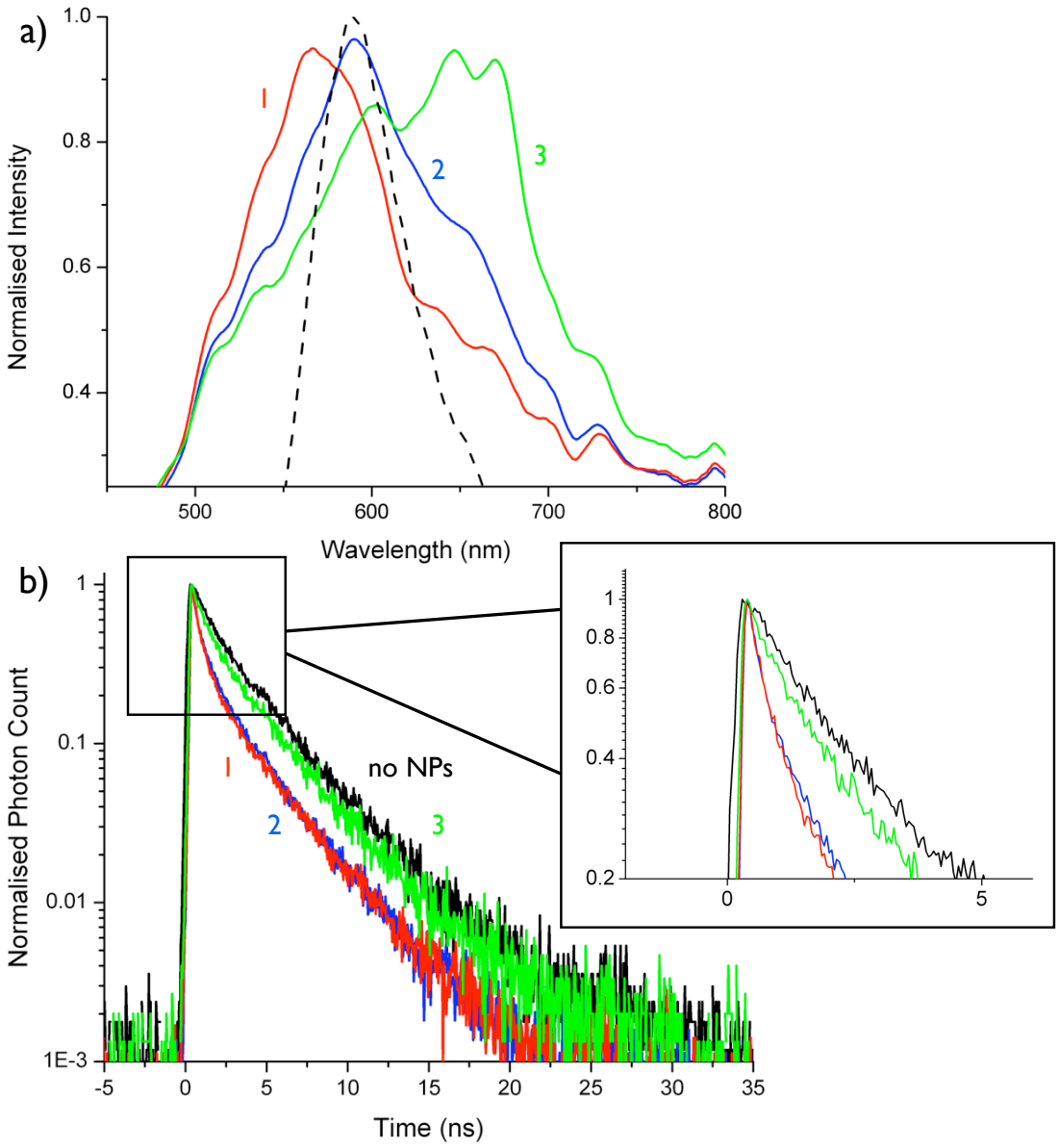

Figure 6.1: a) The dark field scattering of three 100nm gold nanoparticles, giving a LSPR spectrum for each. The extent to which the spectra overlap with the emission spectra of Nile Red, shown by the black dashed line, can clearly be seen. b) The corresponding lifetime decays for Nile Red deposited over each of the imaged nanoparticles, numbered to allow comparison, and a zoomed in section showing the difference in the decays more clearly for short time delays, when rapid decay from fluorophores in the vicinity of the GNPs dominates. A broadband continuum laser source is used for excitation of the scattered spectra and therefore the structure observed in the dark field results from the structure in this source spectrum.

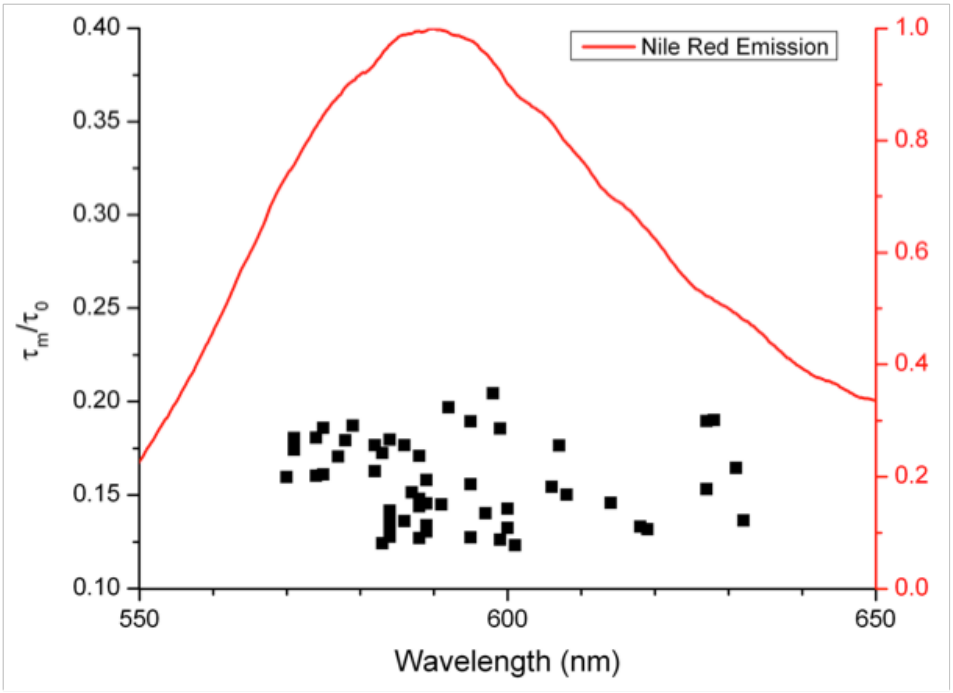

Figure 6.2: The initial data collected for 100nm gold nanoparticles on Nile Red embedded in PMMA, showing the correlation between LSPR peak wavelength, and the ratio of modified to unmodified fluorescence lifetime.

an unmodified fluorescence region. It can be clearly seen that the lifetime in the presence of the nanoparticles is modified from the case where there is no nanoparticle, to varying degrees. The zoomed in section of figure 6.1b) shows this most clearly, since the modification of the lifetime in the region of the nanoparticle typically takes the form of a short lifetime, and so the modification is most obvious in the first few nanoseconds of the decay. It is thought that the varying lifetime modification depending on different nanoparticles is due to the extent of the overlap between the fluorescence emission spectrum of the dye and the LSPR of the nanoparticle, and it is this assertion that this chapter aims to investigate.

Another observation worth thinking about is the relatively large width of the LSPR peak. Initially this was a cause of some concern, but bulk spectroscopic measurements from the gold colloid supplier BBInternational suggested that the bulk LSPR peak would be around 570nm for 100nm gold nanoparticles, and that the FWHM of the bulk LSPR peak would be

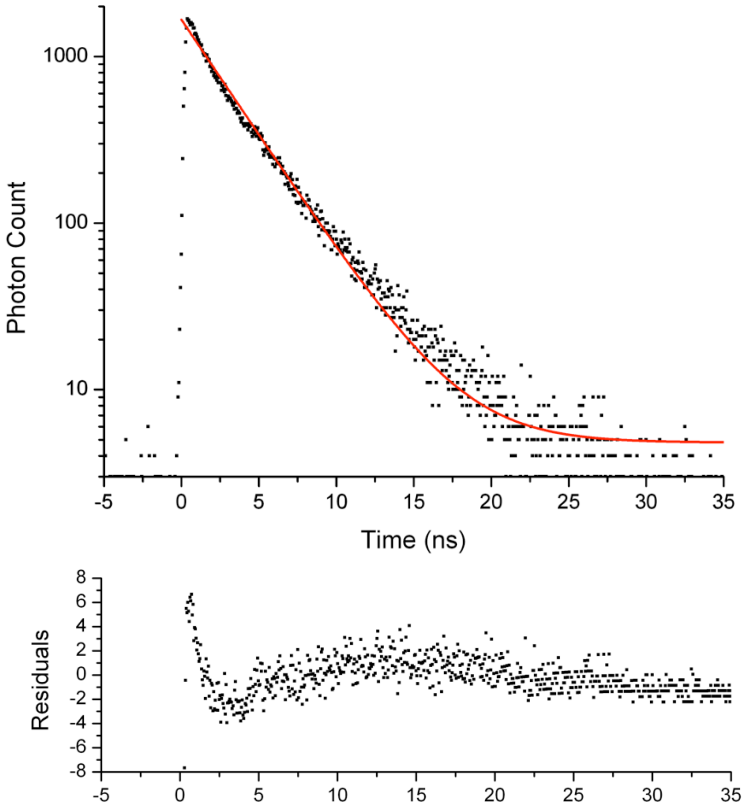

Figure 6.3: The unmodified fluorescence decay data from a Nile Red sample, with a mono-exponential decay fitted. The χ^2 value here is 2.48 and no fit parameters were dictated. Underneath the difference between the data and the fit is plotted in the form of residuals (weighted by 1/sqrt(fit)). This data conforms poorly to a mono-exponential fit.

expected to be in excess of 100nm. As such the large width of the individual LSPR peaks is consistent with these observations.

Initial measurements were taken using PMMA embedded with Nile Red, and 100nm diameter gold nanoparticles. Measurements of the fluorescence lifetime were analysed using the method outlined in section 4.5, the same analysis methods as was used for the interrogation of the spacer samples. As mentioned in section 3.5, all dark field spectra are taken using an Avantes Spectrometer, which collects light scattered by the nanoparticles from a structured laser source. The data is then fitted to a Gaussian curve using OriginLab software, and the location of the peak of the Gaussian is noted. It is this LSPR value that is then compared to the ratio of modified to unmodified fluorescence lifetime (τ_m / τ_0).

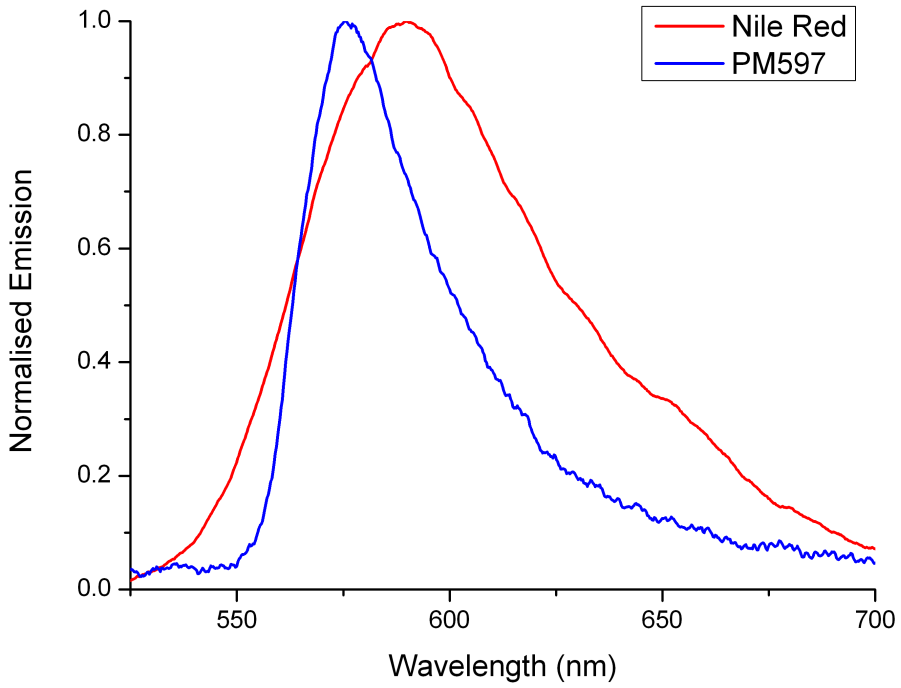

Figure 6.4: A comparison between the emission spectra of the two dyes used in this chapter, Nile Red and PM597.

The initial data collected can be seen in figure 6.2. This graph shows the distribution of τ_m/τ_0 with LSPR peak wavelength, and how they vary depending on their location relative to the fluorescence emission peak. This data clearly shows no trend, and a relatively small variation in τ_m/τ_0 for the different values of LSPR. However, with careful consideration of the data a number of reasons why Nile Red was not a suitable candidate for these measurements were uncovered, and these are outlined below.

Firstly and most importantly, Nile Red, as mentioned in section 4.3.2, has an environment dependent fluorescence response. While initial measurements had suggested that this response conformed to a mono-exponential decay, further measurements taken showed that even when the dye was not in the region of a nanoparticle it conformed to a bi-exponential fit rather than a mono-exponential fit. This can be seen in figure 6.3, especially in the residuals that show the difference between the data and the fit. Additionally this deviation from the mono-exponential fit is clearly seen in the upper part of the decay. This is a problem because the fitting used makes the assumption that the unmodified fluorescence lifetime takes the form of a mono-exponential. If this is not the case, then it

cannot be assumed that the component of the decay that makes it bi-exponential is due to the presence of the nanoparticle. Additionally, the bi-exponential component from the unmodified lifetime and the bi-exponential component from the presence of the nanoparticle occur in the same area of the decay, and as such it's impossible to instigate some workaround, as the two are indiscernible.

The second issue is the comparative width of the Nile Red fluorescence emission spectrum. As can be seen in figure 6.1, the LSPR spectra are broad, and in the case where the emission spectrum of the dye is also broad, small differences in the LSPR spectra measured will not cause significant differences in the extent of the overlap with the emission spectrum of the dye.

As such, a new dye is required in order to retake these measurements. Figure 6.4 shows the contrast between the fluorescence emission spectrum of Nile Red and that of PM597, the dye of choice for the majority of the spacer sample measurements, as well as for the remainder of the measurements considering the effects of LSPR on τ_m/τ_0. PM597 has a much narrower emission spectrum than Nile Red, which makes it easier to vary the extent of the overlap between the LSPR and the dye emission.

Additionally, PM597 shows a mono-exponential fluorescence lifetime decay, as seen in figure 6.5. These features make it a much more appropriate candidate for further measurements of this system.

6.2 Phase 2 Measurements – A New Dye and Nanoparticle Size

For reasons detailed in the previous chapter, the second phase of measurements used PM597 instead of Nile Red as the fluorescent dye. In addition to swapping the dye, a further nanoparticle size, diameter 60nm, was also used to allow interrogation of a different part of the LSPR spectrum. The results of this phase are shown in figure 6.6. Here a change in τ_m/τ_0 is observed over a range of LSPR values. There also seems to be – although it is not very clear – a minimum in τ_m/τ_0 coinciding with the leading edge of the PM597 emission spectrum. However, care must be taken when drawing any firm conclusions as to the nature of this minimum here, as it occurs between the 60 and 100nm particles, with the exception of one blue-shifted 100nm diameter nanoparticle.

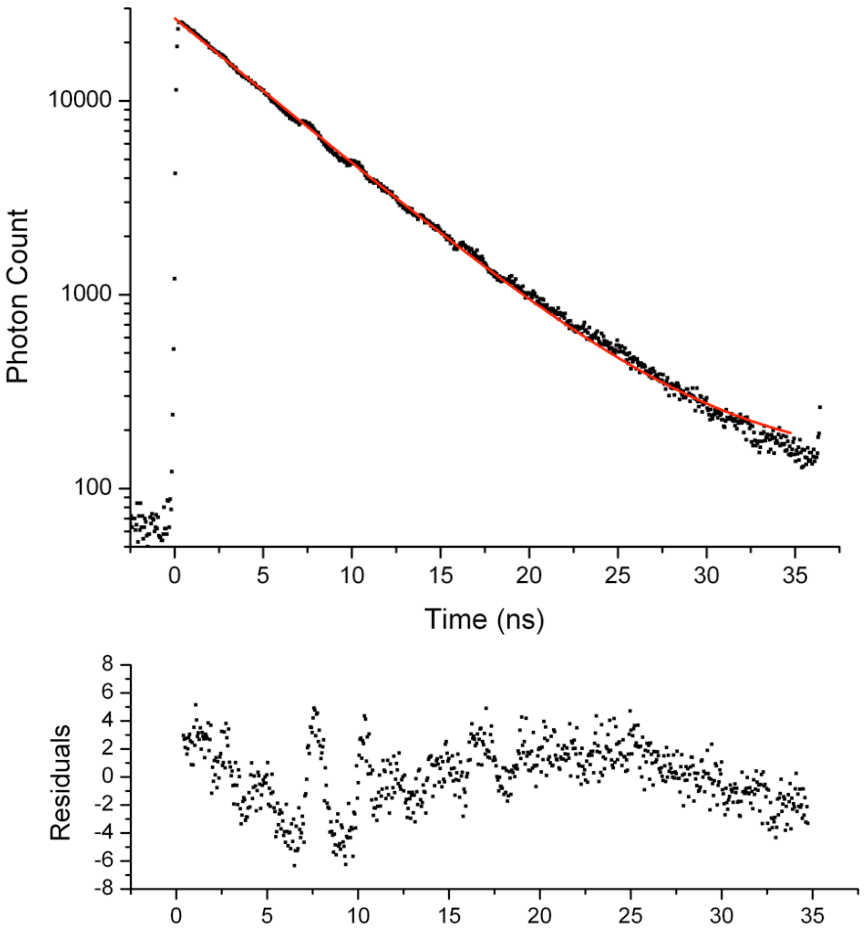

Figure 6.5: An unmodified fluorescence decay data from a PM597 sample, conforms well to a fitted monoexponential decay. The χ^2 value is 4.82 with no fit parameters dictated. Underneath the difference between the data and the fit is plotted in the form of residuals (weighted by 1/sqrt(fit)). The slight oscillation observed in the residuals comes from unavoidable electrical interference, rather than being an artifact of a poor fit. Additionally the residual size is at least two orders smaller than the magnitude of the maximum decay photon count, giving further confidence that this is a very good fit.

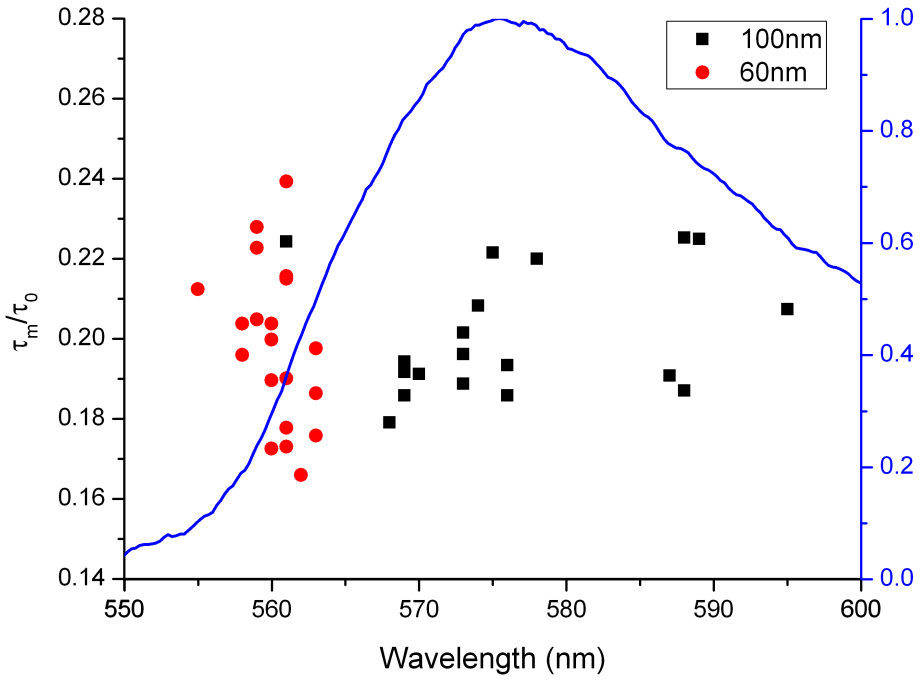

Figure 6.6: The ratio of modified to unmodified fluorescence for the fluorescence from PM597 in the vicinity of two populations of nanoparticles, one 60nm in diameter and one 100nm in diameter, plotted against the peak LSPR wavelength. The emission spectrum for PM597 is included to allow the comparison of features of the spectrum with features of the distribution.

With a lack of a conclusive trend observed here, it was decided to do some further analysis on the data to make sure that the LSPR value was as robust as possible. There are a number of potential problems with the method used initially where the data is simply fitted with a Gaussian and the peak value fitted.

Firstly, the laser, as mentioned in previously, is a structured source. In the laser stability graph shown in figure 3.10 a strong variation in intensity can be seen across the spectrum. This will undoubtedly affect the shape of the LSPR spectrum, potentially skewing the results of the Gaussian fit and therefore the peak LSPR value.

Secondly, and more importantly, the widths and heights of the LSPR spectra are not consistent from nanoparticle to nanoparticle. Some nanoparticles exhibit a much broader scattering spectrum than others, and the extent to which the nanoparticle scatters can vary,

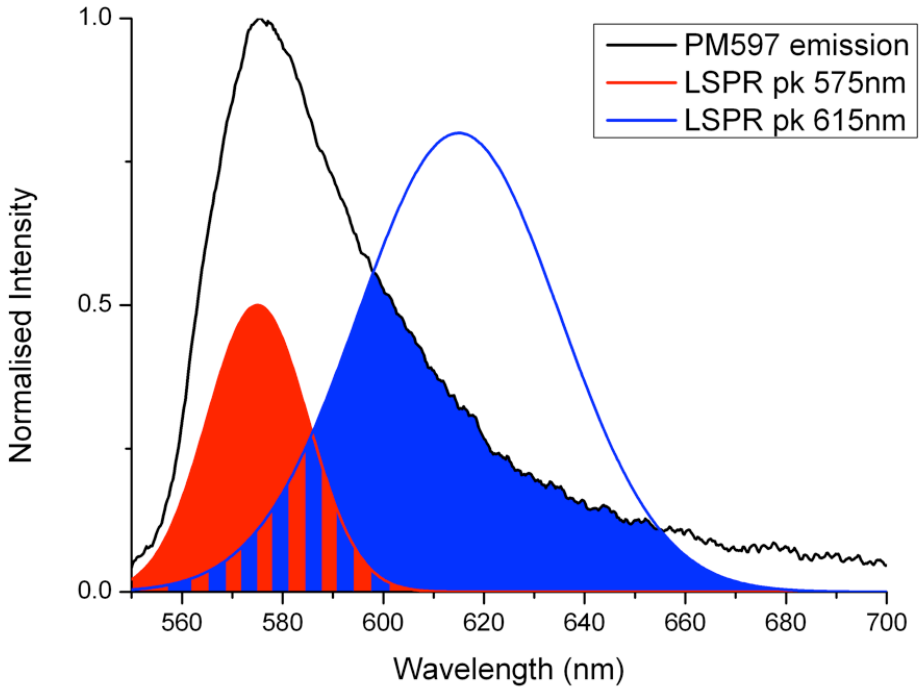

Figure 6.7: A figure showing the difficulties of LSPR peak as a measurement of the extent of the overlap between the LSPR spectrum and the fluorescence emission spectrum. Two theoretical nanoparticle LSPR spectra are shown and the extent to which these different spectra overlap with the emission dye is shown. It is clear that due to varying LSPR peak heights, the spectra where the LSPR is closest to the dye emission peak are not necessarily the spectra that will show the greatest overlap.

leading to different scattering intensity values. The result of these differing shapes is that simply taking the location of the LSPR peak wavelength may be misleading, since the actual parameter that is intended for comparison is the extent of the overlap between the LSPR spectrum and the fluorescence emission spectrum. Figure 6.7 depicts this problem graphically using theoretical nanoparticle LSPR spectra, and shows that it is possible to have a poor alignment of the LSPR with the peak of the scattering spectra but still have a comparatively large overlap between the LSPR spectrum and the fluorophore emission.

Thus, rather than plotting the peak LSPR wavelength against τ_m/τ_0, an overlap integral is calculated between the LSPR spectrum and the fluorescence emission spectrum using the following process. Initially, the LSPR spectrum is normalised with respect to the laser

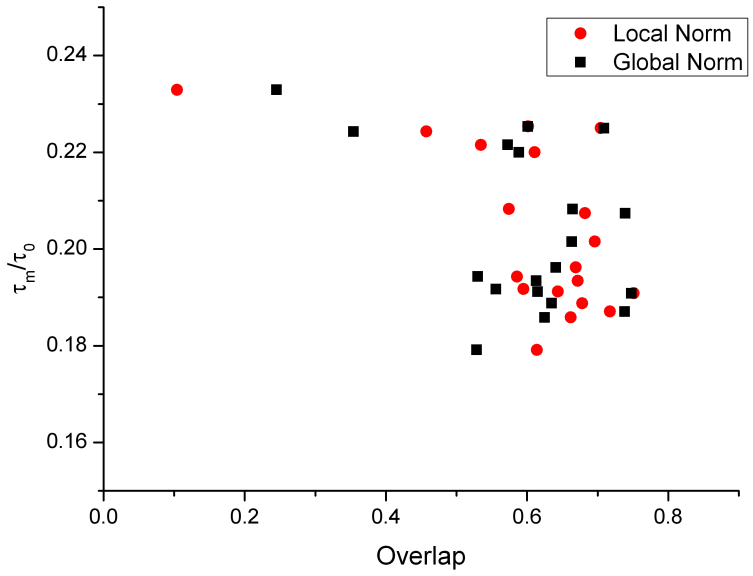

Figure 6.8: A graph depicting the ratio of modified lifetime to unmodified lifetime against the 100nm LSPR scattering spectrum/fluorescence emission spectrum overlap. The data is analysed in two different ways, global normalisation and local normalisation, and the results of both analyses are now plotted to demonstrate the similarity of the results derived from both methods.

emission to remove any structuring in the LSPR. There are then two options for data analysis. Either all the spectra can be normalised with respect to the spectrum that is greatest in intensity (this will be referred to as global normalisation), or each spectrum can be normalised to itself (this will be referred to as local normalisation). The ideal case is the global normalisation, as this allows for any variation in the peak height occurring from different relative scattering strengths to be taken into consideration. However, this assumes that all nanoparticle scattering measurements were taken at the point where they were optimally aligned with the optical fibre, and as such at the maximum value possible for that nanoparticle. If this is not the case, then globally normalizing is an error. However, if this holds true – and the expectation is that if it does hold true – then there should be little variation between the distribution seen for a globally normalised or a locally normalised LSPR spectra. Once the normalisation method had been selected, the overlap between the two spectra was then calculated using a normalised cross correlation function algorithm of the form

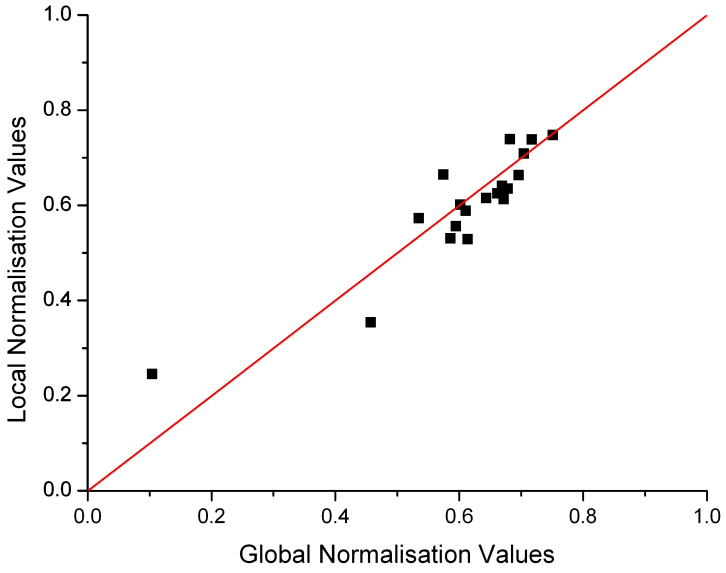

Figure 6.9: A graph depicting the correlation between the global and local normalisation values. A line of gradient 1 is included to demonstrate a clear linear correlation between the two sets of data.

$$x_{overlap} = \frac{1}{n}\sum_{n}\frac{\left(f_s(n)-\bar{f}_s\right)\left(f_{em}(n)-\bar{f}_{em}\right)}{\sigma_s\sigma_{em}} \tag{6.1}$$

where n is the number of points in the spectrum, $f_s(n)$ and $f_{em}(n)$ are the emission and scattering spectra respectively, $\bar{f}_s$ and $\bar{f}_{em}$ are the average values of the spectra, and σ_s and σ_{em} are the standard deviation of the scattering and emission spectra. For a sample with complete spectra overlap, this value will be 1, and for a sample with no spectral overlap at all, the value will be 0.

Figure 6.8 shows the same set of 100nm particle data from figure 6.6 analysed in two different ways on the same plot, one set using a global normalisation, and the other using a local normalisation. Reassuringly, there is good correlation shown between the two data sets, suggesting that there is not a huge discrepancy in the peak intensity values. This result would be expected given that all scattering spectra were taken from 100nm particles, and so unless there was huge and unexpected variation in shape it would make sense that the peak heights would be relatively similar; the signal/noise ratio for the LSPR scattering spectra for the 60 nm nanoparticles is too great for a meaningful determination of the overlap integral.

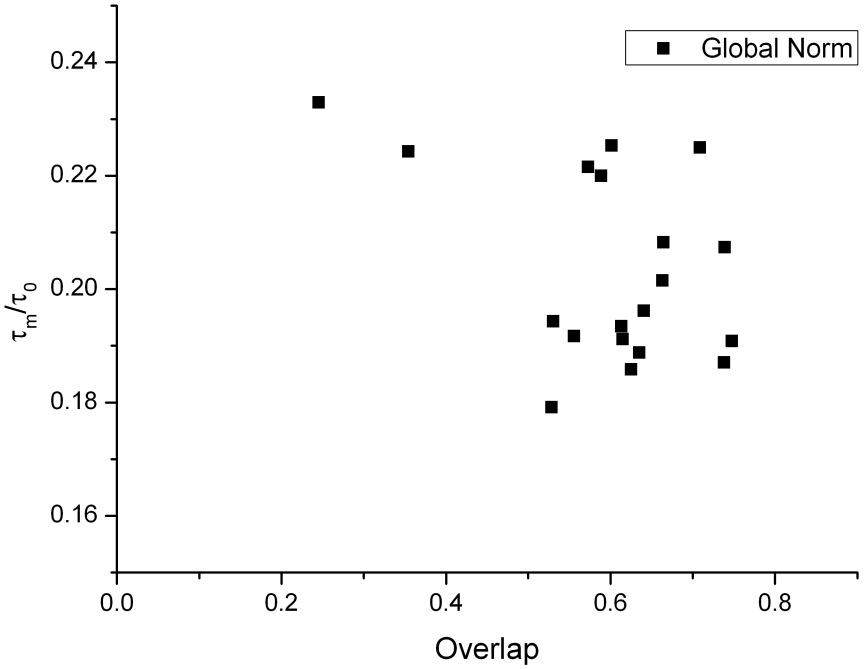

Figure 6.10: The ratio of modified lifetime to unmodified lifetime against the globally normalised LSPR scattering spectrum/fluorescence emission spectrum overlap.

Similarly, a good one-to-one correlation between the locally normalised and the globally normalised data as demonstrated in figure 6.9. As such, the globally normalised data is preferable, as it will take into account small variations in peak height.

This data has now been analysed in a robust and thorough manner, which in turn throws up a number of issues and questions. It seems to be that a decrease in the extent of the overlap leads to an increase in τ_m/τ_0, which is to be expected. But if this is the case, why then is a change in τ_m/τ_0 observed, albeit a small one, with seemingly no change in the spectral overlap value? It is possible that here our approach is insufficiently sensitive to shorter lifetimes, and the long unmodified lifetime component is dominating the analysis. As τ_m/τ_0 increases there does seem to be a sudden change in the extent of the spectral overlap, but in order to understand this observation better more data a greater range of overlap values, small overlap especially, would need to be measured, as this data set is clearly deficient at lower spectral overlap values. A full understanding of this behaviour would require a detailed theoretical investigation and computational modeling, which is beyond the scope of this project.

6.3 Summary

This chapter examined the relationship between LSPR and the ratio of modified to unmodified fluorescence lifetime. A large population of single nanoparticles were imaged, both using FLIM and dark-field. Initially two different fluorescence dyes were investigated, Nile Red and PM597, but it was decided to use PM597 for final measurements due to Nile Red's comparatively complicated photophysical properties. The data was analysed in two different ways, firstly by simply plotting the LSPR peak against τ_m/τ_0. The data seemed to show a trend where a local minimum in τ_m/τ_0 was observed coinciding with the leading edge of the fluorescence emission spectrum. However, plotting LSPR peak was considered to be an less than robust approach due to height variation within the LSPR spectra, meaning that the degree to which the LSPR peak matched the emission maximum from the dye did not necessarily correlate to the size of the overlap between the emission spectrum and the LSPR spectrum. Instead using a cross-correlation function algorithm, this overlap value calculated and was then plotted against τ_m/τ_0. This data analysis tentatively showed that a smaller degree of overlap between the LSPR spectra and the dye emission spectra seemed to cause an increase in the value of τ_m/τ_0, but in order to be sure of this trend more data would need to be collected, particularly in regions where the overlap between the LSPR and the dye emission spectrum is considerably less.

Chapter 7 – Conclusions

The goal of this thesis was to improve understanding of single nanoparticle modified fluorescence. This project was undertaken with a view to helping to contribute to the formation of a complete understanding of the role that spectral overlap between fluorescence excitation, LSPR and fluorescence emission plays in fluorescence enhancement, as well as better understanding the influence that fluorophore and nanoparticle separation has on the modification of fluorescence lifetime and intensity, particularly in sub-resolution samples. The pursuit of these two goals, that is the investigation of the relationship between LSPR and enhancement and the investigation of the relationship between nanoparticle/dye separation distance and enhancement, comprised the bulk of the results in this thesis.

The presence of some gold nanoparticle in close proximity to some fluorescent dye-embedded polymer was shown to produce a large intensity enhancement in the local fluorophores, as well as a corresponding decrease in fluorescence lifetime. The presence of the nanoparticle altered the local density of states and as such changed the nature of the fluorescence decay from a simple monoexponential to a more complex exponential. This response was expected in accordance to the work of Sandoghdar and Novotny as outlined in section 1.3. However, given that much of their work concerned a single fluorescent molecule system and the system of interest here was a bulk fluorophore system a parameterisation of this reduction in lifetime was required, and so a bi-exponential function was fitted to the data. In this bi-exponential there would be a large unmodified fluorescence component, some modified component. This modified component resulted from the fact that, due to the small size of the nanoparticle in comparison to the diffraction limited spot, it was impossible to separate out individual modified fluorescence lifetimes and these would therefore be averaged to form the modified lifetime component. This method contrasts with the stretched exponential method conventionally adopted by groups like Ginger's to fit bulk fluorescence data (11). The lifetimes of these two components were then compared, and, while this parameterisation method required some care to ensure that it could be used to compare data from different samples, τ_m/τ_0 the was used for establishing trends within the

data initially. Having established what was considered to be an appropriate data fitting method, two principal relationships were examined.

Firstly, the relationship between fluorophore modification and nanoparticle/fluorophore separation was investigated. The interrogation of a large population of nanoparticles gave a statistical distribution of intensity enhancement and lifetime reduction, which was attributed to varying nanoparticle size and shape – a parameter known to cause variation in the LSPR and thus the LSPR/fluorescence excitation overlap. Analysis of the phase one data showed a variation in intensity enhancement and lifetime reduction as the spacer layer was changed, but due to uncertainties in the spacer thickness no more conclusive information about the trend could be given. However, τ_m/τ_0 was plotted against the intensity enhancement value, which showed a clear relationship between the two parameterisation values. When the value of τ_m/τ_0 was low a stronger intensity enhancement was observed, and similarly when less of a modification in lifetime occurred, the value of intensity enhancement was considerably lower. Phase two measurements considered a much larger nanoparticle sample set, and showed a variation in intensity enhancement that demonstrated good agreement with the theoretical data discussed in section 2.3.6, with fluorescence quenching observed when there was no spacer layer, then a peak enhancement at small separation, with the extent of the fluorescence enhancement decreasing as the distance between the nanoparticles and the fluorophores increased. However the lifetime modification data did not agree with the theoretical expectations at all, and instead of τ_m/τ_0 increasing with distance, as the fluorescence lifetime tended to the unmodified value, instead τ_m/τ_0 showed a decrease with increasing distance. It is possible that this anomalous behaviour results from an inadequacy in the fitting method – if the modified component of the bi-exponential is too small it might account for fluctuations in this value. In an attempt to address this, the data was analysed using a weighted lifetime modification radio of the form $A_m\tau_m/A_0\tau_0$. This resulted in a more physically sensible trend. However, in order to be sure it would be prudent to interrogate a broader range of spacer thickness samples to acquire more data points and see if this is a real trend or not – three data points is not ideal. It might also be worth revisiting the existing data with an alternative means of analysis to see whether similar trends are obtained.

In terms of the magnitude of the modification, the approximate calculation for the PM dye yielded a rough enhancement factor of around 6.4. This seems broadly in agreement with

theoretical predictions from Novotny's group (7) where it was suggested that at 650nm a gold nanoparticle could be expected to show an enhancement factor of around 6, although the differing optical constants of gold at these wavelengths make too direct a comparison unwise. They also observed that the optimum fluorescence enhancement was found when the excitation wavelength was red-shifted with respect to the LSPR of the nanoparticle – a regime with which this study did not concern itself. They also observed that in the case of a 80nm diameter nanoparticle in the region of a PMMA film embedded with Nile blue optimal enhancement is both predicted theoretically, and experimentally observed at a distance of around 5nm. While the variation in spacer thickness was not small enough to establish that this is also the case in this study, in figure 5.10 the histogram showing the trend in intensity enhancement with spacer thickness suggested that for the thicknesses interrogated in this study, a 10 nm spacer provided optimum enhancement, which again would seem be in good agreement with Novotny's results, particularly as with the 80nm diameter gold nanoparticle they used it would be expected that the reflection field would decay more quickly than in the case of a 100nm gold nanoparticle.

Secondly, the relationship between spectral overlap between fluorescence excitation, LSPR and fluorescence emission and its role in fluorescence enhancement was considered. Again, large populations of nanoparticles were interrogated, but this time, in addition to fluorescence intensity and lifetime information, dark-field information was also acquired for individual nanoparticles. The modified to unmodified fluorescence lifetime values were then plotted against LSPR peak values in order to determine the extent to which the alignment of the LSPR peak with the fluorescence emission peak affected τ_m/τ_0 values. A trend seemed to be observed, showing a small minimum in τ_m/τ_0 at the leading edge of the PM597 emission spectrum. However, given that the nanoparticles did not all scatter light to exactly the same extent, it was decided instead to calculate the spectral overlap by cross-correlating the data, and thus plot that against τ_m/τ_0 instead. One of the principle limitations with the data here is simply that there is not enough of it, and it doesn't cover enough of the spectrum. In order to draw any firm conclusions, more points where spectral overlap is very poor would be ideal. However, even in the absence of this extra data, it is possible to tentatively conclude from existing data that a large degree of overlap between the LSPR spectra and the dye emission spectra seemed to cause a decrease in the value of τ_m/τ_0. This would seem to be consistent with work done by Ginger's group (10,11) and De

Costa's group (27), although the inconclusive nature of the results in this study would make further comment presumptuous at this stage.

This project leaves much scope for further work. Given the seemingly counter-intuitive nature of some of the results found here, in addition to the potential for more data collection, a comprehensive theoretical investigation would seem appropriate. The simple and well-defined nature of the systems that were investigated should make computationally modeling the system in order to understand behaviour, not trivial, but at least readily achievable.

It is hoped that in investigating the effects that the fluorophore/nanoparticle separation has on the modification of fluorescence lifetime and intensity, as well as considering carefully the role that spectral overlap between fluorescence excitation, LSPR and fluorescence emission plays in fluorescence enhancement this project has made some contribution to the understanding of single nanoparticle enhanced fluorescence.

References

(1) Herman B, Frohlich VE, Lakowicz JR, Murphy DB, Spring KR, Davidson MW. Basic Concepts in Fluorescence. 2012; Available at: http://www.olympusmicro.com/primer/techniques/fluorescence/fluorescenceintro.html. Accessed 4th August, 2013.

(2) Huang F, King's College, London. Department of Physics. Tip-enhanced optical spectroscopy and microscopy. ; 2005.

(3) Purcell EM, Torrey HC, Pound RV. Resonance Absorption by Nuclear Magnetic Moments in a Solid. Phys Rev 1946;69:37-38.

(4) Kühn S, Håkanson U, Rogobete L, Sandoghdar V. Enhancement of Single-Molecule Fluorescence Using a Gold Nanoparticle as an Optical Antenna. Phys Rev Lett 2006;97:017402.

(5) Cade NI, Culfaz F, Eligal L, Ritman-Meer T, Huang F, Festy F, et al. Plasmonic Enhancement of Fluorescence and Raman Scattering by Metal Nanotips. Nanobiotech 2007;3:203-211.

(6) Kümmerlen J, Leitner A, Brunner H, Aussenegg F, Wokaun A. Enhanced dye fluorescence over silver island films: analysis of the distance dependence. Mol Phys 1993;80:1031-1046.

(7) Anger P, Bharadwaj P, Novotny L. Enhancement and Quenching of Single Molecule Fluorescence. Phys Rev Lett 2006;96(11):113002-113006.

(8) Bharadwaj P, Anger P, Novotny L. Nanoplasmonic enhancement of single-molecule fluorescence. Nanotech 2007;18:044017.

(9) Ming T, Zhao L, Yang Z, Chen H, Sun L, Wang J, et al. Strong Polarization Dependence of Plasmon-Enhanced Fluorescence on Single Gold Nanorods. Nano Lett 2009 11/11; 2013/10;9(11):3896-3903.

(10) Chen Y, Munechika K, Ginger DS. Dependence of Fluorescence Intensity of the Spectral Overlap between Fluorophores and Plasmon Resonant Single Silver Nanoparticles. Nano Lett 2007;7:690-696.

(11) Munechika K, Chen Y, Tillack A, Kulkarni A, Plante I, Munro A, et al. Spectral Control of Plasmonic Emission Enhancement from Quantum Dots near Single Silver Nanoprisms. Nano Lett 2010;10:2598-2603.

(12) Cade NI, Fruhwirth GO, Ng T, Richards D. Plasmon-Assisted Super-Resolution Axial Distance Sensitivity in Fluorescence Cell Imaging. J Phys Chem Lett 2013 09/26; 2013/10:3402-3406.

(13) Ray K, Badugu R, Lakowicz JR. Sulforhodamine Adsorbed Layers on Silver Island Films: Effect of Probe Distance on the Metal-Enhanced Fluorescence. J Phys Chem C 2007 05/01; 2013/10;111(19):7091-7097.

(14) Cade NI, Fruhwirth G, Archibald SJ, Ng T, Richards D. A cellular screening assay using analysis of metal-modified fluorescence lifetime. Biophys J 2010 Jun 2;98(11):2752-2757.

(15) Hobson PA, Wedge S, Wasey JAE, Sage I, Barnes WL. Surface Plasmon Mediated Emission from Organic Light-Emitting Diodes. Adv Mater 2002;14(19):1393-1396.

(16) Lakowicz JR. Introduction to Fluorescence. Principles of Fluorescence Spectroscopy. 3rd ed. New York: Springer; 2006. p. 1-26.

(17) Herschel, Sir J. F. W. On a case of Superficial Colour Presented by a Homogenous Liquid Internally Colourless. Phil Trans Roy Soc 1845;135:143-145.

(18) Stokes GG. On the Change of Refrangibility of Light. Phil Trans Roy Soc 1852;142:463-562.

(19) Jablonski A. Efficiency of Anti-Stokes Fluorescence in Dyes. Nature 1933;131:839-840.

(20) Song L, Hennink EJ, Young IT, Tanke HJ. Photobleaching kinetics of fluorescein in quantitative fluorescence microscopy. Biophys J 1995 Jun;68(6):2588-2600.

(21) Axelrod D, Koppel DE, Schlessinger J, Elson E, Webb WW. Mobility measurement by analysis of fluorescence photobleaching recovery kinetics. Biophys J 1976 9;16(9):1055-1069.

(22) Clegg RM. Fluorescence resonance energy transfer. Curr Opin Biotechnol 1995;6(1):103-110.

(23) Selvin PR. Fluorescence resonance energy transfer. Methods in Enzymology: Academic Press; 1995. p. 300-334.

(24) Jares-Erijman EA, Jovin TM. FRET Imaging. Nat Biotech 2003;21(11):1387-1395.

(25) Palumbo G, Pratesi R, Royal Society of Chemistry. Lasers and current optical techniques in biology. 2004;4:658.

(26) Seelig J, Leslie K, Renn A, Kühn S, Jacobsen V, van de Corput M, et al. Nanoparticle-Induced Fluorescence Lifetime Modification as Nanoscopic Ruler: Demonstration at the Single Molecule Level. Nano Lett 2007(3):685.

(27) Teixeira R, Paulo PMR, Viana AS, Costa S. Plasmon-Enhanced Emission of a Phthalocyanine in Polyelectrolyte Films Induced by Gold Nanoparticles. J Phys Chem C 2011 12/22; 2013/09;115(50):24674-24680.

(28) Maier SA. Plasmonics: fundamentals and applications. 1st ed. New York: Springer, /; 2007.

(29) Barnes WL, Dereux A, Ebbesen TW. Surface plasmon subwavelength optics. Nature 2003 Aug 14;424(6950):824-830.

(30) Kelf TA, Sugawara Y, Cole RM, Baumberg JJ. Localized and delocalized plasmons in metallic nanovoids. Phys Rev B 2006;74(24):245415.

(31) Ghaemi HF, Thio T, Grupp DE, Ebbesen TW, Lezec HJ. Surface plasmons enhance optical transmission through subwavelength holes. Phys Rev B 1998;58(11):6779-6782.

(32) Cade NI, Ritman-Meer T, Richards D. Strong coupling of localized plasmons and molecular excitons in nanostructured silver flims. Phys Rev B 2009;79:241404.

(33) Atwater H. The Promise of Plasmonics. Scientific American 2007;296:56-62.

(34) Bohren CF, Huffman DR. Absorption and scattering of light by small particles. Wiley Professional Paperback ed. New York: Wiley; 1998.

(35) Kelly KL, Coronado E, Zhao LL, Schatz GC. The Optical Properties of Metal Nanoparticles: The Influence of Size, Shape, and Dielectric Environment. J Phys Chem B 2003 01/01; 2013/08;107(3):668-677.

(36) Böttcher CJF, van Belle OC, Bordewijk P, Rip A. Theory of Electric Polarization. 2nd Edition ed. Amsterdam, New York: Elsevier Scientific Pub. Co.; 1973.

(37) Fort E, Grésillon S. Surface enhanced fluorescence. J Phys D 2008;41(1):013001.

(38) Metiu H. Surface enhanced spectroscopy. Prog Surf Sci 1984;17(3–4):153-320.

(39) Thomas M, Greffet J-, Carminati R, Arias-Gonzalez JR. Single-molecule spontaneous emission close to absorbing nanostructures. Appl Phys Lett 2004 October 25, 2004;85(17):3863-3865.

(40) Ritman-Meer T, King's College, London. Department of Physics. Surface enhanced fluorescence and Raman spectroscopy using noble metal nanostructures. London: University of London; 2009.

(41) Chance RR, Prock A, Silbey R. Lifetime of an emitting molecule near a partially reflecting surface. J Chem Phys 1974;60(7):2744.

(42) Chance RR, Prock A, Silbey R. Comments on the classical theory of energy transfer. J Chem Phys 1975 March 15, 1975;62(6):2245-2253.

(43) Gersten J, Nitzan A. Spectroscopic properties of molecules interacting with small dielectric particles. J Chem Phys 1981 August 1, 1981;75(3):1139-1152.

(44) Drexhage KH, Kuhn H, Schäfer FP. Variation of the Fluorescence Decay Time of a Molecule in Front of a Mirror. Berichte der Bunsengesellschaft für physikalische Chemie 1968;72(2):329-329.

(45) Barnes WL. Fluorescence near interfaces: The role of photonic mode density. Journal of Modern Optics 1998 04/01; 2013/08;45(4):661-699.

(46) Sullivan KG, Hall DG. Enhancement and inhibition of electromagnetic radiation in plane-layered media. 1. Plane-wave spectrum approach to modeling classical effects. J Opt Soc Am B 1997;14(5):1149.

(47) Lakowicz,J.R., Malicka,J., Gryczynski I, Gryczynski Z, Geddes CD. Radiative decay engineering: the role of photonic mode density in biotechnology. J Phys D App Phys 2003;36:240-249.

(48) Emmanuel Fort and SG. Surface enhanced fluorescence. J Phys D 2008;41(1):013001.

(49) Huang F, Richards D. Fluorescence Enhancement and Energy Transfer in Apertureless Scanning Near-Field Optical Microscopy. J Opt A: Pure Appl Opt 2006;8:S234-S238.

(50) Becker W. Classic Time-Correlated Single Photon Counting. The bh TCSPC Handbook. 5th Edition ed.: Becker & Hickl GmbH; 2012. p. 51-58.

(51) Becker W. Advanced Time-Correlated Single Photon Counting Techniques. Berlin: Springer; 2005.

(52) Chung P, King's College, London. Department of Physics. Advanced fluorescence lifetime imaging and spectroscopy techniques for biological samples. ; 2012.

(53) Lakowicz JR. Instrumentation for Fluorescence Spectroscopy. Principles of Fluorescence Spectroscopy. 3rd ed.: Springer; 2006. p. 27-61.

(54) Becker W. Multi-Dimensional TCSPC. The bh TCSPC Handbook. 5th Edition ed.: Becker & Hickl GmbH; 2012. p. 59-64.

(55) Murphy DB, Davidson MW. Darkfield Microscopy. Fundamentals of Light Microscopy and Electronic Imaging. 2nd ed.: John Wiley & Sons; 2012. p. 129-133.

(56) Binnig G, Quate CF, Gerber C. Atomic Force Microscope. Phys Rev Lett 1986;56:930-934.

(57) Binnig G, Rohrer H. Scanning tunneling microscopy. Surf Sci 1983 3/2;126(1–3):236-244.

(58) Hall DB, Underhill P, Torkelson JM. Spin coating of thin and ultrathin polymer films. Polymer Engineering & Science 1998;38(12):2039-2045.

(59) Bek A, Jansen R, Ringler M, Mayilo S, Klar TA, Feldmann J. Fluorescence Enhancement in Hot Spots of AFM-Designed Gold Nanoparticle Sandwiches. Nano Lett 2008 02/01; 2013/10;8(2):485-490.

(60) Nuffield-Chelsea Curriculum Trust. Nuffield Advanced Science: Book of Data. Essex: Pearson Education Ltd.; 1972.

(61) Polyanskiy M. Refractive Index Database. Available at: http://refractiveindex.info. Accessed Sept. 11, 2013.

(62) Kubin R, Fletcher A. Fluorescence quantum yields of some rhodamine dyes. J Luminescence 1982;27:455.

(63) Greenspan P, Mayer EP, Fowler SD. Nile Red: A Selective Fluorescent Stain for Intracellular Lipid Droplets. J Cell Biol 1985;100:965-973.

(64) Cser A, Nagy K, Biczók L. Fluorescence lifetime of Nile Red as a probe for the hydrogen bonding strength with its microenvironment. Chemical Physics Letters 2002 7/17;360(5–6):473-478.

(65) Bañuelos Prieto J, López Arbeloa F, Martínez Martínez V, Arbeloa López T, López Arbeloa I. Photophysical Properties of the Pyrromethene 597 Dye: Solvent Effect. J Phys Chem A 2004;108:5503-5508.

(66) Barber PR, Ameer-Beg SM, Gilbey J, Carlin LM, Keppler M, Ng T, et al. Multiphoton time-domain fluorescence lifetime imaging microscopy: practical application to protein-protein interactions using global analysis. J R Soc Interface 2009;6:S93-S105.

(67) Christy RW, Johnson PB. Optical Constants of the Noble Metals. Phys Rev B 1972;6:4370.